universität wien

DISSERTATION / DOCTORAL THESIS

Titel der Dissertation /Title of the Doctoral Thesis

Innovative tools for preclinical studies on anticancer drugs with metabolomics approaches

verfasst von / submitted by

Mate Rusz MSc

angestrebter akademischer Grad / in partial fulfilment of the requirements for the degree of

Doktor der Naturwissenschaften (Dr.rer.nat.)

Wien, 2022 / Vienna 2022

Studienkennzahl lt. Studienblatt / degree programme code as it appears on the student record sheet:	A 796 605 419
Dissertationsgebiet lt. Studienblatt / field of study as it appears on the student record sheet:	Chemie
Betreut von / Supervisor:	o. Univ.-Prof. Dr. Dr. Bernhard Keppler
Betreut von / Supervisor:	Univ.-Prof. Dr. Gunda Köllensperger

Acknowledgment

It has been my dream and aspiration to become a researcher for a long time. I am very grateful for the fact, that I could live this dream. In the following, I try to briefly mention who I need to thank for this…

I would like to thank **Prof. Bernhard Keppler** for giving me the opportunity to work on this project and proving a solid financial background for all the scientific work.

Above all, I am deeply grateful to my supervisor **Gunda Köllensperger**, for her constant support and fighting along my side during all these years.

I thank **Jürgen Zanghellini** and **Helena Herrmann** for their modeling efforts and for introducing network science and computational biology on a professional level to us.

Additionally, I would like to express my sincere gratitude to **Walter Berger** and **Dina Baier** for their support and many interesting discussions and fruitful cooperation on the field of cancer drug resistance.

My gratitude extends to **Giorgia Del Favero** for her contribution to live cell imaging microscopy experiments and morphological studies.

For their insightful comments and suggestions during the planning of the experiments and the preparation of the manuscripts, I thank **Michael Jakupec** and **Christopher Gerner**.

I would like to offer my special thanks to **Michaela Schwaiger**, **Yasin El Abiead**, **Harald Schöny**, **Veronika Fitz**, **Gerrit Hermann**, **Evelyn Rampler** and other members of the Köllensperger Lab. It has been a pleasure to be in the company of such progressive and nice colleagues for years!

I acknowledge various persons, whose work enabled a high level of organization in the laboratories and thus conduction of efficient experiments, **Klaudia Cseh**, **Michaela Hejl**, **Petra Volejnik**, **Christoph Baumgartinger**, as well as members of the Mass Spectrometry Centre of the University of Vienna.

Furthermore, I would like to thank **Susanne Stockburger** and **Benita Eberhardt-Lange** to kindle my interest in biology and chemistry, and **Éva Frank** who taught me to appreciate a carefully crafted text and great writing.

Last but not least, I want to thank my whole family and friends, especially my parents for always supporting my pursuit of science.

Abstract

In this Ph.D. thesis, bioanalytical approaches and innovative tools with liquid chromatography-mass spectrometry-based metabolomics were developed and applied in preclinical studies on anticancer drugs.

Within the first publication, the optimization of sample preparation for three-dimensional multicellular tumor spheroid (3D MTS) cancer models is presented. The aim was to develop a suitable sample preparation method for spheroid cell culture models which is compatible with LC-MS-based metabolomics. As a particular challenge, spheroids are small, grow up to one mm in diameter in a non-scaffold, suspension-based setting, thus they are not only barely visible to the naked eye but also contain substantially less biomaterial (only a few 10.000s of cells), than conventionally used 2D monolayer cell cultures. The workflow has been optimized in terms of the extraction protocol, speed, washing steps, and a minimum number of spheroids required. The final protocol enables considerable throughput and repeatability (reproducibility), it requires only a single sub-mm spheroid and can be easily extended to any cell line which is inclined to form spheroids. Finally, the capability of the workflow has been demonstrated in a proof-of-principle experiment by response-profiling of spheroids exposed to two different anticancer metal complexes, oxaliplatin and BOLD-100/KP1339.

Next, a combined, fully parallelized metabolomics and live cell imaging **methodology** was developed to show the benefits of applying imaging technologies like live cell imaging to supplement metabolomics and illustrate that such an application is feasible. Furthermore, in a proof-of-concept experiment, we applied it to profile the early oxidative stress response upon a short (2 h) exposure to hydrogen peroxide and show how the imaging and omics methodology mutually compensate shortcomings and blind spots. We demonstrated the strength of the workflow by studying multifaceted and dynamic biological processes such as the fragmentation of the mitochondrial network in response to increasing external hydrogen peroxide influx. As a particular feature, it is able to recapitulate countless effects related to early phase oxidative stress response simultaneously in a single experiment.

In the third publication we investigated the metabolic basis of acquired resistance in the HCT116 cell line, as acquired resistance towards the established metallodrug oxaliplatin and clinically investigated BOLD-100/KP1339 were examined.

We used experimentally quantified absolute metabolite concentrations (normalized to total protein content) to determine metabolic fluxes with genome-scale metabolic modeling and flux-balance analysis computationally. For the complete modeling endeavor, the intracellular metabolite amounts

were complemented with the change of extracellular metabolite levels during a time-course experiment and the growth rate had been obtained for all models.

Regarding the difference between the two resistance models, most of the differences in metabolic fluxes were found in the fatty acid, amino acid and nucleotide metabolism. While most of these pathways are more active in the Ru-based resistance, indicating that this cell line is metabolically more active, pathways such as glycolysis and pentose phosphate pathway have higher fluxes in the Pt-based resistance model.

We applied genome-scale metabolic modeling and flux-balance analysis for the first time to investigate acquired metallodrug resistance for two cellular models and identified multiple metabolic effects common in metallodrug resistance, as well as other ones specific to the type of drug.

Zusammenfassung (German abstract)

In dieser Dissertation wurden bioanalytische Ansätze und innovative Werkzeuge mit Flüssigchromatographie-Massenspektrometrie-basierter Metabolomik entwickelt und in präklinischen Studien zu Krebsmedikamenten angewendet.

In der ersten Veröffentlichung wird die Optimierung der Probenvorbereitung für dreidimensionale multizelluläre Tumorsphäroide (3D MTS) Krebsmodelle vorgestellt. Ziel war es, eine geeignete Probenvorbereitungsmethode für Sphäroid-Zellkulturmodelle zu entwickeln, die mit LC-MS-basierter Metabolomik kompatibel ist. Eine besondere Herausforderung besteht darin, dass Sphäroide klein sind, einen Durchmesser von bis zu einem Millimeter haben und somit nicht nur mit bloßem Auge kaum sichtbar sind, sondern auch wesentlich weniger Biomaterial enthalten (nur einige 10.000 Zellen) als die herkömmlich verwendeten 2D-Monolayer-Zellkulturen. Der Arbeitsablauf wurde hinsichtlich des Extraktionsprotokolls, der Geschwindigkeit, der Waschschritte und der Mindestanzahl der benötigten Sphäroide optimiert. Das endgültige Protokoll ermöglicht einen beträchtlichen Durchsatz und Wiederholbarkeit (Reproduzierbarkeit), erfordert nur ein einziges Sub-mm-Sphäroid und kann leicht auf jede Zelllinie ausgeweitet werden, die dazu neigt, Sphäroide zu bilden. Schließlich wurde die Leistungsfähigkeit des Arbeitsablaufs in einem Proof-of-Principle-Experiment durch die Erstellung von Reaktionsprofilen von Sphäroiden demonstriert, die zwei verschiedenen krebsbekämpfenden Metallkomplexen, Oxaliplatin und BOLD-100/KP1339, ausgesetzt waren.

Anschließend wurde eine kombinierte, vollständig parallelisierte Metabolomik- und Lebendzellbildgebungsmethode entwickelt, um die Vorteile der Anwendung von Bildgebungstechnologien wie der Lebendzellbildgebung zur Ergänzung der Metabolomik aufzuzeigen und zu veranschaulichen, dass eine solche Anwendung machbar ist. Darüber hinaus haben wir in einem Proof-of-Concept-Experiment ein Profil der frühen oxidativen Stressreaktion nach einer kurzen (2 h) Wasserstoffperoxid-Exposition erstellt und gezeigt, wie die Bildgebungs- und Omics-Methodik Mängel und blinde Flecken gegenseitig kompensieren. Wir haben die Stärke des Arbeitsablaufs demonstriert, indem wir komplexe und dynamische biologische Prozesse wie die Fragmentierung des mitochondrialen Netzwerks als Reaktion auf den zunehmenden externen Wasserstoffperoxid-Zufluss untersucht haben. Ein besonderes Merkmal ist, dass es in der Lage ist, zahllose Effekte im Zusammenhang mit der Reaktion auf oxidativen Stress in der Frühphase gleichzeitig in einem einzigen Experiment zu rekapitulieren.

In der dritten Publikation untersuchten wir die metabolischen Grundlagen der erworbenen Resistenz in der HCT116-Zelllinie, wobei die erworbene Resistenz gegenüber dem etablierten Metalldroge Oxaliplatin und dem klinisch untersuchten BOLD-100/KP1339 untersucht wurde.

Wir nutzten experimentell quantifizierte absolute Metabolitenkonzentrationen (normalisiert auf den Gesamtproteingehalt), um metabolische Flüsse mit genomspezifischer metabolischer Modellierung und Flux-Balance-Analyse rechnerisch zu bestimmen. Für die vollständige Modellierung wurden die intrazellulären Metabolitenmengen mit der Veränderung der extrazellulären Metabolitenmengen während eines Zeitverlaufsexperiments ergänzt und die Wachstumsrate für alle Modelle ermittelt.

Was die Unterschiede zwischen den beiden Resistenzmodellen betrifft, so wurden die meisten Unterschiede bei den Stoffwechselflüsse im Fettsäure-, Aminosäure- und Nukleotidstoffwechsel festgestellt. Während die meisten dieser Stoffwechselwege in der Ru-basierten Resistenz aktiver sind, was darauf hindeutet, dass diese Zelllinie metabolisch aktiver ist, weisen Stoffwechselwege wie die Glykolyse und der Pentosephosphat-Stoffwechselweg in dem Pt-basierten Resistenzmodell höhere Flüsse auf.

Wir haben zum ersten Mal eine Stoffwechselmodellierung auf Genomebene und eine Flux-Balance-Analyse angewandt, um die erworbene Metallodrug-Resistenz für zwei zelluläre Modelle zu untersuchen, und wir haben mehrere Stoffwechseleffekte identifiziert, die bei Metallodrug-Resistenz üblich sind, sowie weitere, die spezifisch für die Art des Medikaments sind.

Table of Contents

Preamble and Introduction 1

Metabolomics: The omics-cascade, phenotype, and investigating biological systems 1

Technical challenges, instrumentation, and strategies 1

Sample preparation 3

Normalization 4

Understanding metabolomics data: from experiments to knowledge 4

Network analysis, genome-scale metabolic modeling, and flux-balance analysis 7

Metallodrugs 12

3D Multicellular tumor spheroids 13

References 16

Synopsis of the Publications 23

Results and Discussion 25

Conclusion 86

List of all peer-reviewed publications 89

Preamble and Introduction

Metabolomics: The omics-cascade, phenotype, and investigating biological systems

Metabolomics is an interdisciplinary science, which aims to measure all small molecules within biological systems and interpret these results from a system biology perspective. Since metabolites are the end-products of biological processes, they depend on the activity of genes and proteins and thus more directly mirror physiology (Fiehn, 2002). Due to this, metabolomics holds the potential to help tailor therapies to individuals, coined "precision medicine", by monitoring treatment and patient response (Frédérich et al., 2016; Puchades-Carrasco and Pineda-Lucena, 2017). This is possible since both drug metabolism and the state of the metabolome are highly dependent on various factors, such as genotype, environment, and age. The discovery of biomarkers and their clinical applications can also extend patient stratification, which is currently mostly focusing on genetic variants (Zhao et al., 2016). In addition, metabolic profiling might help disease prediction or early detection (Armitage and Southam, 2016; Fahrmann et al., 2019).

Beyond direct applications in therapies, metabolomics is a key tool to decipher the molecular background of several diseases (Deidda et al., 2018; Johnson et al., 2016), as well as biochemical concepts (Chen et al., 2020) and thereby promotes drug discovery (Armitage et al., 2018; Cavill et al., 2011). Despite the tremendous prospects to advance a new era of human medicine, metabolomics is an emerging field of science, compared to other historically more mature omics fields (such as genomics) and it faces several technical challenges and obstacles, which currently stand in the way to reach its full potential.

Technical challenges, instrumentation, and strategies

Compared with the analytes of other omics disciplines, such as nucleic acids or proteins and peptides, metabolites are from a chemical and physicochemical perspective extremely **diverse**. Even if we set apart lipidomics as a distinct subsection of metabolomics (Cajka and Fiehn, 2016), due to practical considerations, and make lipids exempt from the list of targets, other endogenous and exogenous metabolites still involve a wide variety of small molecules with various functional groups, chemical structures, and a broad range of polarity (Yanes et al., 2011). Furthermore, the typical **concentration ranges** differ by up to 8 orders of magnitude (Dunn, 2008). No single **instrumental platform** is universally adept to deal with these challenges simultaneously and provide the required sensitivity and selectivity.

Typically, nuclear magnetic resonance spectroscopy (NMR), flow injection mass spectrometry, gas chromatography-mass spectrometry (GC-MS), or liquid chromatography-mass spectrometry (LC-MS)

are used (Liu and Locasale, 2017). Generally, mass spectrometry dominates the field (Cajka and Fiehn, 2016), not least due to superb sensitivity enabling detection and quantification in the nM to pM range. Although it is also possible to couple LC to NMR spectroscopy (Emwas et al., 2019), coupling a separation technique to MS detection is more straightforward and has the advantage of resolving metabolites in time, thereby adding a piece of orthogonal information and reducing the complexity a detector is facing. In addition, using a separation technique lessens matrix effects and aids to identify artifacts from in-source fragmentation as well as distinguish isomers/isobars (Xu et al., 2015).

In targeted metabolomics, the aim is the quantification of a well-defined set of molecules through external calibration with commercially available standards. Typically, targeted metabolomics instrumentation involves a separation technique (such as LC or GC) coupled to a triple quadrupole mass spectrometer (QqQ) or quadrupole/linear ion trap (QLIT). These instruments operated in multiple reaction monitoring-mode (MRM) provide a high dynamic range (Griffiths et al., 2010). Moreover, compound-specific application of isotopically labeled internal standards spiked during the extraction step ensures the best reliability and enables absolute quantification. While targeted metabolomics the emphasis lays on quantification of a predefined known set of analytes, in nontargeted metabolomics relative quantification and identification of new compounds is the primary objective. For this purpose, high-resolution instruments are utilized in full MS acquisition, such as time-of-flight (TOF), quadrupole-time-of-flight (QTOF), or Orbitrap mass spectrometers with fragmentation capability for the acquisition of data-independent MS/MS spectra (Cajka and Fiehn, 2016).

The Metabolite Identification Task Group of the Metabolomics Society proposes a guideline with 7 levels of certainty for **identification** denoted with letters of the alphabet from A to G (Rampler et al., 2021) as a revision of the previous nomenclature conceived by the Chemical Analysis Working Group of the Metabolomics Standard Initiative describing level 1 to 4 certainty in metabolite annotation and identification (Chaleckis et al., 2019; Salek et al., 2013). In the newly proposed system, the letter “A” denotes the highest degree of confidence in the identity of the metabolite, where even the stereochemistry is clear (e.g. L-Isoleucine vs D-Isoleucine). While a typical untargeted metabolomics study can have a varying degree of confidence in the identity of analytes of interest, LC-MS-based targeted metabolomics studies typically achieve level B or C highest despite utilizing authentic standards, as deciphering stereochemistry with mainstream separation techniques is not possible. Thus, the quantified metabolite amount is a mixture of diastereomers (Isoleucine and *allo*-Isoleucine), but generally, it is assumed, that depending on the origin of the sample, we quantify the most ubiquitous, such as L-amino acids and D-sugars.

From a technical point of view regarding sum formula generation and structure determination with mass spectrometry, mass accuracy is crucial, so are isotopic patterns (Kind and Fiehn, 2007). Also, reliable and abundant mass spectral compound libraries are key. Here, *in-silico* generated fragment spectra are prevalent, while only a fraction of known molecules has pure chemical standard-based experimental spectra, constituting relevant gaps in the human metabolism (Frainay et al., 2018).

Although targeted and non-targeted metabolomics are remarkably different in their aims, prerequisites, and strengths (Roberts et al., 2012) as non-targeted analysis aids hypothesis generation and discovery, while targeted methodology rather supports hypothesis validation. Despite this, it is possible and advantageous to merge such methods by establishing a targeted method on a high-resolution instrument so some compounds can be quantified strictly targeted, and additionally, this set can be expanded by metabolites assessed with a non-targeted approach (Cajka and Fiehn, 2016).

Sample preparation

LC-MS-based metabolomics analysis of cellular samples requires solid-liquid **extraction** from the biological material. To obtain a true snapshot of the intracellular metabolism efficient quenching is required to stop the metabolism instantly, without loss or degradation of the metabolites. For the effective extraction and broad coverage of metabolites, solvent polarity, pH and temperature can be all optimized (Dietmair et al., 2010; Yanes et al., 2011). As leakage of metabolites upon quenching the metabolism can be a problem (Canelas et al., 2008), cellular metabolomics protocols can combine quenching and extraction into a single step.

Despite the vast number of metabolites present in biological systems, it is hard to achieve a fully comprehensive and quantitative method, even when multiple instrumental platforms, extraction and sample preparations strategies, or multidimensional chromatography techniques are applied (Coman et al., 2016; Schwaiger et al., 2018; Viant et al., 2017). Sophisticated approaches, like credentialing with stable isotope-labeled biomass (Mahieu et al., 2014) can help identify features with biological origin vs. background noise, and thereby substantially reduce the amount of information to be processed (and enables focus on the relevant features) (Mahieu and Patti, 2017).

We can conclude, that a fully unbiased, global single metabolomics experiment which can comprehensively measure and quantify the metabolome of an organism is not possible even with state-of-the-art sample preparation, instrumentation, and analytical method (Viant et al., 2017). The applied techniques inevitably infer some degree of bias towards analyte classes with particular properties. Increasing selectivity, coverage, and throughput simultaneously of a particular workflow can be incompatible objectives (Ortmayr et al., 2016; Rampler et al., 2021). These aspects need to be carefully considered during the experimental design and interpretation of the results alike.

Normalization

Normalization is a key aspect of quantitative metabolomics analysis, both for *in vivo* and *in vitro* studies. For instance, in cell biological experiments, the number of cells recovered after the experiment varies due to inaccuracy in seeding, inherent differences in grow treatment conditions. The aim is to normalize within-sample variation of the same group and it should correlate with the concentration of metabolites within the same group. The suitable normalization method of choice is strongly dependent on the sample type: for urine samples creatine concentration or osmolarity is routinely used, while MS "total useful signal" (MSTUS) uses the combined intensity of all peaks and is universally applicable while for serum or plasma. Also, dry weight, UV absorbance, conductivity, cell count are possible factors for normalization (Wu and Li, 2016). Furthermore, considering the degree of ion-suppression (matrix-induced ion suppression or MIIS (Chen et al., 2015)), total protein or total DNA content, metabolic markers (such as inositol and pantothenate) (Cao et al., 2011), and "housekeeping metabolites" or UV absorbance after dansylation of phenols and primary amines (Wu and Li, 2014) is also an option.

Although determining the cell count would be the most direct measure to normalize cell extracts for metabolomics experiments, it is rarely done with adherently growing cells due to practical reasons. Unfortunately, cell counting needs to be done upon harvesting the cells and just before extraction. As harvesting to detach cells from the vessel by enzymatic dissociation (such as with trypsin) itself is a stressful event for the cells due to the proteolytic activity of the enzyme, it causes metabolites leakage and might introduce artifacts, rendering it insufficient for metabolomics studies (Dettmer et al., 2011; Huang et al., 2010). Due to this reason metabolism is often quenched by stopping all enzymatic activity and the metabolites are subsequently extracted, as this avoids a delayed sample preparation.

Understanding metabolomics data: from experiments to knowledge

The **pipeline** of metabolomics experiments is complex and contains several distinct phases in order to fit a top-down approach (Brown et al.; Rosato et al., 2018). In the first step, an appropriate study design is conceived to address concrete, testable biological questions. The biological experiment, suitable sample collection, and preparation are performed (Dunn et al., 2012). Subsequently, the measurement series is carried out with the instrumental setup of choice and the raw data is produced. Next, the data needs to be preprocessed: normalization, feature scaling, missing value imputation, filtering for outliers (both in sample or feature level), data reduction can be carried out. Although data processing can be carried out in an iterative manner by reprocessing the raw data, it is critical for obtaining an accurate classification performance (Gromski et al., 2014, 2015). Once the cleaned, final

dataset is available, a wide variety of unsupervised, supervised methods as well as descriptive analysis can be applied (Liebal et al., 2020).

It is important to note, that each step is crucial in the pipeline (both wet lab and dry lab) and can hinder capturing insight about the biological system or perturbation. The very first step is the experimental design. Here, proper controls need to be prepared for all known experimental variables. To avoid possible confounding effects, blocking can be used. By generating homogeneous experimental units, it is possible to isolate and focus on the variation related to the research question and study design, rather than on variation introduced by pre-analytical aspects related to sample collection and batch effects (Yin et al., 2013). In addition to these efforts randomization strategies (Kang et al., 2008) along multiple axes of experimental parameters (biological experiment, sample collection, preparation, measurement sequence, etc.) might help deal with unknown confounding effects or when blocking is not possible (Wehrens and Salek 2019). Controlling confounding factors by the choice of appropriate controls, such as the time, environment, analysis method, and operator. Once such confounding factors have been identified, randomization and blocking can help. By blocking, we group based on confounding factors and investigate within block variability, and compare it to the design-related variability (Kang et al., 2008).

The number of biological replicates required to reach a desired statistical power can be also assessed prior to the experiment, although it is not trivial, especially in nontargeted metabolomics, where the number of features might be unclear before the measurement. Still, based on data simulation and permutation, it is possible to estimate the sample size (Nyamundanda et al., 2013).

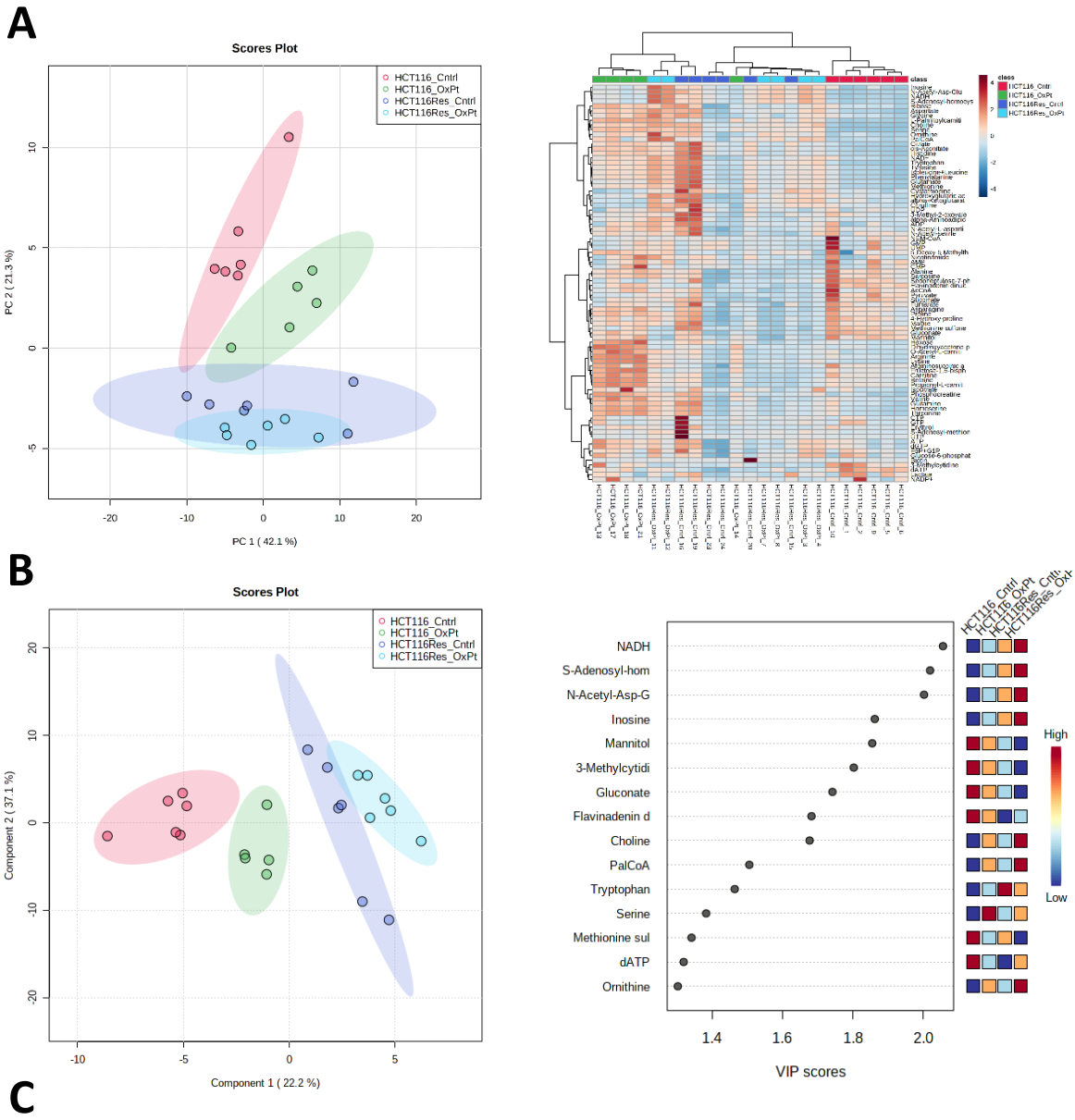

C

Pathway Name	Match Status	p	-log(p)	Holm p	FDR
Glycolysis / Gluconeogenesis	5/26	1.0568E-6	5.976	5.6012E-5	3.7452E-5
Glycerophospholipid metabolism	2/36	1.4133E-6	5.8498	7.349E-5	3.7452E-5
Glycerolipid metabolism	1/16	3.065E-6	5.5136	1.5631E-4	5.4148E-5
Pentose phosphate pathway	4/22	8.7682E-6	5.0571	4.3841E-4	9.6669E-5
Fructose and mannose metabolism	2/20	9.1197E-6	5.04	4.4687E-4	9.6669E-5
Glycine, serine and threonine metabolism	7/33	7.1495E-5	4.1457	0.0034318	5.582E-4
Biotin metabolism	2/10	7.3725E-5	4.1324	0.0034651	5.582E-4
Pantothenate and CoA biosynthesis	3/19	2.0509E-4	3.688	0.0094343	0.0013587
beta-Alanine metabolism	3/21	2.7886E-4	3.5546	0.012549	0.0016422
Galactose metabolism	1/27	4.886E-4	3.311	0.021499	0.0025896
Arginine biosynthesis	9/14	7.7264E-4	3.112	0.033223	0.0036174
Citrate cycle (TCA cycle)	9/20	9.0351E-4	3.0441	0.037948	0.0036174

Pathway Name	Match Status	p	-log(p)	Holm p	FDR
Riboflavin metabolism	1/4	5.4157E-4	3.2663	0.028703	0.026452
Cysteine and methionine metabolism	6/33	0.0010665	2.972	0.055459	0.026452
Tryptophan metabolism	2/41	0.0014973	2.8247	0.076361	0.026452
Fatty acid degradation	4/39	0.0059878	2.2227	0.29939	0.074152
Glycine, serine and threonine metabolism	7/33	0.0069954	2.1552	0.34278	0.074152
Glycerophospholipid metabolism	2/36	0.013872	1.8578	0.66588	0.097498
Alanine, aspartate and glutamate metabolism	13/28	0.014444	1.8403	0.67888	0.097498
beta-Alanine metabolism	3/21	0.01747	1.7577	0.80363	0.097498
Tyrosine metabolism	3/42	0.019074	1.7196	0.85831	0.097498
Citrate cycle (TCA cycle)	9/20	0.021156	1.6746	0.93087	0.097498
Selenocompound metabolism	1/20	0.025671	1.5906	1.0	0.097498
Ubiquinone and other terpenoid-quinone biosynthesis	1/9	0.026109	1.5832	1.0	0.097498

Figure 1 Result of distinct data analysis methods to evaluate metabolomics experiments. Parental oxaliplatin-sensitive HCT116 cell line ("HCT116_Cntrl"), this cell line treated with 20 µM oxaliplatin for 24 h ("HCT116_OxPt"), HCT116 with acquired oxaliplatin-resistance ("HCT116Res_Cntrl") and this cell line with oxaliplatin treatment ("HCT116Res_OxPt") were investigated with (A) PCA and heatmap (hierarchical clustering), (B) Partial least squares-discriminant analysis (PLS-DA) and respective VIP scores of influential compounds, (C) pathway analysis with the most perturbed and impacted pathways for oxaliplatin treatment (left) and acquired resistance (right). Analysis with MetaboAnalyst 4.0 (Chong et al., 2019).

Metabolomics being the cellular end-point of biological processes enables a **top-down approach**, focusing on the interaction of multiple metabolites, which is in contrast to (the historically more prevalent) reductionist approach in molecular and cellular biology trying to attribute functions to a single molecule (Barabási and Oltvai, 2004). In order to capture such interactions and aid the interpretation of the results in a biological context, metabolomics data analysis relies heavily on the methods of multivariate statistics, supervised and unsupervised methods, network inference, metabolic modeling, metabolite and pathway enrichment techniques. It is beyond the scope of this introduction to my dissertation to discuss these methodologies in detail, however, I explored the subject in our review article "Recurrent Topics in Mass Spectrometry-Based Metabolomics and Lipidomics - Standardization, Coverage, and Throughput" (Rampler et al., 2021) to which I contributed the chapter dealing with data analysis and visualization, metabolic networking and databases and in the following, I briefly recapitulate and touch on these subjects. Downstream analysis of mass spectrometry data typically starts with exploratory data analysis. Uni- and multivariate methods are applied, among others unsupervised techniques like principal component analysis (PCA) or hierarchical clustering (Figure 1A), since these methods are not prone to overfitting as they don't require labeled, classified data in contrast to supervised learning techniques. Once exploratory data analysis confirmed that the strongest underlying differences are study design-related, supervised techniques, such as partial least squares-discriminant analysis (PLS-DA) (Figure 1B) or logistic regression (Fahrmann et al., 2019) can be applied to search for biomarkers of the investigated phenotype. Although these statistical and machine learning algorithms are certainly powerful, they are not using any biological knowledge about the relationship of the investigated metabolites. Pathway information can be utilized with overrepresentation analysis (ORA) using metabolite lists, metabolite set enrichment analysis (MSEA) with quantitative information about metabolites. Moreover, pathway enrichment and topology analysis (Figure 1C) takes both the degree of change and the position of the affected metabolite within the pathway into account to calculate enrichment and perturbation, respectively.

Network analysis, genome-scale metabolic modeling, and flux-balance analysis

Genome-scale metabolic representations require a known set of reactions, annotated genes, enzymes, proteins, and metabolites (Bordbar et al., 2014). It is possible to map significantly altered metabolites upon such a metabolic network and extract a subnetwork, a (hyper-)graph whose nodes and edges are a subset of nodes and edges of the original larger graph or network. This can enhance the biological interpretation and bring closer to potentially finding a mechanistic explanation, as the

resulting network will be an appropriate condensed representation of the investigated phenotype (Frainay and Jourdan, 2017).

Biological **networks**, such as metabolic networks approximate generally a scale-free topology, lacking a typical, representative node (Bordbar et al., 2014) and therefore have higher average clustering coefficients, consequently few nodes act as hubs, having high connectivity. Moreover, metabolic networks are dissociative, the highly linked hubs are rarely directly linked to each other and they are quite robust against random failure, as such can be tempered with alternative reactions. Such a topology can be explained with the mechanisms of gradual network growth, and indeed nodes that emerged early in the course of evolution tend to be highly connected (Wagner and Fell, 2001).

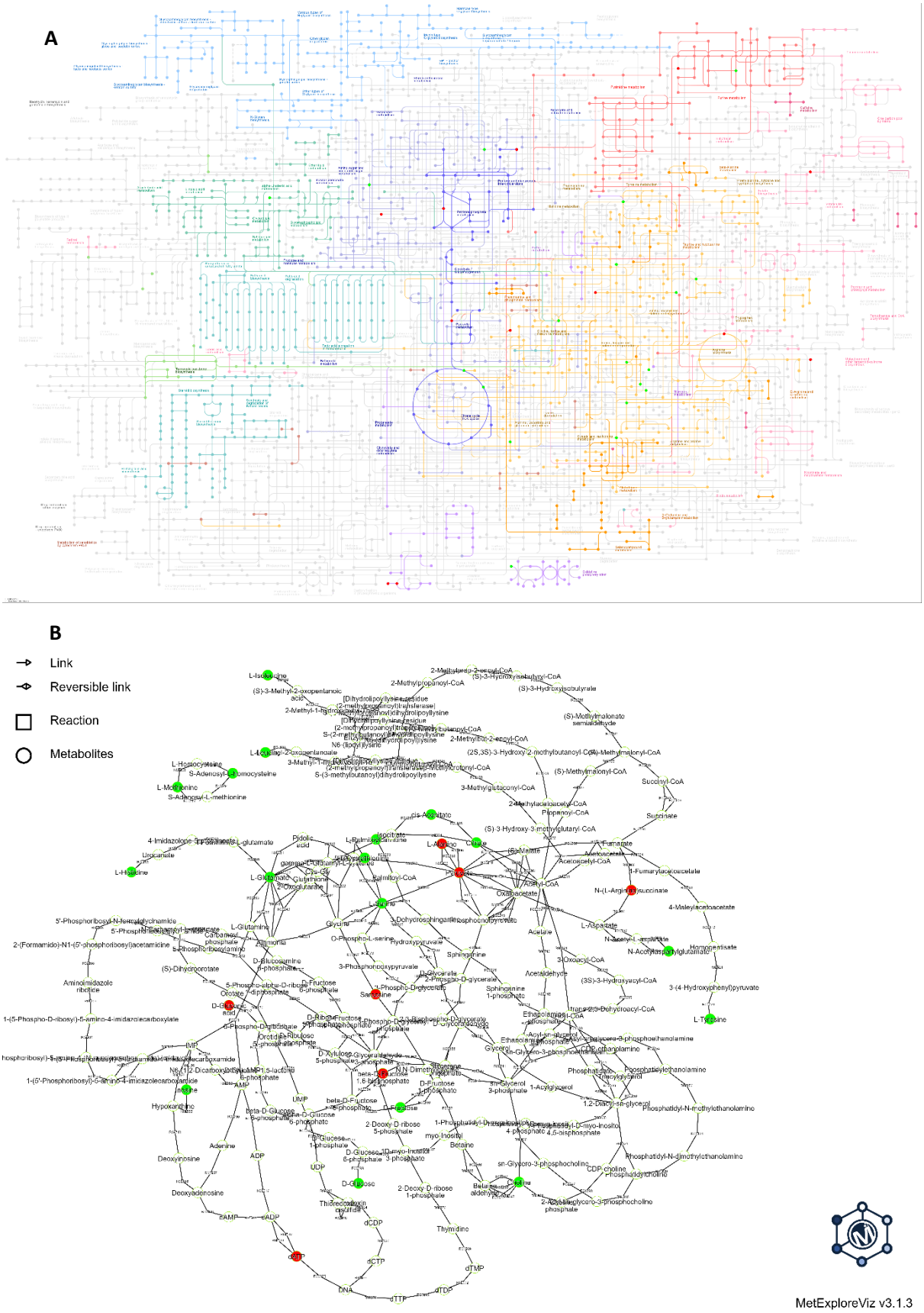

Figure 2 Significantly changed metabolites (adjusted P-value < 0.05) upon acquired oxaliplatin-resistance in HCT116 cell line as described in (Herrmann-Rusz et al.), mapped on (A) KEGG (Kanehisa and Goto, 2000) with MetaboAnalyst (Chong et al., 2019) and (B) the corresponding extracted subnetwork which contains all significantly changed metabolites and side-compounds are removed. Green nodes are upregulated, red nodes are downregulated metabolites, respectively. Created with MetExplore (Chazalviel et al., 2018; Cottret et al., 2018).

The importance of these highly connected metabolites, such as ATP is undisputed, as they participate in a plethora of reactions. However, in the metabolic network analysis software tool **MetExplore** (Chazalviel et al., 2018; Cottret et al., 2018), there is a particular emphasis to avoid ascribing too much significance to hub molecules within the metabolic network. Upon extraction of subnetworks based on significantly altered metabolites, the algorithm connects all participating nodes via the shortest and lightest paths, which is defined by the squares of the degrees of the nodes, which the shortest path traverses. The union of all shortest and lightest paths defines the subnetwork and removes all side-compounds, thereby removing noise and delivering a relevant representation corresponding to the investigated phenotype (Figure 2).

Although metabolomics holds a prominent position in the omics cascade, it can certainly benefit from complementing with results from other omics modalities. Multi-omics integration, such with transcriptomics can reveal information about part of the metabolism, where the metabolomics experiment has little coverage, thereby extending our perspective about the phenotype (Karnovsky et al., 2012). A particular strength of such datasets is that they enable inspection of regulation of the phenotype. Although there is no direct link between metabolites and transcripts, these two omics modalities are complementary and integration is highly advantageous, as opposed to separate analysis (Cavill et al., 2016). Co-regulation analysis is both possible with correlation-based network analysis as well as topological analysis of biological networks, which take advantage of available biological knowledge of reactions and pathways (Eicher et al., 2020). Only a fraction of metabolites might be significantly changed within a particular pathway, like in the TCA cycle in Figure 3, but beyond the two metabolites *cis*-aconitate and citrate, the transcript of the rate-limiting enzyme Isocitrate dehydrogenase (IDH) is also significantly upregulated, along with significant changes of other transcripts. Even though, such studies can identify important perturbed pathways for the phenotype, help dissect their regulation and find possible biomarkers, to come closer to elucidate the metabolic basis of diseases, discover possible metabolic vulnerabilities of cancer types, it is necessary to obtain a quantitative picture of pathway activities and rate of metabolic reactions.

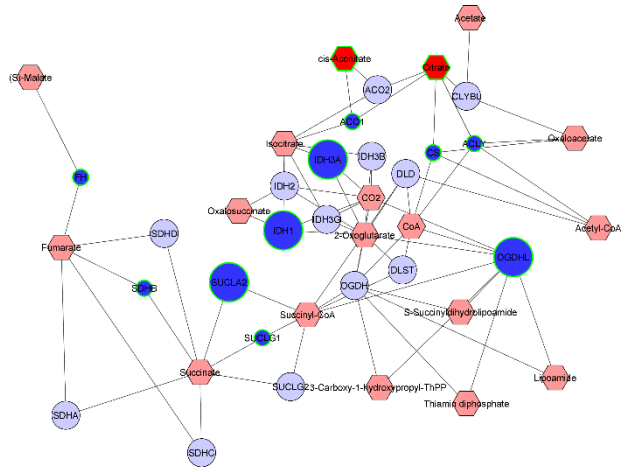

Figure 3 Perturbations upon the emergence of acquired oxaliplatin resistance in the HCT116 cell line: Compound-gene metabolic network of TCA cycle integrating metabolomics with transcriptomics results, after statistical, pathway-based integration with KEGG data, following a repeated study design. Created with MetScape (Karnovsky et al., 2012), a Cytoscape (Shannon et al., 2003) plugin.

Flux-based genome-scale metabolic modeling (GSMM) investigates the flux-model distributions of chemical reactions, a rate of turnover of molecules through a particular metabolic reaction or pathway, typically in [mmol/g DW/h] units. Such fluxes cannot be measured directly like the metabolite abundance, but stable isotope substrates are required in a time-resolved experiment to infer indirectly (Antoniewicz, 2013; Jang et al., 2018). If a quasi-steady-state is assumed, internal metabolite concentrations are constant, and this enables to carry out flux balance analysis (FBA), by setting the product of the stoichiometric matrix and the vector of flux values to zero, rendering it to be a homogeneous system of linear equations, determining the corresponding upper and lower bounds of flux for the corresponding flux (Orth et al., 2010).

The stoichiometric matrix contains the stoichiometric coefficients of the reactions, thereby including biochemical knowledge. In addition, it is possible to further constrain the solution space by removing physicochemically infeasible network states, adding reversibility conditions. Introducing an objective function such as the assumption that cancer cells try to maximize growth can select a single possible solution (Heirendt et al., 2019). Since a GSMM contains annotations about multiple omics systems, we can set additional assumptions and heuristics to use any corresponding omics data to constrain the model. Moreover, parsimonious FBA constructs a flux balance distribution with the minimum total sum of flux in the system to deal with multiple feasible solutions and loops (Orth et al., 2010). Once determined, the upper and lower bounds of the fluxes through biochemical reactions, which are resulting from the combination of experimental data (e.g. measured exchange rates) and computational approaches can then be used to investigate the phenotype.

Isotopic labeling experiments, flux analysis and GSMM have their primary application in biotechnology and metabolic engineering, in the improvement of cell factories for synthetic biology, such as increasing yield of the product, coupling the pathway activity to growth or development of production pathways upon genetic modification of microbial organisms. (Antoniewicz, 2013; Jouhten, 2012). Although GSMM and flux-balance analysis in cancer research had been successfully applied in the past (Jalili et al., 2021; Jia et al., 2019; Nilsson and Nielsen, 2017), it had been an established approach in industrial biotechnology before and several aspects will be first investigated as high-quality experimental data will be available. *In silico* studies of cancer metabolism based on state-of-the-art measurements and materials like isotopically labeled standards, open new insights and may also reduce the need for *in vitro*, *in vivo* experiments (and thereby sacrificing animals) thus potentially saving costs while revealing highly informative results.

Metallodrugs

Metals are used in a variety of applications, as therapeutic agents as well as diagnostics (J. Anthony et al., 2020; Komeda and Casini, 2012; Mjos and Orvig, 2014). Although most clinically approved drugs are organic molecules, metal complexes dominate cancer chemotherapy. Due to the widespread application of the three worldwide approved platinum-based drugs cisplatin, carboplatin and oxaliplatin (Kelland, 2007), actually about half of the chemotherapy schemes applied contain a platinum drug (Johnstone et al., 2014).

Despite their success, Pt complexes suffer from several drawbacks, such as severe side effects (nephro-, neuro-, ototoxicity, suppression of bone marrow, etc.) as a consequence of limited specificity to the target DNA (of cancer cells), the development of acquired resistance and the limited application profile through intrinsic resistance of several tumor types (Kelland, 2007).

The success of Pt drugs, as well as their shortcomings, encouraged the investigation of polynuclear Pt(II) complexes (Billecke et al., 2006), Pt(IV)-based molecules (Gibson, 2019) and compounds with alternative central transition metals. Since the side effects of square-planar Pt(II) complexes are a result of high reactivity to biomolecules beyond the primary target DNA, octahedral Pt(IV) complexes are investigated, which show lower cytotoxicity unless they are reduced to more active Pt(II) species (accompanied by elimination of the axial ligands), taking advantage of the more reductive and acidic milieus of solid tumors. Beyond reduced side effects, this might enable oral administration, opposed to the intravenous administration of currently established Pt drugs. Alternative coordination complexes with anticancer activity exist with Ru, Os (Meier-Menches et al., 2018), Au (Bertrand and Casini, 2014; Karaca et al., 2017), Ga, Sn, Ti (Ellahioui et al., 2017), As (Khairul et al., 2017), Pd (Vojtek et al., 2019), Rh, Ir (Almodares et al., 2014).

The interest in compounds beyond the platinum class is motivated by several factors: First of all, potent drugs with a differing mechanism of action have the potential to be efficient against tumors where established Pt-drugs fail due to intrinsic resistance, and they could complement Pt-based therapies. Although there are certainly effects common to many metal complexes with anticancer activity, such as the direct or indirect modulation of redox status, there is indeed strong evidence for a wide variety of alternative mechanisms of action: Au complexes inhibiting thioredoxin reductase (Karaca et al., 2017), thereby interfering with the redox state of mitochondrial functions, or Ru complexes targeting the cytoskeleton linker protein plectin (Meier et al., 2017) or down-regulating GRP78 and thus affecting ER stress defense and impeding metastatic potential (Gifford et al., 2016). In addition, several non-platinum metal complexes display a prodrug behavior such as the reduction of Ru(III) complexes to more reactive Ru(II) species, resulting in a mild toxicity profile and selective activation. Further possible strategies for the application of transition metal complexes in human medicine involve photodynamic therapy (PDT), photothermal therapy, photochemotherapy (PCT) (J. Anthony et al., 2020; Monro et al., 2019) and drug activation by tumor-associated enzymes (Tromp et al., 2004).

Despite the success and prominence of certain metal complexes in oncology, only three platinum-based (cisplatin, carboplatin, oxaliplatin) and one non-platinum metal compound (arsenic trioxide) have been globally approved for clinical use, with the latest approval dating back 20 years ago. On the one hand, the limited ability of (monolayer cell culture-based) *in vitro* cytotoxicity assays to predict clinical efficacy can be blamed for the high failure rate of novel compounds in clinical translation. On the other hand, the lack of “prospectively validated biomarkers” complicates evaluation both at preclinical and clinical stages (Pötsch et al., 2019). Consequently, there are high incentives behind improving preclinical screening and developing methodologies capable of finding reliable biomarkers.

Although there is a large body of knowledge available for metallodrugs, it is clear that they operate through a multimodal mechanism of action and our understanding is not yet complete (Gibson, 2009). Most of the studies focused on the chemistry of the compounds (hydrolysis, ligand exchange), element speciation, structure-activity relationships, reactions with biomolecules, pharmacokinetics and bioavailability. While cell-free assays provided great service, many of these processes require more complex models for investigation, such as the presence of multiple cell layers, hypoxia (for drug activation) or even an immune system (Englinger et al., 2018; Holtkamp, 2018; Terenzi et al., 2016).

3D Multicellular tumor spheroids

In vitro tumor models are an important pillar of the preclinical oncology drug **discovery** process, as novel drug candidates are routinely screened on such models in high-throughput screening (HTS)

(Langhans, 2018), before progressing to more complex models such as cell-line- or patient-derived xenografts in immunocompromised mice (Katt et al., 2016; Yoshida, 2020).

Multicellular tumor spheroids (MTS) can be grown on special plates from established cell lines similar to 2D monolayer cell cultures. However, they capture more features of tumors than monolayer cell cultures, such as gradients of oxygen and nutrients. 3D MTS display three distinct zones with actively proliferating, quiescent and necrotic cells. As such a **microenvironment** drastically alters cellular metabolism through transcriptional master regulators such as HIF1α (Tafani et al., 2016), there is a substantial discrepancy in the behavior projected by 2D cell cultures and *in vivo* tumors (Edmondson et al., 2014; Stock et al., 2016). A key feature of spheroids is the presence of a hypoxic zone, which is especially relevant for the investigation of metal complexes with anticancer activity, as many of them are activated upon reduction under hypoxia. In addition, tumors have a higher barrier against the mass transfer of anticancer drugs as well, which makes it harder for drugs to penetrate to the inner cells. Monolayer cell cultures are not capable of mimicking these aspects and are therefore prone to deliver false positives in drug screening assays. Beyond simple resistance to mass transfer of the drug, the heterogeneous cell population of a MTS entails different cellular behavior, and the high proportion of dormant cells implies that not only drugs predominantly affecting proliferating cells will deliver positive results.

Although cytotoxicity tests based on metabolic viability, such as the MTT, Alamar Blue, or CellTiter-Glo assays, are the most commonly applied for the identification of potential drug candidates via HTS (Hamid et al., 2004; Nakayama et al., 1997), there have been attempts to incorporate metabolomics into preclinical antitumor drug discovery HTS procedures (Close et al., 2019; Wang et al., 2020). Advances in bioanalytical technologies, top-down cellular assays and omics technologies (transcriptomics, proteomics screening) finally enable a high-throughput manner in metallodrug research to study physiological responses and multifaceted mechanisms, like the ability to exert immunomodulatory effects and their interactions.

We hold that the application of global, unbiased metabolomics is just entering the research of metal complexes, and we are convinced that understanding metabolism will reveal new insights into its regulation, its cross-talk with the epigenome (Li et al., 2020) and binding targets will help to tackle intrinsic and acquired resistance and steer further development and synthesis of novel compounds and fine-tune their application. Here, we expand the toolkit of metallodrug research by establishing an innovative sample preparation workflow for advanced *in vitro* tumor models (multicellular tumor spheroids) and by applying advanced tools such as GSMM and flux balance analysis for the first time to decipher the metabolic mechanisms behind metallodrug resistance. Furthermore, we present a

combined imaging-metabolomics workflow, which allows studying the oxidative stress response, a key feature relevant for common cellular effects of metal complexes.

References

Almodares, Z., Lucas, S.J., Crossley, B.D., Basri, A.M., Pask, C.M., Hebden, A.J., Phillips, R.M., and McGowan, P.C. (2014). Rhodium, Iridium, and Ruthenium Half-Sandwich Picolinamide Complexes as Anticancer Agents. Inorg. Chem. *53*, 727–736.

Antoniewicz, M.R. (2013). 13C metabolic flux analysis: optimal design of isotopic labeling experiments. Current Opinion in Biotechnology *24*, 1116–1121.

Armitage, E.G., and Southam, A.D. (2016). Monitoring cancer prognosis, diagnosis and treatment efficacy using metabolomics and lipidomics. Metabolomics *12*.

Armitage, E.G., Godzien, J., Peña, I., López-Gonzálvez, Á., Angulo, S., Gradillas, A., Alonso-Herranz, V., Martín, J., Fiandor, J.M., Barrett, M.P., et al. (2018). Metabolic Clustering Analysis as a Strategy for Compound Selection in the Drug Discovery Pipeline for Leishmaniasis. ACS Chem. Biol. *13*, 1361–1369.

Barabási, A.-L., and Oltvai, Z.N. (2004). Network biology: understanding the cell's functional organization. Nature Reviews Genetics *5*, 101–113.

Bertrand, B., and Casini, A. (2014). A golden future in medicinal inorganic chemistry: the promise of anticancer gold organometallic compounds. Dalton Transactions *43*, 4209–4219.

Billecke, C., Finniss, S., Tahash, L., Miller, C., Mikkelsen, T., Farrell, N.P., and Bögler, O. (2006). Polynuclear platinum anticancer drugs are more potent than cisplatin and induce cell cycle arrest in glioma1. Neuro-Oncology *8*, 215–226.

Bordbar, A., Monk, J.M., King, Z.A., and Palsson, B.O. (2014). Constraint-based models predict metabolic and associated cellular functions. Nat Rev Genet *15*, 107–120.

Brown, M., Dunn, W.B., Ellis, D.I., Goodacre, R., Handl, J., and Knowles, J.D. A metabolome pipeline: from concept to data to knowledge. 13.

Cajka, T., and Fiehn, O. (2016). Toward Merging Untargeted and Targeted Methods in Mass Spectrometry-Based Metabolomics and Lipidomics. Anal. Chem. *88*, 524–545.

Canelas, A.B., Ras, C., Pierick, A. ten, Dam, J.C. van, Heijnen, J.J., and Gulik, W.M. van (2008). Leakage-free rapid quenching technique for yeast metabolomics. Metabolomics *4*, 226–239.

Cao, B., Aa, J., Wang, G., Wu, X., Liu, L., Li, M., Shi, J., Wang, X., Zhao, C., Zheng, T., et al. (2011). GC–TOFMS analysis of metabolites in adherent MDCK cells and a novel strategy for identifying intracellular metabolic markers for use as cell amount indicators in data normalization. Anal Bioanal Chem *400*, 2983–2993.

Cavill, R., Kamburov, A., Ellis, J.K., Athersuch, T.J., Blagrove, M.S.C., Herwig, R., Ebbels, T.M.D., and Keun, H.C. (2011). Consensus-Phenotype Integration of Transcriptomic and Metabolomic Data Implies a Role for Metabolism in the Chemosensitivity of Tumour Cells. PLOS Computational Biology *7*, e1001113.

Cavill, R., Jennen, D., Kleinjans, J., and Briedé, J.J. (2016). Transcriptomic and metabolomic data integration. Brief Bioinform *17*, 891–901.

Chaleckis, R., Meister, I., Zhang, P., and Wheelock, C.E. (2019). Challenges, progress and promises of metabolite annotation for LC–MS-based metabolomics. Current Opinion in Biotechnology *55*, 44–50.

Chazalviel, M., Frainay, C., Poupin, N., Vinson, F., Merlet, B., Gloaguen, Y., Cottret, L., and Jourdan, F. (2018). MetExploreViz: web component for interactive metabolic network visualization. Bioinformatics *34*, 312–313.

Chen, G.-Y., Liao, H.-W., Tsai, I.-L., Tseng, Y.J., and Kuo, C.-H. (2015). Using the Matrix-Induced Ion Suppression Method for Concentration Normalization in Cellular Metabolomics Studies. Anal. Chem. *87*, 9731–9739.

Chen, M., Yang, J., Li, L., Hu, Y., Lu, X., Sun, R., Wang, Y., Wang, X., and Zhang, X. (2020). Metabolomics Reveals that Cysteine Metabolism Plays a Role in Celastrol-Induced Mitochondrial Apoptosis in HL-60 and NB-4 Cells. Scientific Reports *10*, 471.

Close, D.A., Wang, A.X., Kochanek, S.J., Shun, T., Eiseman, J.L., and Johnston, P.A. (2019). Implementation of the NCI-60 Human Tumor Cell Line Panel to Screen 2260 Cancer Drug Combinations to Generate >3 Million Data Points Used to Populate a Large Matrix of Anti-Neoplastic Agent Combinations (ALMANAC) Database. SLAS DISCOVERY: Advancing the Science of Drug Discovery *24*, 242–263.

Coman, C., Solari, F.A., Hentschel, A., Sickmann, A., Zahedi, R.P., and Ahrends, R. (2016). SIMPLEX: a combinatorial multimolecular omics approach for systems biology. Molecular & Cellular Proteomics.

Cottret, L., Frainay, C., Chazalviel, M., Cabanettes, F., Gloaguen, Y., Camenen, E., Merlet, B., Heux, S., Portais, J.-C., Poupin, N., et al. (2018). MetExplore: collaborative edition and exploration of metabolic networks. Nucleic Acids Res *46*, W495–W502.

Deidda, M., Noto, A., Bassareo, P.P., Cadeddu Dessalvi, C., and Mercuro, G. (2018). Metabolomic Approach to Redox and Nitrosative Reactions in Cardiovascular Diseases. Front. Physiol. *9*.

Dettmer, K., Nürnberger, N., Kaspar, H., Gruber, M.A., Almstetter, M.F., and Oefner, P.J. (2011). Metabolite extraction from adherently growing mammalian cells for metabolomics studies: optimization of harvesting and extraction protocols. Anal Bioanal Chem *399*, 1127–1139.

Dietmair, S., Timmins, N.E., Gray, P.P., Nielsen, L.K., and Krömer, J.O. (2010). Towards quantitative metabolomics of mammalian cells: Development of a metabolite extraction protocol. Analytical Biochemistry *404*, 155–164.

Dunn, W.B. (2008). Current trends and future requirements for the mass spectrometric investigation of microbial, mammalian and plant metabolomes. Phys. Biol. *5*, 011001.

Dunn, W.B., Wilson, I.D., Nicholls, A.W., and Broadhurst, D. (2012). The importance of experimental design and QC samples in large-scale and MS-driven untargeted metabolomic studies of humans. Bioanalysis *4*, 2249–2264.

Edmondson, R., Broglie, J.J., Adcock, A.F., and Yang, L. (2014). Three-Dimensional Cell Culture Systems and Their Applications in Drug Discovery and Cell-Based Biosensors. Assay Drug Dev Technol *12*, 207–218.

Eicher, T., Kinnebrew, G., Patt, A., Spencer, K., Ying, K., Ma, Q., Machiraju, R., and Mathé, E.A. (2020). Metabolomics and Multi-Omics Integration: A Survey of Computational Methods and Resources. Metabolites *10*, 202.

Ellahioui, Y., Prashar, S., and Gómez-Ruiz, S. (2017). Anticancer Applications and Recent Investigations of Metallodrugs Based on Gallium, Tin and Titanium. Inorganics *5*, 4.

Emwas, A.-H., Roy, R., McKay, R.T., Tenori, L., Saccenti, E., Gowda, G.A.N., Raftery, D., Alahmari, F., Jaremko, L., Jaremko, M., et al. (2019). NMR Spectroscopy for Metabolomics Research. Metabolites *9*, 123.

Englinger, B., Pirker, C., Heffeter, P., Terenzi, A., Kowol, C.R., Keppler, B.K., and Berger, W. (2018). Metal Drugs and the Anticancer Immune Response. Chemical Reviews.

Fahrmann, J.F., Bantis, L.E., Capello, M., Scelo, G., Dennison, J.B., Patel, N., Murage, E., Vykoukal, J., Kundnani, D.L., Foretova, L., et al. (2019). A plasma-derived protein-metabolite multiplexed panel for early-stage pancreatic cancer. Journal of the National Cancer Institute *111*.

Fiehn, O. (2002). Metabolomics – the link between genotypes and phenotypes. Plant Mol Biol *48*, 155–171.

Frainay, C., and Jourdan, F. (2017). Computational methods to identify metabolic sub-networks based on metabolomic profiles. Briefings in Bioinformatics *18*, 43–56.

Frainay, C., Schymanski, E.L., Neumann, S., Merlet, B., Salek, R.M., Jourdan, F., and Yanes, O. (2018). Mind the Gap: Mapping Mass Spectral Databases in Genome-Scale Metabolic Networks Reveals Poorly Covered Areas. Metabolites *8*, 51.

Frédérich, M., Pirotte, B., Fillet, M., and de Tullio, P. (2016). Metabolomics as a Challenging Approach for Medicinal Chemistry and Personalized Medicine. J. Med. Chem. *59*, 8649–8666.

Gibson, D. (2009). The mechanism of action of platinum anticancer agents—what do we really know about it? Dalton Trans. *0*, 10681–10689.

Gibson, D. (2019). Multi-action Pt(IV) anticancer agents; do we understand how they work? Journal of Inorganic Biochemistry *191*, 77–84.

Gifford, J.B., Huang, W., Zeleniak, A.E., Hindoyan, A., Wu, H., Donahue, T.R., and Hill, R. (2016). Expression of GRP78, Master Regulator of the Unfolded Protein Response, Increases Chemoresistance in Pancreatic Ductal Adenocarcinoma. Mol Cancer Ther *15*, 1043–1052.

Griffiths, W.J., Koal, T., Wang, Y., Kohl, M., Enot, D.P., and Deigner, H.-P. (2010). Targeted Metabolomics for Biomarker Discovery. Angewandte Chemie International Edition *49*, 5426–5445.

Gromski, P.S., Xu, Y., Kotze, H.L., Correa, E., Ellis, D.I., Armitage, E.G., Turner, M.L., and Goodacre, R. (2014). Influence of Missing Values Substitutes on Multivariate Analysis of Metabolomics Data. Metabolites *4*, 433–452.

Gromski, P.S., Xu, Y., Hollywood, K.A., Turner, M.L., and Goodacre, R. (2015). The influence of scaling metabolomics data on model classification accuracy. Metabolomics *11*, 684–695.

Hamid, R., Rotshteyn, Y., Rabadi, L., Parikh, R., and Bullock, P. (2004). Comparison of alamar blue and MTT assays for high through-put screening. Toxicology in Vitro *18*, 703–710.

Heirendt, L., Arreckx, S., Pfau, T., Mendoza, S.N., Richelle, A., Heinken, A., Haraldsdóttir, H.S., Wachowiak, J., Keating, S.M., Vlasov, V., et al. (2019). Creation and analysis of biochemical constraint-based models using the COBRA Toolbox v.3.0. Nat Protoc *14*, 639–702.

Holtkamp, H.U. (2018). Advanced metallomics methods in anticancer metallodrug mode of action studies. Trends in Analytical Chemistry 8.

Huang, H.-L., Hsing, H.-W., Lai, T.-C., Chen, Y.-W., Lee, T.-R., Chan, H.-T., Lyu, P.-C., Wu, C.-L., Lu, Y.-C., Lin, S.-T., et al. (2010). Trypsin-induced proteome alteration during cell subculture in mammalian cells. Journal of Biomedical Science *17*, 36.

Jalili, M., Scharm, M., Wolkenhauer, O., Damaghi, M., and Salehzadeh-Yazdi, A. (2021). Exploring the Metabolic Heterogeneity of Cancers: A Benchmark Study of Context-Specific Models. Journal of Personalized Medicine *11*, 496.

Jang, C., Chen, L., and Rabinowitz, J.D. (2018). Metabolomics and Isotope Tracing. Cell *173*, 822–837.

J. Anthony, E., M. Bolitho, E., E. Bridgewater, H., L. Carter, O.W., M. Donnelly, J., Imberti, C., C. Lant, E., Lermyte, F., J. Needham, R., Palau, M., et al. (2020). Metallodrugs are unique: opportunities and challenges of discovery and development. Chemical Science *11*, 12888–12917.

Jia, D., Lu, M., Jung, K.H., Park, J.H., Yu, L., Onuchic, J.N., Kaipparettu, B.A., and Levine, H. (2019). Elucidating cancer metabolic plasticity by coupling gene regulation with metabolic pathways. PNAS 201816391.

Johnson, C.H., Ivanisevic, J., and Siuzdak, G. (2016). Metabolomics: beyond biomarkers and towards mechanisms. Nat Rev Mol Cell Biol *17*, 451–459.

Johnstone, T.C., Park, G.Y., and Lippard, S.J. (2014). Understanding and Improving Platinum Anticancer Drugs – Phenanthriplatin. Anticancer Res *34*, 471–476.

Jouhten, P. (2012). METABOLIC MODELLING IN THE DEVELOPMENT OF CELL FACTORIES BY SYNTHETIC BIOLOGY. Computational and Structural Biotechnology Journal *3*, e201210009.

Kang, M., Ragan, B.G., and Park, J.-H. (2008). Issues in Outcomes Research: An Overview of Randomization Techniques for Clinical Trials. Journal of Athletic Training *43*, 215–221.

Karaca, Ö., Scalcon, V., Meier-Menches, S.M., Bonsignore, R., Brouwer, J.M.J.L., Tonolo, F., Folda, A., Rigobello, M.P., Kühn, F.E., and Casini, A. (2017). Characterization of Hydrophilic Gold(I) N-Heterocyclic Carbene (NHC) Complexes as Potent TrxR Inhibitors Using Biochemical and Mass Spectrometric Approaches. Inorg. Chem. *56*, 14237–14250.

Karnovsky, A., Weymouth, T., Hull, T., Tarcea, V.G., Scardoni, G., Laudanna, C., Sartor, M.A., Stringer, K.A., Jagadish, H.V., Burant, C., et al. (2012). Metscape 2 bioinformatics tool for the analysis and visualization of metabolomics and gene expression data. Bioinformatics *28*, 373–380.

Katt, M.E., Placone, A.L., Wong, A.D., Xu, Z.S., and Searson, P.C. (2016). In Vitro Tumor Models: Advantages, Disadvantages, Variables, and Selecting the Right Platform. Front Bioeng Biotechnol *4*, 12.

Kelland, L. (2007). The resurgence of platinum-based cancer chemotherapy. Nat. Rev. Cancer *7*, 573–584.

Khairul, I., Wang, Q.Q., Jiang, Y.H., Wang, C., and Naranmandura, H. (2017). Metabolism, toxicity and anticancer activities of arsenic compounds. Oncotarget *8*, 23905–23926.

Kind, T., and Fiehn, O. (2007). Seven Golden Rules for heuristic filtering of molecular formulas obtained by accurate mass spectrometry. BMC Bioinformatics *8*, 105.

Komeda, S., and Casini, A. (2012). Next-generation anticancer metallodrugs. Curr Top Med Chem *12*, 219–235.

Langhans, S.A. (2018). Three-Dimensional in Vitro Cell Culture Models in Drug Discovery and Drug Repositioning. Frontiers in Pharmacology *9*, 6.

Li, Y., Gruber, J.J., Litzenburger, U.M., Zhou, Y., Miao, Y.R., LaGory, E.L., Li, A.M., Hu, Z., Yip, M., Hart, L.S., et al. (2020). Acetate supplementation restores chromatin accessibility and promotes tumor cell differentiation under hypoxia. Cell Death & Disease *11*, 1–17.

Liebal, U.W., Phan, A.N.T., Sudhakar, M., Raman, K., and Blank, L.M. (2020). Machine Learning Applications for Mass Spectrometry-Based Metabolomics. Metabolites *10*, 243.

Liu, X., and Locasale, J.W. (2017). Metabolomics: A Primer. Trends in Biochemical Sciences *0*.

Mahieu, N.G., and Patti, G.J. (2017). Systems-Level Annotation of a Metabolomics Data Set Reduces 25 000 Features to Fewer than 1000 Unique Metabolites. Anal. Chem. *89*, 10397–10406.

Mahieu, N.G., Huang, X., Chen, Y.-J., and Patti, G.J. (2014). Credentialing Features: A Platform to Benchmark and Optimize Untargeted Metabolomic Methods. Anal. Chem. *86*, 9583–9589.

Meier, S.M., Kreutz, D., Winter, L., Klose, M.H.M., Cseh, K., Weiss, T., Bileck, A., Alte, B., Mader, J.C., Jana, S., et al. (2017). An Organoruthenium Anticancer Agent Shows Unexpected Target Selectivity For Plectin. Angewandte Chemie International Edition *56*, 8267–8271.

Meier-Menches, S.M., Gerner, C., Berger, W., Hartinger, C.G., and Keppler, B.K. (2018). Structure–activity relationships for ruthenium and osmium anticancer agents – towards clinical development. Chem. Soc. Rev. *47*, 909–928.

Mjos, K.D., and Orvig, C. (2014). Metallodrugs in Medicinal Inorganic Chemistry. Chem. Rev. *114*, 4540–4563.

Monro, S., Colón, K.L., Yin, H., Roque, J., Konda, P., Gujar, S., Thummel, R.P., Lilge, L., Cameron, C.G., and McFarland, S.A. (2019). Transition Metal Complexes and Photodynamic Therapy from a Tumor-Centered Approach: Challenges, Opportunities, and Highlights from the Development of TLD1433. Chem. Rev. *119*, 797–828.

Nakayama, G.R., Caton, M.C., Nova, M.P., and Parandoosh, Z. (1997). Assessment of the Alamar Blue assay for cellular growth and viability in vitro. Journal of Immunological Methods *204*, 205–208.

Nilsson, A., and Nielsen, J. (2017). Genome scale metabolic modeling of cancer. Metab Eng *43*, 103–112.

Nyamundanda, G., Gormley, I.C., Fan, Y., Gallagher, W.M., and Brennan, L. (2013). MetSizeR: selecting the optimal sample size for metabolomic studies using an analysis based approach. BMC Bioinformatics *14*, 338.

Orth, J.D., Thiele, I., and Palsson, B.Ø. (2010). What is flux balance analysis? Nat Biotechnol *28*, 245–248.

Ortmayr, K., Causon, T.J., Hann, S., and Koellensperger, G. (2016). Increasing selectivity and coverage in LC-MS based metabolome analysis. TrAC Trends in Analytical Chemistry *82*, 358–366.

Pötsch, I., Baier, D., Keppler, B.K., and Berger, W. (2019). CHAPTER 12:Challenges and Chances in the Preclinical to Clinical Translation of Anticancer Metallodrugs. In Metal-Based Anticancer Agents, pp. 308–347.

Puchades-Carrasco, L., and Pineda-Lucena, A. (2017). Metabolomics Applications in Precision Medicine: An Oncological Perspective. Curr Top Med Chem *17*, 2740–2751.

Rampler, E., Abiead, Y.E., Schoeny, H., Rusz, M., Hildebrand, F., Fitz, V., and Koellensperger, G. (2021). Recurrent Topics in Mass Spectrometry-Based Metabolomics and Lipidomics—Standardization, Coverage, and Throughput. Anal. Chem. *93*, 519–545.

Roberts, L.D., Souza, A.L., Gerszten, R.E., and Clish, C.B. (2012). Targeted Metabolomics. Current Protocols in Molecular Biology *98*, 30.2.1-30.2.24.

Rosato, A., Tenori, L., Cascante, M., De Atauri Carulla, P.R., Martins dos Santos, V.A.P., and Saccenti, E. (2018). From correlation to causation: analysis of metabolomics data using systems biology approaches. Metabolomics *14*, 37.

Salek, R.M., Steinbeck, C., Viant, M.R., Goodacre, R., and Dunn, W.B. (2013). The role of reporting standards for metabolite annotation and identification in metabolomic studies. Gigascience *2*, 13.

Schwaiger, M., Schoeny, H., Abiead, Y.E., Hermann, G., Rampler, E., and Koellensperger, G. (2018). Merging metabolomics and lipidomics into one analytical run. Analyst *144*, 220–229.

Stock, K., Estrada, M.F., Vidic, S., Gjerde, K., Rudisch, A., Santo, V.E., Barbier, M., Blom, S., Arundkar, S.C., Selvam, I., et al. (2016). Capturing tumor complexity in vitro: Comparative analysis of 2D and 3D tumor models for drug discovery. Sci Rep *6*.

Tafani, M., Sansone, L., Limana, F., Arcangeli, T., De Santis, E., Polese, M., Fini, M., and Russo, M.A. (2016). The Interplay of Reactive Oxygen Species, Hypoxia, Inflammation, and Sirtuins in Cancer Initiation and Progression. Oxid Med Cell Longev *2016*, 3907147.

Terenzi, A., Pirker, C., Keppler, B.K., and Berger, W. (2016). Anticancer metal drugs and immunogenic cell death. Journal of Inorganic Biochemistry *165*, 71–79.

Tromp, R.A., van Boom, S.S.G.E., Marco Timmers, C., van Zutphen, S., van der Marel, G.A., Overkleeft, H.S., van Boom, J.H., and Reedijk, J. (2004). The β-glucuronyl-based prodrug strategy allows for its application on β-glucuronyl-platinum conjugates. Bioorganic & Medicinal Chemistry Letters *14*, 4273–4276.

Viant, M.R., Kurland, I.J., Jones, M.R., and Dunn, W.B. (2017). How close are we to complete annotation of metabolomes? Current Opinion in Chemical Biology *36*, 64–69.

Vojtek, M., Marques, M.P.M., Ferreira, I.M.P.L.V.O., Mota-Filipe, H., and Diniz, C. (2019). Anticancer activity of palladium-based complexes against triple-negative breast cancer. Drug Discovery Today *24*, 1044–1058.

Wagner, A., and Fell, D.A. (2001). The small world inside large metabolic networks. Proceedings of the Royal Society of London. Series B: Biological Sciences *268*, 1803–1810.

Wang, X.-X., Yu, P., and Li, J. (2020). High-Throughput Metabolomics for Identification of Metabolic Pathways and Deciphering the Effect Mechanism of Dioscin on Rectal Cancer From Cell Metabolic Profiles Coupled With Chemometrics Analysis. Frontiers in Pharmacology *11*, 68.

Wu, Y., and Li, L. (2014). Dansylation Metabolite Assay: A Simple and Rapid Method for Sample Amount Normalization in Metabolomics. Anal. Chem. *86*, 9428–9433.

Wu, Y., and Li, L. (2016). Sample normalization methods in quantitative metabolomics. Journal of Chromatography A *1430*, 80–95.

Xu, Y.-F., Lu, W., and Rabinowitz, J.D. (2015). Avoiding Misannotation of In-Source Fragmentation Products as Cellular Metabolites in Liquid Chromatography–Mass Spectrometry-Based Metabolomics. Anal. Chem. *87*, 2273–2281.

Yanes, O., Tautenhahn, R., Patti, G.J., and Siuzdak, G. (2011). Expanding Coverage of the Metabolome for Global Metabolite Profiling. Anal. Chem. *83*, 2152–2161.

Yin, P., Peter, A., Franken, H., Zhao, X., Neukamm, S.S., Rosenbaum, L., Lucio, M., Zell, A., Häring, H.-U., Xu, G., et al. (2013). Preanalytical aspects and sample quality assessment in metabolomics studies of human blood. Clin Chem *59*, 833–845.

Yoshida, G.J. (2020). Applications of patient-derived tumor xenograft models and tumor organoids. Journal of Hematology & Oncology *13*, 4.

Zhao, H., Heimberger, A.B., Lu, Z., Wu, X., Hodges, T.R., Song, R., and Shen, J. (2016). Metabolomics profiling in plasma samples from glioma patients correlates with tumor phenotypes. Oncotarget *7*, 20486–20495.

(2019). Metabolomics: Practical Guide to Design and Analysis (Boca Raton: Chapman and Hall/CRC).

Chong, J., Wishart, D.S., and Xia, J. (2019). Using MetaboAnalyst 4.0 for Comprehensive and Integrative Metabolomics Data Analysis. Current Protocols in Bioinformatics 68, e86.

Shannon, P., Markiel, A., Ozier, O., Baliga, N.S., Wang, J.T., Ramage, D., Amin, N., Schwikowski, B., and Ideker, T. (2003). Cytoscape: A Software Environment for Integrated Models of Biomolecular Interaction Networks. Genome Res 13, 2498–2504.

Synopsis of the Publications

The Ph.D. thesis consists of the three publications below. All these three works revolved around the application of metabolomics on *in vitro* cell culture models, in the context of response profiling and metallodrug research.

Single Spheroid Metabolomics: Optimizing Sample Preparation of Three-Dimensional Multicellular Tumor Spheroids

Rusz, M., Rampler, E., Keppler, B.K., Jakupec, M.A., and Koellensperger, G. (2019). Metabolites 9, 304.

https://doi.org/10.3390/metabo9120304

Published: 14 December 2019

Contribution: Design and conduction of experiments. Organization of required materials. Cultivation of cells, cell biological characterization. Development of LC-MS-method. Optimization of sample preparation. LC-MS measurements. Data analysis. Interpretation of results. Creation of figures. Writing of the manuscript.

Morpho-metabotyping the oxidative stress response

Rusz, M., Del Favero, G., El Abiead, Y., Gerner, C., Keppler, B.K., Jakupec, M.A., and Koellensperger, G. (2021). Sci Rep 11, 15471.

https://doi.org/10.1038/s41598-021-94585-8

Published: 29 July 2021

Contribution: Design and conduction of experiments. Organization of required materials. Cultivation of cells. Development of LC-MS-method and optimization of sample preparation. LC-MS sample preparation, measurements. Data analysis. Analysis of imaging data: morphological parameters and mitochondrial network. Interpretation, contextualization of results. Creation of figures. Writing of the manuscript.

Thermodynamic Genome-Scale Metabolic Modeling of Metallodrug Resistance in Colorectal Cancer

Herrmann, H.A.[†], Rusz, M.[†], Baier, D., Jakupec, M.A., Keppler, B.K., Berger, W., Koellensperger, G., and Zanghellini, J. (2021) Cancers 13, 4130.

https://doi.org/10.3390/cancers13164130

[†] Equal contributor.

Published: 17 August 2021

Contribution: Design and conduction of experiments. Organization of required materials. LC-MS sample preparation, measurements. Data analysis. Interpretation, contextualization of results. Involved in the creation of figures. Writing of the manuscript.

Results and Discussion

metabolites

MDPI

Article

Single Spheroid Metabolomics: Optimizing Sample Preparation of Three-Dimensional Multicellular Tumor Spheroids

Mate Rusz [1], Evelyn Rampler [2,3,4], Bernhard K. Keppler [1], Michael A. Jakupec [1] and Gunda Koellensperger [2,3,4,*]

1 Institute of Inorganic Chemistry, University of Vienna, Währinger Str. 42, 1090 Vienna, Austria; mate.rusz@univie.ac.at (M.R.); bernhard.keppler@univie.ac.at (B.K.K.); michael.jakupec@univie.ac.at (M.A.J.)
2 Institute of Analytical Chemistry, University of Vienna, Währinger Str. 38, 1090 Vienna, Austria; evelyn.rampler@univie.ac.at
3 Vienna Metabolomics Center (VIME), University of Vienna, Althanstraße 14, 1090 Vienna, Austria
4 Research Network Chemistry Meets Microbiology, Althanstraße 14, 1090 Vienna, Austria
* Correspondence: gunda.koellensperger@univie.ac.at; Tel.: +43-1-4277-52303

Received: 9 November 2019; Accepted: 12 December 2019; Published: 14 December 2019

Abstract: Tumor spheroids are important model systems due to the capability of capturing in vivo tumor complexity. In this work, the experimental design of metabolomics workflows using three-dimensional multicellular tumor spheroid (3D MTS) models is addressed. Non-scaffold based cultures of the HCT116 colon carcinoma cell line delivered highly reproducible MTSs with regard to size and other key parameters (such as protein content and fraction of viable cells) as a prerequisite. Carefully optimizing the multiple steps of sample preparation, the developed procedure enabled us to probe the metabolome of single MTSs (diameter range 790 ± 22 µm) in a highly repeatable manner at a considerable throughput. The final protocol consisted of rapid washing of the spheroids on the cultivation plate, followed by cold methanol extraction. ^{13}C enriched internal standards, added upon extraction, were key to obtaining the excellent analytical figures of merit. Targeted metabolomics provided absolute concentrations with average biological repeatabilities of <20% probing MTSs individually. In a proof of principle study, MTSs were exposed to two metal-based anticancer drugs, oxaliplatin and the investigational anticancer drug KP1339 (sodium *trans*-[tetrachloridobis(1*H*-indazole)ruthenate(III)]), which exhibit distinctly different modes of action. This difference could be recapitulated in individual metabolic shifts observed from replicate single MTSs. Therefore, biological variation among single spheroids can be assessed using the presented analytical strategy, applicable for in-depth anticancer drug metabolite profiling.

Keywords: multicellular tumor spheroids; metabolomics; metallodrugs; oxaliplatin; KP1339; method development; LC-MS; IT-139

1. Introduction

Three-dimensional multicellular tumor spheroids (3D MTSs) emerged as essential tools in cancer research with the aim of increasing the efficiency of oncologic drug development. Indeed, MTSs provide a cancer model of intermediate complexity, not replacing animal models entirely, but constituting a substantial improvement compared to two-dimensional (2D) monolayer cell cultures [1,2]. 3D MTSs grown from established cancer cell lines resemble more closely early-stage avascular tumors than 2D monolayer cell cultures in many aspects. For example, nutrient and oxygen concentration gradients as present in tumors are established in 3D MTS models, which in turn results in a concentration of

proliferating cancer cells in the outer layers of the MTS, while in the inner zone, deprived of nutrients and oxygen, necrotic cells accumulate (depending on the MTS size). In addition, viable quiescent cells are found in a transition zone between the necrotic core and outer layer of proliferating cells [3]. This inhomogeneity is an important feature of in vivo tumors, which 2D monolayer cell cultures fail to recapitulate as they predominantly contain normoxic, actively proliferating cells [2,4]. Many anticancer drugs exert their cytotoxicity against proliferating cells, with quiescent cells evading the treatment [5]. Thus, a model system such as 3D MTSs, which involve quiescent cells, is of utmost importance.

Another key aspect is the fact that the three-dimensionality intrinsically affects the cell morphology (rather round instead of stretched-out on a plastic surface), which relates to cell-to-cell contacts, stimuli exerted by cell surface receptors, and, ultimately, transcription and protein expression levels [6]. Furthermore, reduced oxygen levels and hypoxia lead to the generation of reactive oxygen species (ROS) and hypoxia-inducible factor-1 (HIF-1) stabilization, which is a major transcription factor responsible for metabolic transformation and tumor progression [7–10].

In the recent past, the combination of cancer models with cutting edge –omics type of analysis showed to be a powerful approach for generating new hypotheses regarding the prediction of drug susceptibility, drug resistance, and mode of action [11,12]. This was accompanied by a reemerging interest in cancer metabolism [13]. Metabolic signatures are accepted as the closest proxy for a phenotype [14,15]. One of the biggest hopes in cancer metabolomics is the discovery of molecular signatures with predictive power in cancer therapy [16]. As a consequence of this renewed interest in metabolism, dedicated workflows were introduced, addressing the needs of preclinical and clinical studies [17–19]. Cancer cell model studies required the development and validation of multi-step sample preparation protocols [20]. While today metabolomics experiments with 2D monolayer cell cultures are routine, sample preparation protocols for 3D MTSs are rarely discussed in detail. Up to date, only a few reports on metabolomics in 3D MTS models exist. The studies involved a range of LC-MS-based metabolomics workflows including lipidomics and fluxomics applications [21–25]. Despite showing the power of combining advanced models such as 3D MTSs and metabolomics, the validation of sample preparation was not addressed comprehensively. Even a detailed description of the experimental design (e.g., whether MTS samples were pooled for the analysis or how gels established in 3D culture were removed upon metabolome extraction) was lacking.

In this work, we focus on the experimental design enabling metabolomics in 3D MTSs, using non-scaffold based cell cultures grown on ultra-low attachment plates from cell suspensions. This approach avoids 3D scaffolds or gels for obtaining a three-dimensional structure, which facilitates metabolomics measurements. More specifically, sample preparation protocols are developed with the goal to provide a validated procedure capable of probing single MTSs; at the same time not compromising on analytical throughput and, thus, the number of biological replicates. The validity of the established preclinical tool-set was shown for the example of metal-based anticancer drug development. Metal-based drugs are a prime example since a clear cut mechanism remains to be elucidated despite extensive clinical use and fundamental research [26,27]. In fact, how the drugs exert their cytotoxicity differs even for the three clinically approved platinum(II) drugs [28–30]. Although massive research efforts resulted in a plethora of promising candidate drugs, the failure rate upon translation into clinics was/is extremely high for metal-based anticancer drugs [31]. Discovering potential metabolic pertubations specific for drug exposure, by measuring molecular signatures in advanced 3D MTS models, bear the potential of accelerating discoveries with regard to the mode of action and susceptibility towards the drug. In this work, a 3D human colon cancer model was studied. Metabolic shifts, as exerted by the clinically established oxaliplatin and KP1339, a promising candidate drug, were investigated.

2. Results

2.1. Establishment and Validation of Sample Preparation Procedures Suitable for Probing the Metabolome of Spheroids

2.1.1. Determining the Minimal Number of MTS Required for Metabolomics Experiment

A uniform size distribution of MTSs was obtained by using the colon cancer model HCT116; seeding of 3×10^3 cells and cultivation for 4 days following the suspension-based procedure described in the experimental section. The average resulting spheroid diameter was 560 ± 30 µm (n = 56). Suspension-based 3D cultivation enabled a straightforward establishment of metabolomics workflows otherwise hampered by tedious washing procedures in hydrogel and other scaffold-based techniques. The investigated size range amounted to $9.9 \times 10^3 \pm 3.9 \times 10^3$ cells with 81% ± 5% viable cells (Table S1, "cellNumbers" sheet). The estimation was based on disaggregating the MTS with a recombinant enzyme reagent, staining with a dye, and subsequent measurement with a flow cytometer to determine cell counts and viability in the final suspension.

In order to exclude poor extraction efficiencies for MTSs in this work, metabolomics experiments resorted to boiling ethanol extractions, implementing the yeast-derived fully ^{13}C labeled ($U^{13}C$) internal standard. More specifically, extractions were carried out on single spheroids (three biological replicates, N = 3) and pooled spheroid samples, i.e., pools of 5 (N = 3), 10 (N = 3) and 15 spheroids (N = 2), respectively. The applied boiling ethanol protocol is the established gold standard in yeast metabolomics, offering nearly 100% extraction efficiency and recovery for a large panel of primary metabolites [32,33]. In cancer cell monolayer cultures, less tedious cold extraction protocols are established, which demand thorough validation when applied to MTS investigations [20,34].

Targeted metabolomics measurements were performed implementing reversed-phase chromatography coupled to tandem mass spectrometry using a 100%-wettable column providing enhanced separation for branched amino acids and organic acids [35]. Metabolite abundances relative to the isotopically enriched internal standard, i.e., relative response ratios, were addressed in single MTS extractions versus pooled extractions. The validation considered 29 metabolites (amino acids, organic acids, nucleotides, nucleosides). Single spheroid extractions resulted on average in repeatabilities of 28%, while pooled samples showed repeatabilites of 17% and 32% for 5 and 10 MTSs pooled, respectively (Table S1, "metabolitesExtract" sheet). In order to evaluate whether the number of pooled MTSs correlated with cell number and protein content, the cell pellets remaining upon boiling ethanol were submitted to acidic hydrolysis. Absolute amounts of 8 amino acids (alanine, arginine, glycine, histidine, lysine, phenylalanine, proline, tyrosine) were determined. The selected amino acids were quantitatively recovered [36] by the applied sample preparation protocol and were used for traceable protein quantification. The obtained absolute amino acid amounts displayed a strong linear correlation with the number of MTSs (Table S1, "aminoAcids_pellet", and Figure A3). This linear correlation (coefficient of determination above 0.99) was a prerequisite for further evaluation of metabolome abundances in single versus pooled MTS samples, depending on the assumption of linear correlation between cell number, protein concentration, and the number of spheroids (for a uniformly sized MTS sample set). Upon transforming the linear regressions of metabolite abundances from intracellular cell extracts versus number of spheroids by normalizing the metabolite abundances to average abundance found in single MTS samples, the parameters of the linear regression became comparable: assuming an ideal scenario (as represented by 100% extraction efficiency and recovery regardless of whether pooled or single samples are investigated) for these plots, a slope of 1 is expected and can be observed for the investigated metabolites, the ideal case of slope of 1 is nearly met (Table S1, "regressionNormalized", Figures A2 and A3). On average, the slope of the normalized regression is 1.11 and the average coefficient of determination is 0.94. Overall, the strong linear correlation of the relative responses with the number of uniform-size spheroids indicates that metabolomics experiments, even from single spheroids, are highly repeatable.

These findings are captured in a correlation matrix (Figure 1), which reveals that most of the investigated metabolites have a strong positive correlation with the amino acids measured from the corresponding pellet as well as from the number of MTSs they were extracted from.

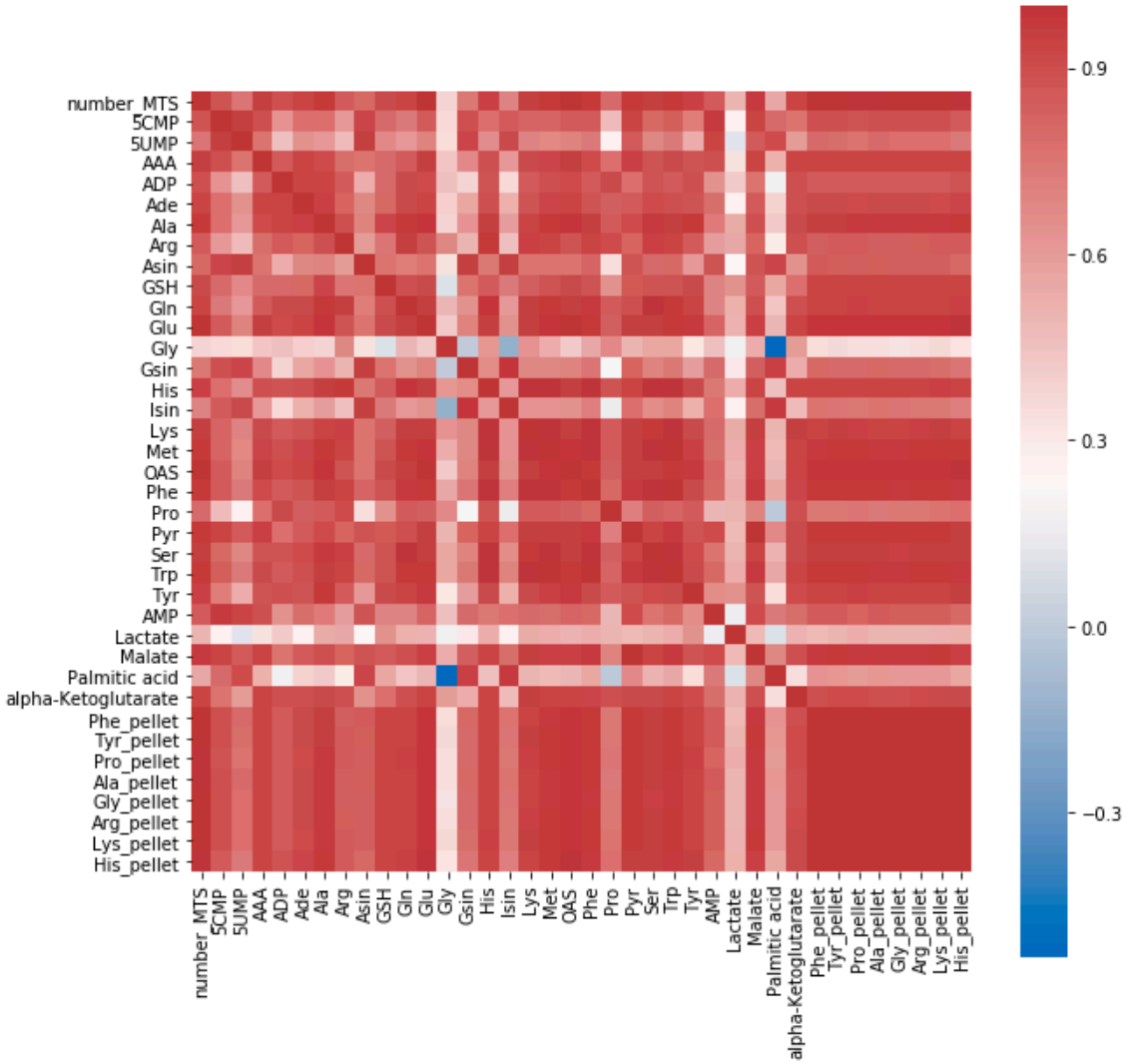

Figure 1. Correlation matrix of number of multicellular tumor spheroids (MTS), relative responses ($^{12}C/^{13}C$) of 29 metabolites from boiling ethanolic extracts with ^{13}C internal standardization, absolute amounts of 8 amino acids [nmol] measured from hydrolyzed pellet (indicated with the "pellet" suffix) from samples containing 1 ($N = 3$), 5 ($N = 3$), 10 ($N = 3$), and 15 MTS ($N = 2$) from the same population. Most metabolites show a strong correlation with all the amino acids hydrolyzed from the pellet and the number of MTSs.

2.1.2. Speeding Up the Sample Preparation

In the next step, alternative extraction protocols were addressed with the aim of increasing analytical throughput without compromising overall accuracy. The workflow based on boiling ethanol, involved the transfer of MTSs into tubes, three washing steps, and quenching by flash freezing with liquid nitrogen, which was followed by hot extraction. As a drawback, the procedure is rather time-consuming and on top of that, only a very limited number of MTS samples can be prepared in parallel. In fact, during collection and washing, only a limited number of spheroids can be handled at a given time. Only after the handled samples are quenched can be the next MTS collected. This often implies different durations of incubation at uncontrolled temperatures and CO_2 partial pressure, which might lead to systematic metabolic biases. Thus, it is key to decrease the time until quenching,

as only a high degree of synchronization enables reasonable study sizes (number of replicates) and investigations of cells upon multiple metabolic perturbations [20].

In this work, the reduction of cell manipulations was addressed as follows: First, comparative metabolomics experiments compared different strategies regarding the first washing steps. Instead of transferring MTSs to tubes for repeated washing, single-step washing was performed on the cultivation plate directly. (For the sake of clarity the first approach was denoted as "OFF", while the single washing step on the well-plate was denoted as "ON".) Second, the extraction procedure was optimized. More specifically, the hot extraction (boiling ethanol, "BE") was compared to a cold methanol-based extraction ("CM"). In the past, it was shown that the harsh conditions of hot ethanol were not a stringent requirement for monolayer mammalian cell cultures [34], where mild cold extractions proved to be valid strategies.

The already-mentioned studies [18–22] with 3D cultures involving LC-MS-based metabolomics workflows, including lipidomics and fluxomics applications utilized washing of the samples and organic solvents (methanol, acetonitrile) with an aqueous proportion for extraction, mostly in cold state. To the best of our knowledge, a thorough evaluation of 3D cancer cell models is still lacking.

Figure 2 depicts the two sample preparation strategies involving washing, quenching, internal standardization using ^{13}C internal standards and extraction. The validation experiments were carried out using replicates of single spheroids. The cultivation was designed to produce large spheroids (diameter = 744 ± 15 µm, 4-day long cultivation, and 10^4 cells seeded) representing a "worst-case scenario" for efficient extraction. Four different sample preparation strategies were compared, namely OFF and ON plate washing, both followed by either BE or CM, respectively, all involving $U^{13}C$ internal standardization upon extraction. The extracts were measured as described in [37]. In brief, a hydrophilic interaction liquid chromatography (HILIC) separation at pH 4 was used combined with high-resolution MS. Targeted absolute quantification of 26 metabolites based on external calibration with internal standardization served as validation of the sample preparation.

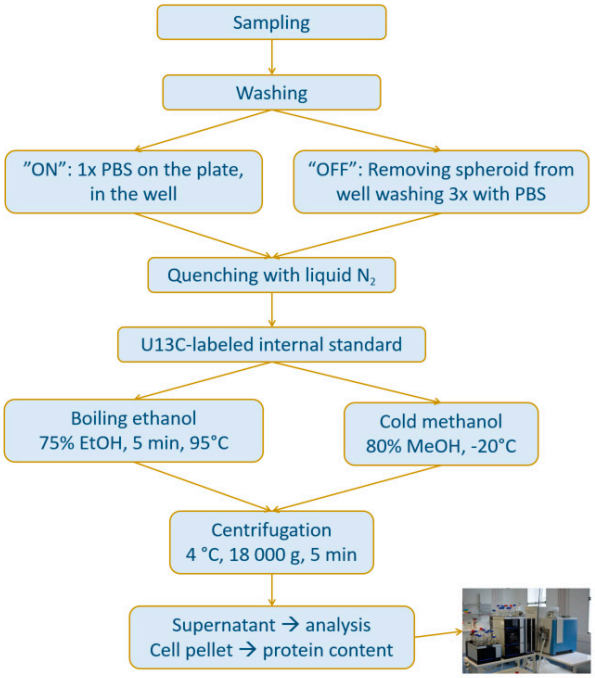

Figure 2. The study design for speeding up the sample preparation. Two different washing procedures ("ON": washing the multicellular tumor spheroid once with PBS on the 96-well plate vs. "OFF" washing three-times in an Eppendorf-tube after transfer from cultivation well) and two alternative extractions (boiling ethanol vs. cold methanol extraction) were tested on large multicellular tumor spheroids (744 ± 15 µm), which in combination resulted in four sample groups.

In addition to the biological repeatability, the technical repeatability was assessed by injections of a pooled sample over the measurement series (denoted as QC). Figure 3 summarizes the quantitative metabolome data. Overall, it was found that the accelerated workflow with the reduced washing steps was key to improve repeatability, as this resulted in the lowest average relative standard deviations (18% and 19% for ON/BE and ON/CM, respectively. See Table 1.). Moreover, it could be shown that the cold methanol (CM) extraction was comparable to boiling ethanol (BE) in terms of extraction efficiency, as the quantitative values were in good agreement (within their uncertainty).

Table 1. Average relative standard deviations based on absolute concentrations of 26 analytes in four investigated sample preparation strategies for single multicellular tumor spheroids. The four different sample preparation methods involved two washing procedures ("ON": washing the multicellular tumor spheroid once with PBS on the 96-well plate vs. "OFF" washing three times in an Eppendorf tube after transfer from cultivation well) and two alternative extractions are combined (boiling ethanol "BE" vs. cold methanol extraction "CM"). OFF/BE (N = 6), ON/BE (N = 4), OFF/CM (N = 5), ON/CM (N = 7) One pooled sample from independent OFF/CM and ON/CM samples, QC was a mixture of one OFF/CM and ON/CM sample and was measured as quality control throughout the measurement (N = 4). Measurement was performed with liquid chromatography (HILIC separation) high-resolution Orbitrap mass spectrometry. All extractions utilized $U^{13}C$ internal standardization.

Sample Preparation	Average RSD [%]
OFF/BE	34%
ON/BE	19%
OFF/CM	24%
ON/CM	18%
QC	7%

Thus it can be concluded that the protocol ON/CM offers a fast and convenient fit-for-purpose method to generate 60 biological replicates in parallel. The 60 replicates were treated and washed within a few minutes (depending on the operator) and then were quenched at the same time by flash freezing them with liquid nitrogen. Overall, a 96-well plate accommodates up to 60 spheroid cultivations since wells at the edges are not used to avoid the "edge effect" (artifacts due to inhomogeneity in evaporation rates).

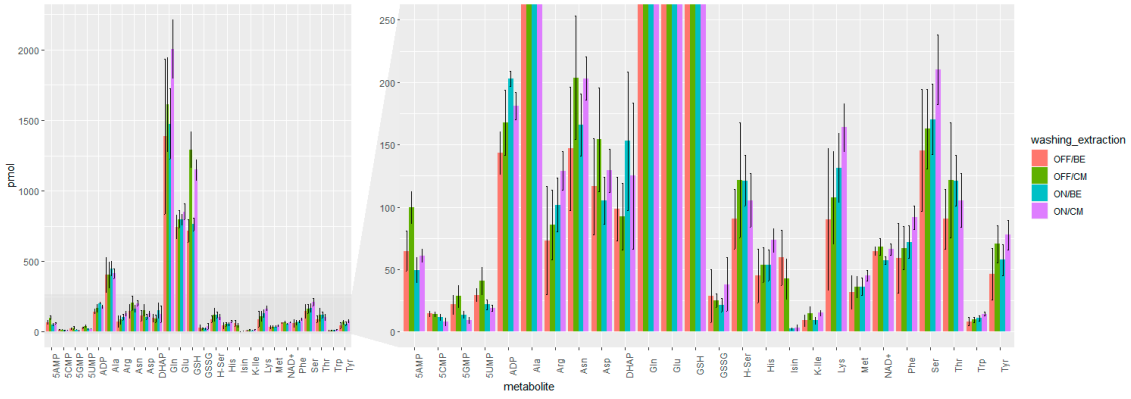

Figure 3. Barplots of the absolute amounts (pmol) of 26 selected metabolites extracted from single multicellular tumor spheroids with four different sample preparation method as well as two washing procedures ("ON": washing the multicellular tumor spheroid once with PBS on the 96-well plate vs. "OFF" washing three times in an Eppendorf-tube after transfer from the culture plate) and two alternative extractions (boiling ethanol, "BE" vs. cold methanol extraction "CM"). OFF/BE (N = 6), ON/BE (N = 4), OFF/CM (N = 5), ON/CM (N = 7) Measurement with liquid chromatography (HILIC separation) high-resolution Orbitrap mass spectrometry. All extractions utilized $U^{13}C$ internal standardization. For the abbreviations of compounds, see Appendix A.

2.2. Assessing Metabolic Shifts in Single MTS Exposed to Metal-Based Anticancer Drugs

Finally, the optimized ON/CM workflow was applied in a proof of principle study addressing metabolic perturbations in single MTSs due to exposure of metal-based anticancer drugs. Again human colon cancer cells (HCT116) were selected. The spheroids were grown from 10^4 cells for 8 days (790 ± 22 µm). Two drugs of distinctly different proposed modes of action were investigated, namely the clinically established oxaliplatin and the investigational anticancer drug sodium *trans*-[tetrachloridobis(1H-indazole)ruthenate(III)] (denoted as KP1339). While oxaliplatin exerts its cytotoxic effects through DNA damage and ribosome biogenesis stress [38], there is growing evidence that KP1339 is not a DNA-damaging agent but its primary mode of action is through endoplasmic reticulum stress [39]. Furthermore, KP1339 shows a prodrug nature, as it is thought to be preferentially reduced in the more reductive milieu of solid tumors to the active Ru(II) form. Finally, while oxaliplatin is considered a bona fide immunogenic cell death inducer [40], KP1339 also exhibits the hallmarks of immunogenic cell death [41,42].

The choice of incubation time and drug concentration was based on previous studies using monolayer cultures, which showed prominent metabolomic shifts only after 24 h exposure to sub-cytotoxic drug concentrations [37]. Specifically, the applied concentrations were 20 and 200 µM for oxaliplatin and KP1339, respectively. As the dissolution and thus the application of KP1339 involved dimethyl sulfoxide (DMSO), an additional control group resembling the DMSO background in the medium was included. Figure A4 and Table S3 (protein_µg sheet) show the protein concentrations obtained in replicate single MTSs for the different conditions under investigation. The plotted protein content was assessed by measuring the concentration in the remaining cell pellets of the individual MTS samples. As can be readily observed, oxaliplatin treatment resulted in a minor reduction of the overall protein content; otherwise the average mean protein concentration was comparable (within its uncertainty) for all conditions, pointing towards comparable growth rates. On top of that, the data clearly showed that using the average protein content of parallel MTS cultivations would compromise the quality of comparative metabolomics experiments. When aiming at the investigation at single MTS level, it is a requirement to normalize metabolic abundances to the corresponding protein content obtained from the same sample. Finally, the ON/CM sample preparation procedure optimized for single MTS analysis comprised the addition of yeast ^{13}C standards. The measurements relied on hydrophilic interaction chromatography—Orbitrap MS and included external calibrants with internal standards for a large panel of metabolites [37]. Implementing the internal standardization approach together with the use of high-resolution Orbitrap MS enabled us to perform targeted and non-targeted metabolomics in a single analytical run.

As suggested by the standardization initiative of the Metabolomics Society, pooled MTS extracts were used as quality control samples [43,44]. Combining positive and negative data, absolute concentration values were obtained. Only analytes with technical repeatability obtained from repeated injections of the QC sample below 30% were considered, which resulted in a total number of 58 remaining analytes. The average relative standard deviation (RSD) for the 58 metabolites was 6.5% for the technical replicates and 13% for biological replicates considering each four group (Table S3, pmolMetabolite sheet). The average RSD after the protein content normalization was 15.2% (Table S3, pmolMetabolitePerµgProtein sheet).

Unsupervised statistical analysis of the targeted, protein content normalized data revealed that there is group clustering according to the type of drug treatment in the case of KP1339 treatment (PCA plot in Figure A5 and heat map in Figure 4). The KP1339-treated samples showed significant regulation of 19 metabolites (proline, propionyl-L-carnitine, ribulose-5-phosphate/ribose-5-phosphate, adenosine monophosphate, lactate, aspartate, reduced glutathione, guanosine monophosphate, glutamine, inosine, glutamate, N-acetylserine, adenosine, dihydroxyacetone phosphate, asparagine, mevalonic acid, alanine, and sarcosine; Table S3, ("significant_cmpds_KP1339") compared to six metabolites (adenosine, guanosine monophosphate, cytidine monophosphate, nicotinamide adenine dinucleotide phosphate (oxidized), uridine monophosphate, and uracil; from Table S3 "significant_cmpds_oxaliPt")

in oxaliplatin-treated samples. The stronger metabolic change caused by the ruthenium drug (KP1339) treatment compared to oxaliplatin treatment was further confirmed by hierarchical cluster analysis, where KP1339-treated samples were separated from both controls, which was not the case for oxaliplatin-treated samples (Figure 4). Overall, the fact that we see a stronger effect in the metabolome with KP1339 treatment than with oxaliplatin treatment is not surprising, since in a study with monolayer cell cultures of the same cell line, we observed considerably milder effects with oxaliplatin, as well [37].

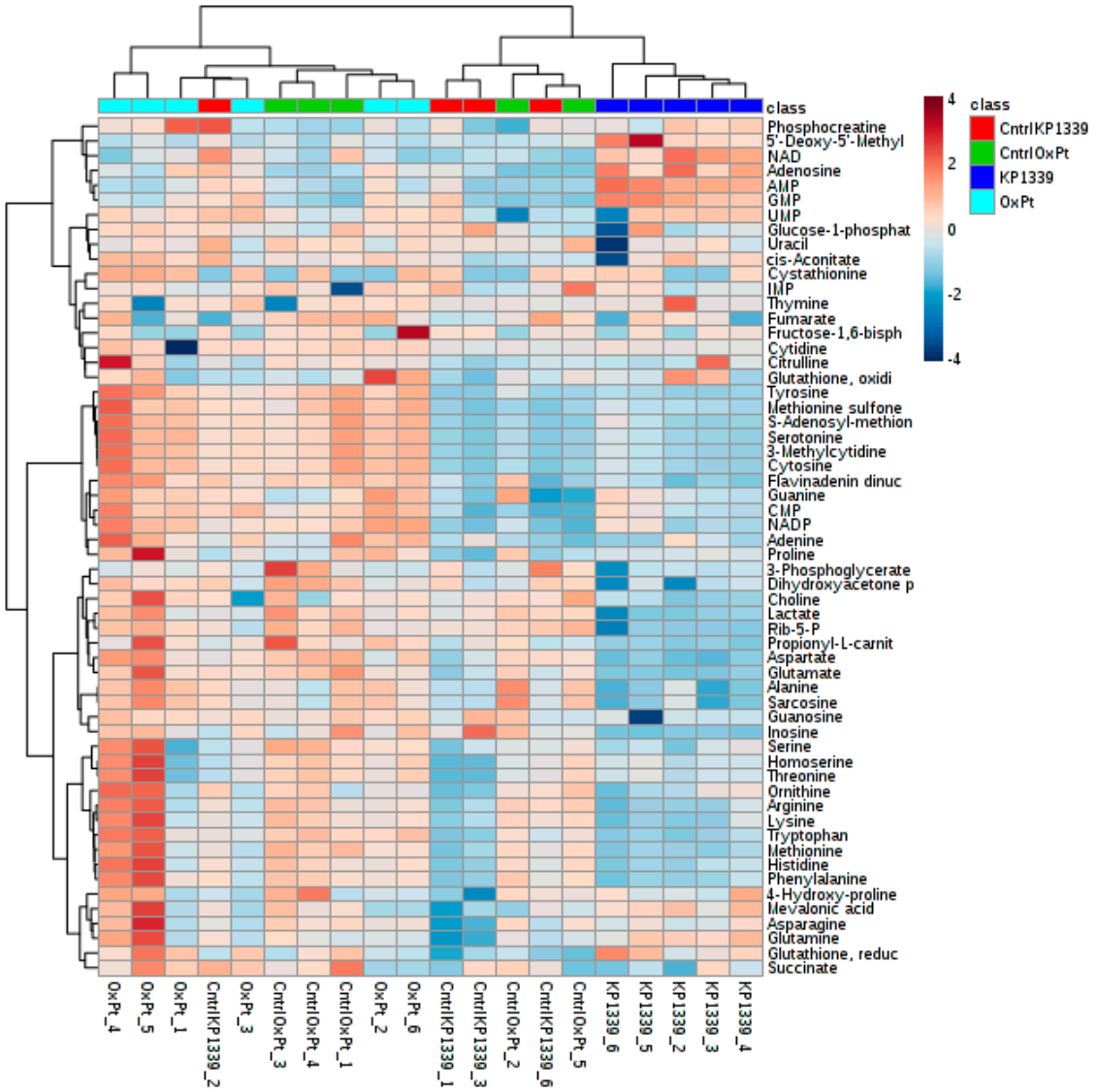

Figure 4. Heatmap displaying absolute amounts of metabolites normalized to total protein content (pmol/µg) of samples from single 3D MTS. Spheroids were treated for 24 h with either 200 µM KP1339, 20 µM oxaliplatin (OxPt), medium (CntrlOxPt) or medium with 0.5% DMSO (CntrlKP1339). Numbers in sample names refer to independent biological replicates. Extraction with cold methanol and internal standardization, measurement by HILIC high-resolution Orbitrap MS.

Pathway enrichment analysis using targeted data revealed that oxaliplatin exposure affected purine metabolism (GMP and adenosine being most significantly down-regulated; glutamine, IMP, inosine, guanosine, guanine, adenine, and AMP were also affected) and pyrimidine synthesis (UMP and CMP being most significantly down-regulated; but cytidine, uracil, glutamine and thymine were also affected), which is in agreement with the accepted mechanism of action of DNA targeting [45] (Figure 5a, Table S3, "pathways_pathways_oxaliplatin"). These findings were also supported by

other significant metabolic shifts involving DNA building blocks. Other retrieved pathways could be related to redox stress such as the pentose phosphate pathway, glutathione metabolism, and nicotinamide metabolism, but also purine metabolism, which is in accordance with the ribosome biogenesis stress only recently proposed as the primary reason for the cytotoxic effect [38]—a hypothesis generated based on transcriptomic analysis. In our work, the measurement of the metabolome provided additional evidence supporting this hypothesis, as the levels of many RNA monomers were significantly altered upon drug exposure (Table S3, "pathways_pathways_oxaliplatin"), and RNA being one of the major component of ribosomes. This was further supported by the fact that the "aminoacyl-tRNA biosynthesis" pathway was also among the affected pathways (see Table S3 for the complete list). Finally, the MetaboAnalyst 4.0 Pathway Analysis module [46] revealed another interesting pathway to be further investigated, namely, the "pantothenate and CoA biosynthesis" pathway (through uracil downregulation). A recent study [29] addressed signature genes for patients responding to oxaliplatin therapy by machine learning. Among the most accurate signature genes for oxaliplatin treatment was PANK3 which encodes for pantothenate kinase, a key regulatory enzyme in the biosynthesis of coenzyme A (CoA). A seminal study correlating transcriptomics and metabolomics for the NCI60 cell line panel showed the involvement of the TCA cycle, pyruvate metabolism, lipoprotein uptake and nucleotide synthesis in platinum sensitivity [47,48]. Again, the metabolomics data of this study support the generated hypothesis as the TCA cycle, purine and pyrimidine metabolism, and pyruvate metabolism were indicated by pathway enrichment analysis.

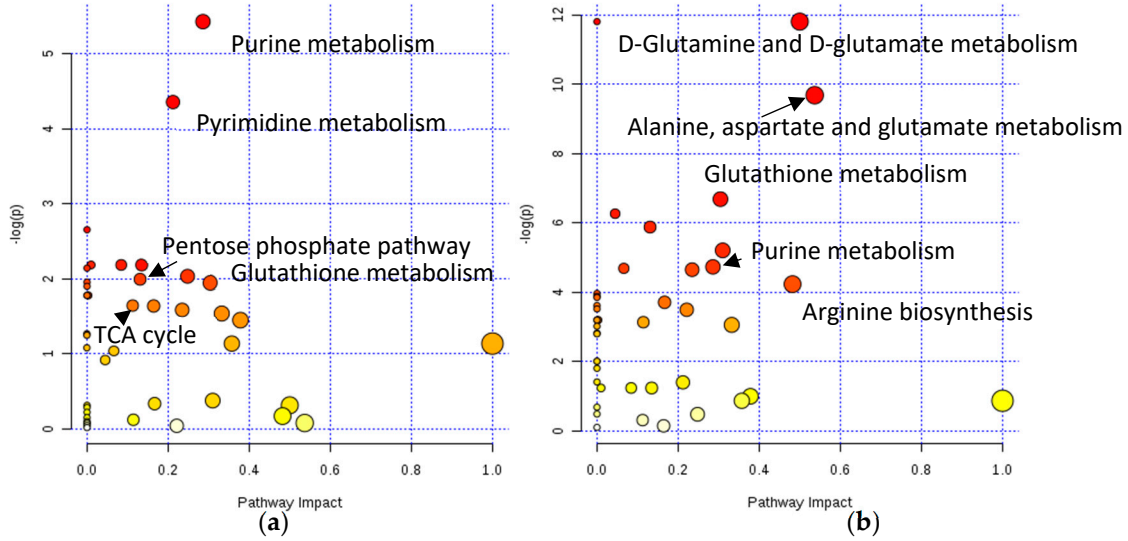

Figure 5. KEGG pathways with MetaboAnalyst affected by oxaliplatin treatment (**a**) and KP1339 treatment (**b**) using pathway enrichment and topology analysis with the MetaboAnalyst pathway analysis module.

The hypothesized difference in the mode of action of the two investigated drugs was reflected by the distinct metabolic shifts, which were observed upon exposing MTSs to the candidate ruthenium drug KP1339. There are indications that this drug is a GRP78 inhibitor, an ER stress sensing chaperone [39,49]. It not only induces ER stress and unfolded protein response, but it has also been shown that it exhibits the hallmarks of immunogenic cell death, calreticulin exposure, and ATP secretion among others [42]. Less is known about the metabolic effects of this compound. In this work, we could individuate the impact on biochemical pathways related to redox stress: glutathione metabolism (glutathione, oxidized glutathione and NADP+ are up-, glutamate down-regulated), purine metabolism, pentose phosphate pathway (ribulose 5-phosphate/ribose 5-phosphate down-regulated), which could be explained by the hypothesized reduction of the drug. Redox stress and elevation of ROS protective proteins [42,50] were confirmed by previous proteomics studies. Finally, pathways such as glycerophospholipid

metabolism (strong choline down-regulation) and various amino acid metabolism-related pathways were pinpointed (glutamine and glutamate metabolism, alanine, aspartate and glutamate metabolism, arginine biosynthesis). Altered amino acid synthesis is related to the fact that the unfolded protein response induces changes in the expression of genes of amino acid transport and synthesis [51].

3. Discussion

In this work, we present a carefully optimized sample preparation workflow for metabolomics experiments in 3D MTS samples. To the best of our knowledge, this is the first study performing extraction optimization ($n \geq 4$) for single tumor spheroids. The comparison of different extraction strategies, namely ON/BE, OFF/BE, OFF/CM, ON/CM, revealed that cold 80% methanol extraction with a single washing step on the plate was most promising for single tumor spheroid analysis. Using the presented workflow increased throughput and convenience as well as resulted in superior analytical figures of merit including the highest analyte concentration and lowest RSDs observed for 26 metabolites in the pmol to nmol range. The sample preparation strategy is limited to spheroids with diameters >400–500 µm and with maximum diameters of 900–1000 µm due to potential error-prone handling and growth limitation, respectively. Other studies in tumor spheroid analysis were performed using various culturing and extraction protocols such as (1) gelatinous cultivation of spheroids and methanol-water extraction [21], (2) magnetized cells to form 3D cultures and cold acetonitrile, 70% methanol or 80% acetone extraction [22], (3) gel-based ultra-low attachment plates of 20–25 spheroids per sample followed by derivatization and chloroform/methanol extraction [23]. Overall, most –omics mass spectrometry-based studies on tumor spheroid analysis rely on extraction strategies with cold organic solvents such as methanol, ethanol or isopropanol [21–24]. This is consistent with our tumor spheroid workflow based on non-scaffold based cultivation on ultra-low attachment plates and the optimized cold 80% methanol extraction with a single washing step. The obtained strong linear correlation with the number of (uniform-size) spheroids and relative responses indicates highly repeatable metabolomics readout from single spheroids. The use of ^{13}C labeled standards for quantification represents a significant advance compared to label-free quantification approaches as the internal standardization allowed to account for sample losses during sample preparation, storage and measurement. Additionally, ^{13}C metabolites represent an interesting normalization strategy for comprehensive non-targeted metabolomics experiments on tumor spheroids. The novel procedure enabled us to probe individual spheroids with excellent biological repeatability (average RSD of 18%) in a considerable throughput. An experiment with a single 96-well plate allows the investigation of up to 60 single spheroids (since wells at the edges are not used). However, high throughput analysis is feasible as there is no theoretical limit in the number of biological replicates or investigated conditions when multiple plates are combined.

The proposed methodology enabled us to investigate different conditions of 3D human cancer models in a parallelized manner comparable to the degree obtained in 2D monolayer cell cultures. The applicability of the method was shown on the example of the metal-based anticancer drugs KP1339 and oxaliplatin. Comparison of the two drugs ($n \geq 4$) revealed stronger metabolic changes caused by the ruthenium drug (KP1339) treatment compared to oxaliplatin treatment, which is consistent with the literature on monolayer cell cultures [37]. We observed significant metabolic changes with purine and pyrimidine pathways after oxaliplatin treatment, which is in agreement with the accepted mechanism of action of DNA targeting of oxaliplatin [45] and consistent with the proposed induction of ribosome biogenesis stress [38]. Further biological interpretation of the data is beyond the scope of this work.

The presented optimized sample preparation workflow is the ideal starting point for single spheroid metabolomics experiments. A relatively large proportion of clinically tested drugs fail in phase 3 of the trials due to insufficient efficacy or unacceptable toxicity, which means a substantial financial loss [6,52]. Since tumor spheroids are three-dimensional models derived from established human cell lines, it is possible to capture more of the complexity of a tumor compared to standard 2D monolayer cultures [1]. Ultimately, metabolomics studies on tumor spheroids could be integrated

into anticancer drug screening, helping to prevent late clinical failure of drug candidates. Future studies will focus on in-depth metabolomics analysis of different anticancer drugs effects using tumor spheroids. Overall, we strongly believe that drug development will benefit significantly from the new discovery tools provided by the unique combination of 3D MTSs and metabolomics.

4. Materials and Methods

4.1. Cell Culture

4.1.1. Cultivation of Spheroids

The human colon carcinoma cell line HCT116 was kindly provided by Brigitte Marian, Institute of Cancer Research, Department of Medicine I, Medical University of Vienna. HCT116 cells were cultured as adherent monolayers in 75 cm^2 flasks (StarLab Germany) in McCoy's 5a medium (Sigma-Aldrich) supplemented with 10% fetal calf serum (FCS) (BioWest) and 4 mM L-glutamine without antibiotics at 37 °C (StarLab) under a humidified atmosphere containing 5% CO_2. All cell culture media and reagents were obtained from Sigma-Aldrich (Vienna, Austria), and all plastic dishes, plates and flasks were from StarLab (Germany) unless stated otherwise. For spheroid generation, HCT116 cells were harvested from culture flasks by trypsinization, resuspended in their respective supplemented medium, and seeded in 200 µL on ultra-low attachment round-bottom 96-well plates (Nunclon Sphera™, Thermo Fisher Scientific). To avoid effects caused by evaporation, the outermost wells were not used for spheroid production and filled with 200 mL of PBS instead. In the experiment where 1, 5, 10, 15 spheroids were investigated, the spheroids were seeded at a density of 3×10^3 viable cells per well in 200 µL. Plates were incubated at 37 °C with 5% CO_2 for 96 h to allow spheroid formation. In the experiment where washing procedures and extraction methods were compared, 10×10^3 viable cells were seeded in 200 µL medium and cultivated at 37 °C with 5% CO_2 for 96 h to allow spheroid formation. In the proof of concept experiment with metallodrugs, 10×10^3 viable cells were seeded in 200 µL medium and cultivated at 37 °C with 5% CO_2 for 96 h to allow spheroid formation, and then 100 µL medium was aspirated and exchanged for fresh medium. After 192 h (8 days) of total incubation, the diameter of the spheroids was measured, 100 µL of medium was exchanged for the respective treatment solution and 24 h of incubation followed either with the drug or with control medium. KP1339 was first dissolved in DMSO, and stock solutions were prepared in the respective medium with FCS and glutamine supplement. Oxaliplatin was dissolved freshly before the experiments in the supplemented medium only.

4.1.2. Microscopy

An Olympus CKX41 (Olympus, Vienna, Austria) microscope was used to measure the diameter of the spheroids in horizontal and vertical directions with cellF 2.7 imaging software and the average diameter was calculated.

4.1.3. Cell Number Estimation

Spheroids grown from 3×10^3 viable cells for 96 h were transferred from the plate to Eppendorf-tubes as single spheroids. After washing once with PBS, dissociation in 100 µL TrypLE Express (Gibco, Vienna, Austria) followed for 15 min at 37 °C. Samples were thoroughly pipetted to disperse any remaining cell aggregates, and 100 µL colorless McCoy's 5a medium (Sigma-Aldrich) with 2% FCS were added followed by 0.8 mL Guava ViaCount reagent (Merck/Millipore, Germany). Samples were measured immediately by using a Guava Soft flow cytometer (Merck/Millipore, Darmstadt, Germany).

4.2. Methods for Determining the Minimal Number of MTS Required for a Metabolomics Experiment

4.2.1. Sampling 1, 5, 10, 15 Multicellular Tumor Spheroids

3D MTS were seeded with 3×10^3 cells in 200 µL McCoys medium and cultivated for 4 days, reaching a diameter of 560 ± 30 µm. Upon extraction, spheroids were transferred by pipetting to a Petri-dish, where little droplets of PBS had been pre-pipetted. Each spheroid was transferred sequentially into three fresh PBS droplets corresponding to three washing steps. After that, each spheroid was transferred into a conical screw cap vial (Bioquote Limited, York, United Kingdom). The vial was put into liquid nitrogen in order to quench the enzymatic activity and put on wet ice, while more spheroids were collected. As soon as the last spheroid for a given sample was washed and sampled to the vial, it was put on −20 °C. When all the samples were collected, they were stored at −80 °C until boiling ethanol extraction.

4.2.2. Internal Standardization

A fully ^{13}C labeled yeast extract of *Pichia pastoris* (2 billion cells) from ISOtopic Solutions e.U., (Vienna, Austria) was reconstituted in 2 mL of water and added in equal amounts to the samples. The final dilution of the internal standard for the measurement was 1:10.

4.2.3. Boiling Ethanol Extraction for 1×-5×-10×-15× MTSs

The protocol was implemented from the works [32,33]. Shortly, 75% ethanol was prepared from ethanol, abs. 100%, HPLC grade (Chem-Lab, Vienna, Austria), H_2O (Sigma, Vienna, Austria, LC-MS-grade), and pre-heated in a clean glass beaker in a 95 °C water bath. The 50 µL of $U^{13}C$ internal standard was added to samples. Once the ethanol–water was boiling in the glass beaker, the hot extraction solvent was added to the conical screw cap vials (Bioquote Limited, York, United Kingdom) to dilute the internal standard amount 1:10 and, subsequently, a 5-min incubation in the 95 °C water bath followed. The vials were closed, vortexed, and centrifuged (14,000 rcf, 4 °C, 5 min). The supernatant was carefully transferred to an MS-vial (Macherey-Nagel, Vienna, Austria), without disturbing the pellet. Extracts were evaporated until dryness. Extracts and resulting pellets were stored at −80 °C until measurement.

4.2.4. Metabolomics Measurement of Extracts 1×-5×-10×-15× MTSs

Samples were reconstituted in 100 µL LC-MS-grade H_2O and analyzed with reversed phase liquid chromatography coupled to high-resolution Orbitrap mass spectrometry. Waters Acquity HSS T3 (2.1 × 150 mm, 1.8 µm) column was used, mobile phase A was H_2O (0.1% formic acid), and mobile phase B was 100% methanol. The following gradient was used at a flow rate of 0.3 mL min^{-1} and 40 °C: 0.0–2.0 min 0% B, 2–6 min 0–40% B, 6–8 min 40–100% B, 8–11 min 100% B, and at 11.1 min switch to 0% B, 11.1–15 min 0% B. The injection volume was 10 µL. The Vanquish Duo UHPLC-system (Thermo Fisher Scientific) was used.

High-resolution mass spectrometry was done with a high field Thermo Scientific™ Q Exactive HF™ quadrupole-Orbitrap mass spectrometer equipped with an electrospray source. The ESI source parameters were the following: sheath gas 40, auxiliary gas 3, spray voltage 2.8 kV in negative and 3.5 kV in the positive mode, capillary temperature 280 °C, S-Lens RF level 30 and auxiliary gas heater 320 °C. Spectral data were acquired in profile mode. Resolution = 60.000, mass range = 60–900 m/z, AGC target 10^6, both in positive and negative polarities. Quantification was done through the areas of extracted ion chromatograms of $[M+H]^+$ and $[M-H]^-$ with 5 ppm mass tolerance on the $U^{12}C$ to $U^{13}C$ ratio.

4.2.5. Acidic Hydrolysis of the Pellet and Amino Acid Analysis

Acidic hydrolysis of the pellet resulting from the boiling ethanol extraction of samples of 1, 5, 10, and 15 spheroids pooled was based on a procedure described in detail elsewhere [53,54]. In short,

1 mL 6 M hydrochloric acid (Fluka, TraceSELECT from ≥37%) was added to the pellets, already in the conical screw cap vials (Bioquote Limited, York, United Kingdom); screw caps were tightly closed and the samples were hydrolyzed at 100 °C for 24 h. The hydrolyzed samples were evaporated to dryness and stored at −80 °C until analysis. Procedural blanks were also prepared to investigate possible background. Upon measurement, samples were reconstituted in 1 mL H_2O. A 1-to-10 dilution was done by taking 50 µL from the sample, adding 50 µL ISTD and 400 µL acetonitrile. NIST SRM 2389a amino acid standard (Sigma-Aldrich) was used to prepare an external calibration with internal standard and achieve absolute concentrations. The eight amino acids were subject to quantitative extraction and measurement according to [36] (alanine, arginine, glycine, histidine, lysine, phenylalanine, proline, tyrosine) were measured with a method described in detail elsewhere [35]. Shortly, the Agilent Infinity LC-System coupled to an Agilent 6490 triple quadrupole mass spectrometer was used with a HILIC separation, Waters Acquity BEH Amide (1.7 µm, 100 × 0.786 mm) column with 10 mM ammonium formate (pH 3.25) as eluent A and 80% acetonitrile 20% 10 mM ammonium formate (pH 3.25) as eluent B. Multiple reaction monitoring transitions were acquired in positive polarity.

4.3. Methods for Comparison Boiling Ethanol (BE) and Cold Methanol (CM) Extraction and Washing Procedures (OFF vs. ON) of 3D MTS

For this experiment, 3D MTS were grown as described above from 10×10^3 cells for 96 h.

4.3.1. Transfer of Spheroids

Sampling and transfer of spheroids were carried out with a 200 µL (Eppendorf, Vienna, Austria) pipette. The tip of the pipette tip was cut with a scissor (washed before in methanol:H_2O 50:50) so that the opening was slightly enlarged. The spheroid was taken up with the surrounding solution by the suction generated by the pipette and transferred from the plate into an Eppendorf tube.

4.3.2. "BE-OFF" Sample Preparation

The spheroids were transferred from the plate into conical screw cap vials (Bioquote Limited, York, United Kingdom), where they were washed three times with phosphate-buffered saline (PBS, Sigma-Aldrich, Vienna, Austria), quenched immediately with liquid nitrogen and stored at −80 °C until extraction. Upon extraction, 20 µL $U^{13}C$ internal standard was added as well as 180 µL 75% ethanol and put on 95 °C in the water bath for 5 min. After 5 min of sonication, samples were vortexed and centrifuged (14,000 rcf, 5 min, 4 °C) and supernatants transferred into MS-vials. Samples were measured directly without evaporation.

4.3.3. "CM-OFF" Sample Preparation

The spheroids were transferred from the plate into an Eppendorf tube, where they were washed three times with PBS and quenched immediately in liquid nitrogen and stored at −80 °C until extraction. Upon extraction, 20 µL $U^{13}C$ internal standard was added as well as 180 µL cold 80% methanol (−20 °C). After 5 min of sonication, samples were vortexed and centrifuged (14,000 rcf, 5 min, 4 °C) and supernatants transferred into MS-vials. Samples were measured directly without evaporation.

4.3.4. "BE-ON" Sample Preparation

The medium of spheroids was carefully aspirated by a multichannel pipette, while spheroids remained in the wells. Subsequently, the spheroids were washed with 200 µL PBS and quenched by liquid nitrogen. The spheroids still in the wells were stored at −80 °C until extraction. Plates were kept on ice during extraction. Upon extraction, 20 µL $U^{13}C$ internal standard was added to the well, then 80 µL 75% ethanol (room temperature, not hot yet) was added; in this amount, the spheroid was transferred to conical screw cap vials (Bioquote Limited, York, United Kingdom). One hundred µL more 75% ethanol was added to wash the well and transferred to the conical screw cap vials (Bioquote Limited, York, United Kingdom). Samples were kept on ice until the extraction of all samples was

completed. Samples were vortexed and put on 95 °C in the water bath for 5 min, then 5 min of sonication followed. Finally, samples were centrifuged (14,000 rcf, 5 min, 4 °C), and supernatants were transferred into MS-vials. Samples were measured directly without evaporation.

4.3.5. "CM-ON" Sample Preparation

The medium of spheroids was carefully aspirated by a multichannel pipette, while spheroids remained in the wells. Subsequently, the spheroids were washed with 200 µL PBS and quenched by liquid nitrogen. The spheroids still in the wells were stored at −80 °C until extraction. Plates were kept on ice during extraction. Upon extraction, 20 µL of the $U^{13}C$ internal standard was added, then 80 µL cold 80% methanol was added (−20 °C); in this amount, the spheroid was transferred to an Eppendorf-tube and 100 µL more cold 80% methanol was added to wash the well and transferred to the Eppendorf tube. Samples were kept on ice until the extraction of all samples was completed. After 5 min of sonication, samples were vortexed and centrifuged (14,000 rcf, 5 min, 4 °C), and the supernatants were transferred into MS-vials. Samples were measured directly without evaporation.

4.3.6. LC-MS Method Applied for Proof of Principle Experiment with Metallodrugs

The metabolite standards were purchased from Sigma-Aldrich or Fluka (Vienna, Austria) except for malic acid which was purchased from Merck (Vienna, Austria). The metabolomics experiment also included an external calibration with a calibration mix of 133 substances and internal standardization with $U^{13}C$-labeled yeast extract. Within every 10 injections, a blank was injected, as well as a pooled QC from extracts (all four groups represented in each: 200 µM KP1339-treated, 20 µM oxaliplatin-treated, control, control with 0.5% dimethylsulfoxid (DMSO)). We used high resolution Orbitrap MS coupled to Vanquish UPLC and with a HILIC separation, as described elsewhere [37]. MS-data were acquired with positive–negative switching and the extracted ion chromatograms were evaluated with Thermo Trace Finder, with the help of external calibration and the internal standard, absolute amounts were calculated in pmol. The normalization with total protein content resulted in pmol metabolite per µg protein.

4.3.7. Total Protein Content Determination

The protein concentration was assessed from the precipitate dissolved in 200 µL 0.05 M NaOH. For that purpose, the commercially available micro BCA protein assay kit (Thermo Fisher Scientific, Pierce Biotechnology, Rockford, IL, USA) was employed, according to the manufacturer's instructions.

4.4. Data Analysis

4.4.1. Targeted Metabolomics Data Treatment and Normalization

Targeted data evaluation of high-resolution mass spectrometry data of metabolites was performed in Thermo Trace Finder 4.1, while for the triple quadrupole data of amino acids hydrolyzed from pellet Agilent MassHunter was used. ^{13}C internal standardization using external calibration was employed for metabolites. All calibration curves were linear.

The dataset with absolute metabolite amounts and total protein contents was exported to Python, where the normalization with protein content was carried out, as well as filtering the dataset based on the performance of pooled quality control samples. (Missing values > 50%, relative standard deviation above 30%).

4.4.2. Exploratory Data Analysis

The MetaboAnalyst 4.0 Statistical Analysis module was used for further exploratory data analysis of dataset with absolute metabolite amounts normalized to total protein content. The default missing values imputation was used with a small number; autoscaling was applied before multivariate analysis.

4.4.3. Pathway Analysis

The MetaboAnalyst 4.0 [46] Pathway Analysis module was used, which combines pathway enrichment analysis and pathway topology analysis to identify the most relevant pathways involved in the conditions under study. As data input, the whole dataset with protein content normalized concentrations was used. Normalized concentrations were autoscaled; missing values imputed with a small number. The following parameters were used: pathway enrichment with "global test", pathway topology analysis with "relative-betweenness centrality", pathway library was homo sapiens KEGG, KEGG version Oct 2019.

Supplementary Materials: The following are available online at http://www.mdpi.com/2218-1989/9/12/304/s1, Table S1: 1x_5x_10x_15x_MTS. Table S2: washing extractions comparison, Table S3: proof Experiment Metallodrugs.

Author Contributions: Conceptualization, M.R. and G.K.; methodology M.R., M.A.J. and G.K.; formal analysis, M.R.; software, M.R.; validation, M.R.; investigation, M.R.; resources, M.A.J. and G.K.; data curation, M.R. and G.K.; writing—original draft preparation, M.R., E.R.; writing—review and editing, M.R., M.A.J., G.K.; visualization, M.R.; supervision, G.K.; M.R.; project administration, M.R., M.A.J. and G.K.; funding acquisition, B.K.K. and G.K.

Funding: This research received funding from Vienna Fund for Innovative Interdisciplinary Cancer Research. Open Access Funding by the University of Vienna.

Acknowledgments: This work is supported by the University of Vienna, the Faculty of Chemistry, the Vienna, Metabolomics Center (VIME; http://metabolomics.univie.ac.at/), the research platform Chemistry Meets Microbiology, the Mass Spectrometry Center (MSC) and Translational Cancer Therapy Research Cluster of the University of Vienna. We would like to thank for Yasin El Abiead, Michaela Schwaiger-Haber and Debora Wernitznig for helpful discussions and for supporting this work.

Conflicts of Interest: The authors declare no conflict of interest.

Abbreviations

Abbreviations of metabolites and their explanation used in this work.

Abbreviation	Explanation
5AMP, AMP	adenosine monophosphate
5CMP, CMP	cytidine monophosphate
5GMP, UMP	guanosine monophosphate
5UMP	uridine monophosphate
AAA	alpha aminoadipic acid
Ade	adenine
ADP	adenosine diphosphate
Ala	alanine
Arg	arginine
Asin	adenosine
Asn	aspragine
Asp	aspartic acid
DHAP	dihydroxyacetone phosphate
Gln	glutamine
Glu	glutamate
Gly	glycine
GMP	guanosine monophosphate
GSH	glutathione (reduced)
Gsin	guanosine
GSSG	Glutathione (oxidized)
His	histidine
H-Ser	homoserine
IMP	inosine monophosphate
Isin	inosine
K-Ile	ketoisoleucine
Lys	lysine

Met	methionine
NAD+	nicotinamide adenine dinucleotide (oxidized)
NADP+	nicotinamide adenine dinucleotide phosphate (oxidized)
OAS	O-acetylserine
Phe	phenylalanine
Pro	proline
Pyr	pyruvate
Rib-5-P	ribose 5-phosphate/ribulose 5-phosphate
Ser	serine
Thr	threonine
Trp	tryptophan
Tyr	tyrosine

Appendix A

Table S1. Summary of the experiment which had the aim of determining the minimal number of MTS required for a metabolomics experiment. Relative responses of 1, 5, 10 and 15 MTS from the boiling ethanol extracts. Absolute amounts of amino acids [nmol] from hydrolysed pellets. Cell numbers and viability. Parameters of the normalized linear regressions.

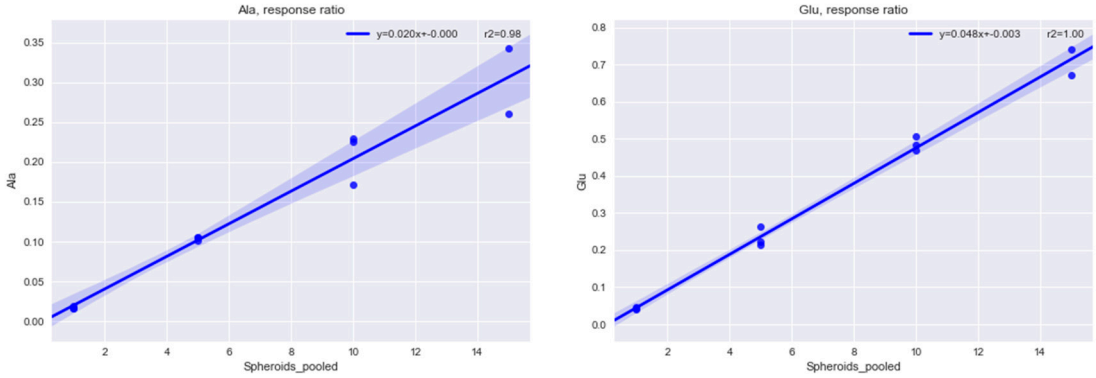

Figure A1. Relative responses ($^{12}C/^{13}C$) of alanine and glutamate as selected examples from a single ($N = 3$), 5 ($N = 3$), 10 ($N = 3$), 15 ($N = 2$) multicellular tumor spheroids. Sample preparation applied boiling ethanol extraction with $U^{13}C$ internal standardization and LC high-resolution mass spectrometry. Investigated metabolites showed high linear correlation.

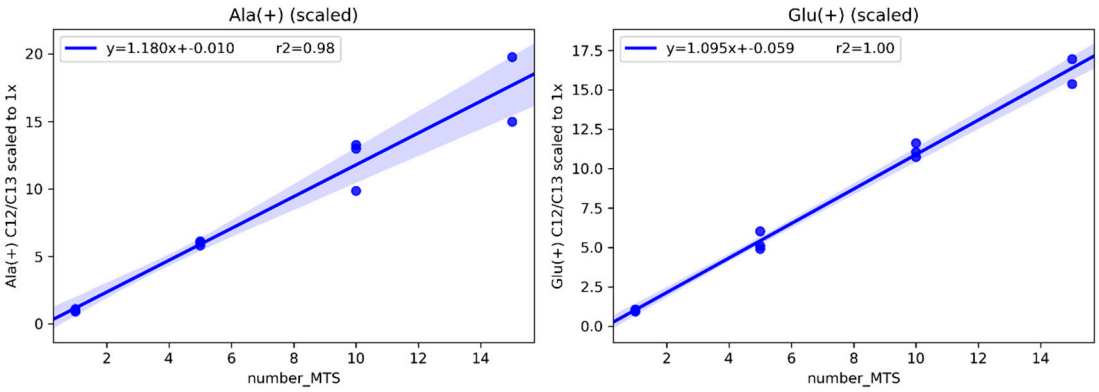

Figure A2. Scaled relative responses ($^{12}C/^{13}C$) of alanine and glutamate as selected examples from a single ($N = 3$), 5 ($N = 3$), 10 ($N = 3$), 15 ($N = 2$) multicellular tumor spheroids: relative responses were scaled to the mean relative response in single multicellular tumor spheroids ($N = 3$). Sample preparation applied boiling ethanol extraction with $U^{13}C$ internal standardization and LC high-resolution mass spectrometry. Alanine and glutamate are shown from the investigated compounds.

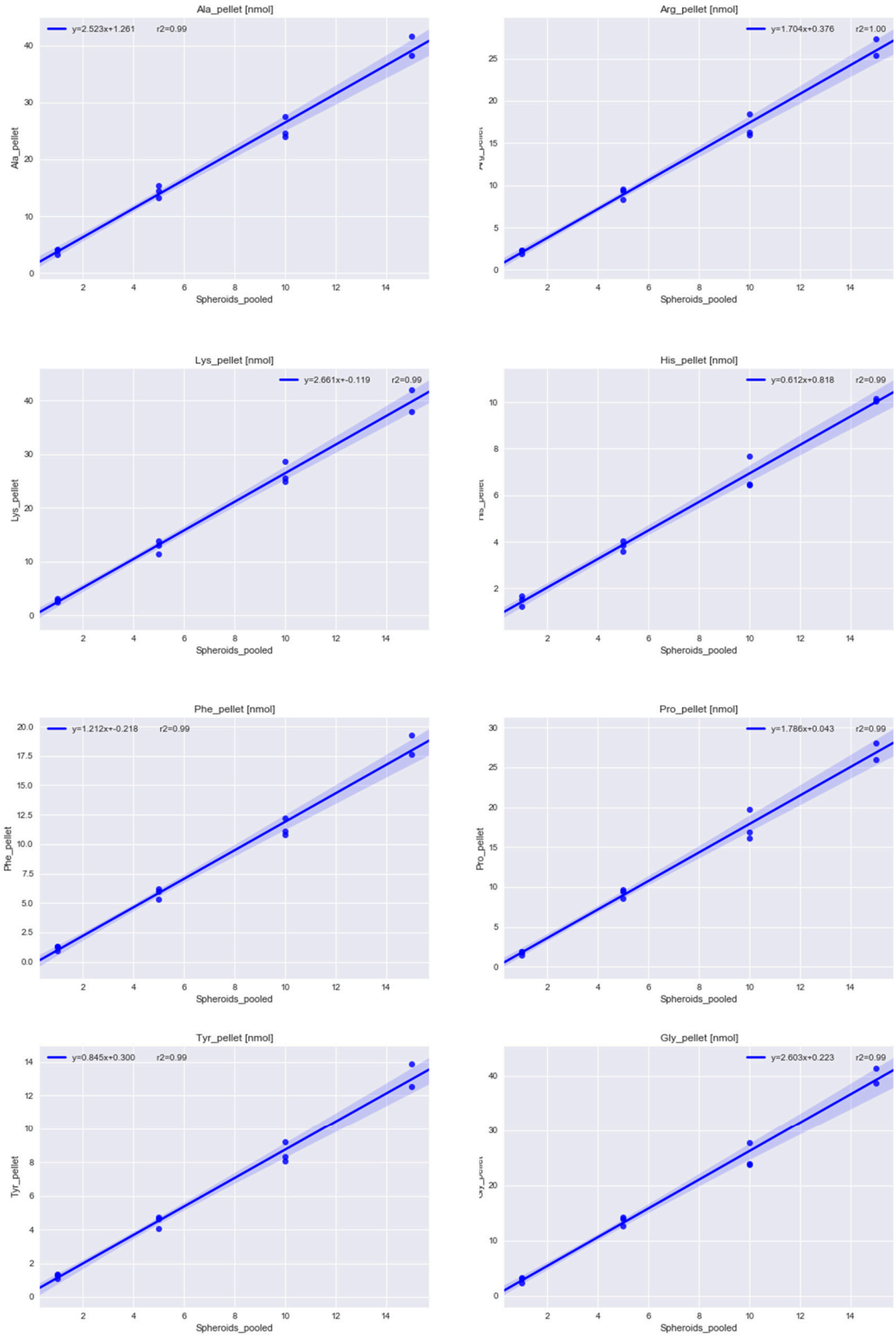

Figure A3. Absolute amounts in nmol of amino acids after acidic hydrolysis of the pellet containing 1 (N = 3), 5 (N = 3), 10 (N = 3) and 15 (N = 2) multicellular tumor spheroids. The pellets are resulting from the high molecular fraction of the boiling ethanol extraction and centrifugation. Amino acid amounts from the proteins show a strong linear correlation with the number of spheroids in the sample.

Table S2. Summary of the experiment comparing the different sample preparation strategies with three washing steps vs. single washing on the plate and boiling ethanol vs. cold methanol extraction. Summary of the absolute amounts of selected metabolites. Individual absolute amounts in samples.

Table S3. Summary of the proof of principle experiment with metallodrugs. Absolute amounts of metabolites in samples and RSDs. Absolute amounts of metabolites normalized to total protein content and RSDs. Absolute amounts of metabolites normalized to total protein content with missing value imputation. Absolute amounts of metabolites normalized to total protein content with missing value imputation and autoscaling. Total protein content in the samples. KEGG pathways affected by Oxaliplatin treatment. KEGG pathways affected by KP1339 treatment. Significant compounds ($p < 0.05$) based on oxaliplatin treatment. Significant compounds ($p < 0.05$) based on KP1339 treatment.

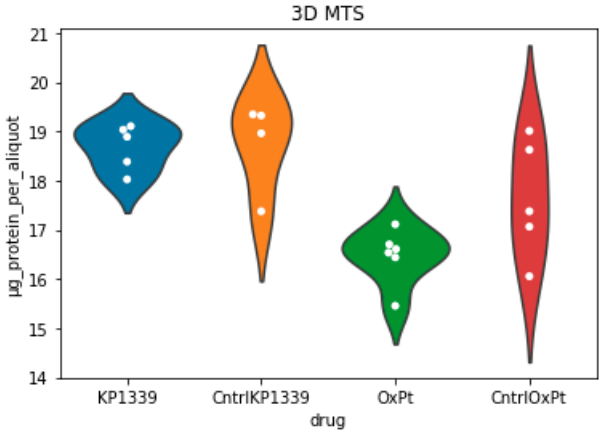

Figure A4. Swarm and violinplot of total protein content [µg] in single 3D MTS cultures (10×10^3 cells seeded, 8 days cultivation diameter 790 ± 22 µm at time of treatment) after 24 h of incubation with 200 µM KP1339, 20 µM Oxaliplatin, growth medium (CntrlOxPt), growth medium with 0.5% DMSO (CntrlKP1339). Protein content is determined by the Thermo micro BCA kit from the high molecular fraction in the pellet.

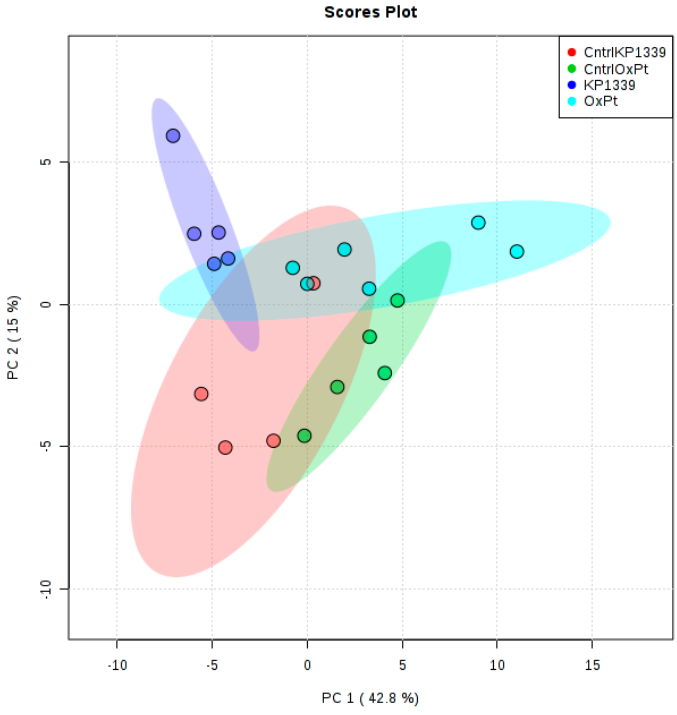

Figure A5. PCA scores plot of absolute amounts of metabolites normalized to protein content of samples from single 3D MTS. Spheroids were treated for 24 h with either 200 µM KP1339, 20 µM Oxaliplatin (OxPt), medium (CntrlOxPt) or medium with 0.5% DMSO (CntrlKP1339). Extraction with cold methanol and internal standardization, measurement by HILIC high-resolution Orbitrap MS.

References

1. Stock, K.; Estrada, M.F.; Vidic, S.; Gjerde, K.; Rudisch, A.; Santo, V.E.; Barbier, M.; Blom, S.; Arundkar, S.C.; Selvam, I.; et al. Capturing tumor complexity in vitro: Comparative analysis of 2D and 3D tumor models for drug discovery. *Sci. Rep.* **2016**, *6*, 28951. [CrossRef] [PubMed]
2. Hirschhaeuser, F.; Menne, H.; Dittfeld, C.; West, J.; Mueller-Klieser, W.; Kunz-Schughart, L.A. Multicellular tumor spheroids: An underestimated tool is catching up again. *J. Biotechnol.* **2010**, *148*, 3–15. [CrossRef] [PubMed]
3. Mehta, G.; Hsiao, A.Y.; Ingram, M.; Luker, G.D.; Takayama, S. Opportunities and Challenges for use of Tumor Spheroids as Models to Test Drug Delivery and Efficacy. *J. Control. Release* **2012**, *164*, 192–204. [CrossRef] [PubMed]
4. Costa, E.C.; Moreira, A.F.; de Melo-Diogo, D.; Gaspar, V.M.; Carvalho, M.P.; Correia, I.J. 3D tumor spheroids: An overview on the tools and techniques used for their analysis. *Biotechnol. Adv.* **2016**, *34*, 1427–1441. [CrossRef] [PubMed]
5. Stewart, D.J. Mechanisms of resistance to cisplatin and carboplatin. *Crit. Rev. Oncol. Hematol.* **2007**, *63*, 12–31. [CrossRef]
6. Edmondson, R.; Broglie, J.J.; Adcock, A.F.; Yang, L. Three-Dimensional Cell Culture Systems and Their Applications in Drug Discovery and Cell-Based Biosensors. *Assay Drug Dev. Technol.* **2014**, *12*, 207–218. [CrossRef]
7. Tafani, M.; Sansone, L.; Limana, F.; Arcangeli, T.; De Santis, E.; Polese, M.; Fini, M.; Russo, M.A. The Interplay of Reactive Oxygen Species, Hypoxia, Inflammation, and Sirtuins in Cancer Initiation and Progression. *Oxid. Med. Cell. Longev.* **2016**, *2016*, 18. [CrossRef]
8. Kondoh, M.; Ohga, N.; Akiyama, K.; Hida, Y.; Maishi, N.; Towfik, A.M.; Inoue, N.; Shindoh, M.; Hida, K. Hypoxia-Induced Reactive Oxygen Species Cause Chromosomal Abnormalities in Endothelial Cells in the Tumor Microenvironment. *PLoS ONE* **2013**, *8*, e80349. [CrossRef]
9. Wang, Q.-S.; Zheng, Y.-M.; Dong, L.; Ho, Y.-S.; Guo, Z.; Wang, Y.-X. Role of mitochondrial reactive oxygen species in hypoxia-dependent increase in intracellular calcium in pulmonary artery myocytes. *Free Radic. Biol. Med.* **2007**, *42*, 642–653. [CrossRef]
10. Hanahan, D.; Weinberg, R.A. Hallmarks of Cancer: The Next Generation. *Cell* **2011**, *144*, 646–674. [CrossRef]
11. Armitage, E.G.; Southam, A.D. Monitoring cancer prognosis, diagnosis and treatment efficacy using metabolomics and lipidomics. *Metabolomics* **2016**, *12*, 146. [CrossRef] [PubMed]
12. do Valle, Í.F.; Menichetti, G.; Simonetti, G.; Bruno, S.; Zironi, I.; Durso, D.F.; Mombach, J.C.M.; Martinelli, G.; Castellani, G.; Remondini, D. Network integration of multi-tumour omics data suggests novel targeting strategies. *Nat. Commun.* **2018**, *9*, 4514. [CrossRef] [PubMed]
13. Beger, R.D. A Review of Applications of Metabolomics in Cancer. *Metabolites* **2013**, *3*, 552–574. [CrossRef] [PubMed]
14. Fiehn, O. Metabolomics—The link between genotypes and phenotypes. *Plant Mol. Biol.* **2002**, *48*, 155–171. [CrossRef] [PubMed]
15. Patti, G.J.; Yanes, O.; Siuzdak, G. Metabolomics: The apogee of the omic triology. *Nat. Rev. Mol. Cell Biol.* **2012**, *13*, 263–269. [CrossRef] [PubMed]
16. Armitage, E.G.; Barbas, C. Metabolomics in cancer biomarker discovery: Current trends and future perspectives. *J. Pharm. Biomed. Anal.* **2014**, *87*, 1–11. [CrossRef]
17. Beger, R.D. Interest is high in improving quality control for clinical metabolomics: Setting the path forward for community harmonization of quality control standards. *Metabolomics* **2018**, *15*, 1. [CrossRef]
18. Cui, L.; Lu, H.; Lee, Y.H. Challenges and emergent solutions for LC-MS/MS based untargeted metabolomics in diseases. *Mass Spectrom. Rev.* **2018**, *37*, 772–792. [CrossRef]
19. Schwaiger, M.; Schoeny, H.; Abiead, Y.E.; Hermann, G.; Rampler, E.; Koellensperger, G. Merging metabolomics and lipidomics into one analytical run. *Analyst* **2018**, *144*, 220–229. [CrossRef]
20. León, Z.; García-Cañaveras, J.C.; Donato, M.T.; Lahoz, A. Mammalian cell metabolomics: Experimental design and sample preparation. *Electrophoresis* **2013**, *34*, 2762–2775. [CrossRef]
21. Coloff, J.L.; Murphy, J.P.; Braun, C.R.; Harris, I.S.; Shelton, L.M.; Kami, K.; Gygi, S.P.; Selfors, L.M.; Brugge, J.S. Differential Glutamate Metabolism in Proliferating and Quiescent Mammary Epithelial Cells. *Cell Metab.* **2016**, *23*, 867–880. [CrossRef] [PubMed]

22. Fan, T.W.-M.; El-Amouri, S.S.; Macedo, J.K.A.; Wang, Q.J.; Song, H.; Cassel, T.; Lane, A.N. Stable Isotope-Resolved Metabolomics Shows Metabolic Resistance to Anti-Cancer Selenite in 3D Spheroids versus 2D Cell Cultures. *Metabolites* **2018**, *8*, 40. [CrossRef] [PubMed]
23. Jones, D.T.; Valli, A.; Haider, S.; Zhang, Q.; Smethurst, E.A.; Schug, Z.T.; Peck, B.; Aboagye, E.O.; Critchlow, S.E.; Schulze, A.; et al. 3D Growth of Cancer Cells Elicits Sensitivity to Kinase Inhibitors but Not Lipid Metabolism Modifiers. *Mol. Cancer Ther.* **2019**, *18*, 376–388. [CrossRef] [PubMed]
24. Vorrink, S.U.; Ullah, S.; Schmidt, S.; Nandania, J.; Velagapudi, V.; Beck, O.; Ingelman-Sundberg, M.; Lauschke, V.M. Endogenous and xenobiotic metabolic stability of primary human hepatocytes in long-term 3D spheroid cultures revealed by a combination of targeted and untargeted metabolomics. *FASEB J.* **2017**, *31*, 2696–2708. [CrossRef]
25. Sato, M.; Kawana, K.; Adachi, K.; Fujimoto, A.; Yoshida, M.; Nakamura, H.; Nishida, H.; Inoue, T.; Taguchi, A.; Takahashi, J.; et al. Spheroid cancer stem cells display reprogrammed metabolism and obtain energy by actively running the tricarboxylic acid (TCA) cycle. *Oncotarget* **2016**, *7*, 33297–33305. [CrossRef]
26. Eljack, N.D.; Ma, H.-Y.M.; Drucker, J.; Shen, C.; Hambley, T.W.; New, E.J.; Friedrich, T.; Clarke, R.J. Mechanisms of cell uptake and toxicity of the anticancer drug cisplatin. *Metallomics* **2014**, *6*, 2126–2133. [CrossRef]
27. Gibson, D. The mechanism of action of platinum anticancer agents—What do we really know about it? *Dalton Trans.* **2009**, *48*, 10681–10689. [CrossRef]
28. Johnstone, T.C.; Suntharalingam, K.; Lippard, S.J. The Next Generation of Platinum Drugs: Targeted Pt (II) Agents, Nanoparticle Delivery and Pt (IV) Prodrugs. *Chem. Rev.* **2016**, *116*, 3436–3486. [CrossRef]
29. Mucaki, E.J.; Zhao, J.Z.L.; Lizotte, D.J.; Rogan, P.K. Predicting responses to platin chemotherapy agents with biochemically-inspired machine learning. *Signal Transduct. Target. Ther.* **2019**, *4*, 1. [CrossRef]
30. Wang, D.; Lippard, S.J. Cellular processing of platinum anticancer drugs. *Nat. Rev. Drug Discov.* **2005**, *4*, 307–320. [CrossRef]
31. Mjos, K.D.; Orvig, C. Metallodrugs in Medicinal Inorganic Chemistry. *Chem. Rev.* **2014**, *114*, 4540–4563. [CrossRef] [PubMed]
32. Canelas, A.B.; ten Pierick, A.; Ras, C.; Seifar, R.M.; van Dam, J.C.; van Gulik, W.M.; Heijnen, J.J. Quantitative evaluation of intracellular metabolite extraction techniques for yeast metabolomics. *Anal. Chem.* **2009**, *81*, 7379–7389. [CrossRef] [PubMed]
33. Gonzalez, B.; François, J.; Renaud, M. A rapid and reliable method for metabolite extraction in yeast using boiling buffered ethanol. *Yeast* **1997**, *13*, 1347–1355. [CrossRef]
34. Dettmer, K.; Nürnberger, N.; Kaspar, H.; Gruber, M.A.; Almstetter, M.F.; Oefner, P.J. Metabolite extraction from adherently growing mammalian cells for metabolomics studies: Optimization of harvesting and extraction protocols. *Anal. Bioanal. Chem.* **2011**, *399*, 1127–1139. [CrossRef] [PubMed]
35. Hermann, G.; Schwaiger, M.; Volejnik, P.; Koellensperger, G. 13C-labelled yeast as internal standard for LC–MS/MS and LC high resolution MS based amino acid quantification in human plasma. *J. Pharm. Biomed. Anal.* **2018**, *155*, 329–334. [CrossRef] [PubMed]
36. Hoofnagle, A.N.; Whiteaker, J.R.; Carr, S.A.; Kuhn, E.; Liu, T.; Massoni, S.A.; Thomas, S.N.; Townsend, R.R.; Zimmerman, L.J.; Boja, E.; et al. Recommendations for the generation, quantification, storage and handling of peptides used for mass spectrometry-based assays. *Clin. Chem.* **2016**, *62*, 48–69. [CrossRef]
37. Galvez, L.; Rusz, M.; Schwaiger, M.; Abiead, Y.E.; Hermann, G.; Jungwirth, U.; Berger, W.; Keppler, B.K.; Jakupec, M.; Koellensperger, G. Preclinical studies on metal based anticancer drugs as enabled by integrated metallomics and metabolomics. *Metallomics* **2019**, *11*, 1716–1728. [CrossRef]
38. Bruno, P.M.; Liu, Y.; Park, G.Y.; Murai, J.; Koch, C.E.; Eisen, T.J.; Pritchard, J.R.; Pommier, Y.; Lippard, S.J.; Hemann, M.T. A subset of platinum-containing chemotherapeutic agents kill cells by inducing ribosome biogenesis stress rather than by engaging a DNA damage response. *Nat. Med.* **2017**, *23*, 461–471. [CrossRef]
39. Schoenhacker-Alte, B.; Mohr, T.; Pirker, C.; Kryeziu, K.; Kuhn, P.-S.; Buck, A.; Hofmann, T.; Gerner, C.; Hermann, G.; Koellensperger, G.; et al. Sensitivity towards the GRP78 inhibitor KP1339/IT-139 is characterized by apoptosis induction via caspase 8 upon disruption of ER homeostasis. *Cancer Lett.* **2017**, *404*, 79–88. [CrossRef]
40. Terenzi, A.; Pirker, C.; Keppler, B.K.; Berger, W. Anticancer metal drugs and immunogenic cell death. *J. Inorg. Biochem.* **2016**, *165*, 71–79. [CrossRef]

41. Kepp, O.; Senovilla, L.; Vitale, I.; Vacchelli, E.; Adjemian, S.; Agostinis, P.; Apetoh, L.; Aranda, F.; Barnaba, V.; Bloy, N.; et al. Consensus guidelines for the detection of immunogenic cell death. *Oncoimmunology* **2014**, *3*, e955691. [CrossRef] [PubMed]
42. Wernitznig, D.; Kiakos, K.; Del Favero, G.; Harrer, N.; Machat, H.; Osswald, A.; Jakupec, M.A.; Wernitznig, A.; Sommergruber, W.; Keppler, B.K. First-in-class ruthenium anticancer drug (KP1339/IT-139) induces an immunogenic cell death signature in colorectal spheroids in vitro. *Met. Integr. Biomet. Sci.* **2019**, *11*, 1044–1048. [CrossRef] [PubMed]
43. Broadhurst, D.; Goodacre, R.; Reinke, S.N.; Kuligowski, J.; Wilson, I.D.; Lewis, M.R.; Dunn, W.B. Guidelines and considerations for the use of system suitability and quality control samples in mass spectrometry assays applied in untargeted clinical metabolomic studies. *Metabolomics* **2018**, *14*, 72. [CrossRef] [PubMed]
44. Dunn, W.B.; Broadhurst, D.I.; Edison, A.; Guillou, C.; Viant, M.R.; Bearden, D.W.; Beger, R.D. Quality assurance and quality control processes: Summary of a metabolomics community questionnaire. *Metabolomics* **2017**, *13*, 50. [CrossRef]
45. Alcindor, T.; Beauger, N. Oxaliplatin: A review in the era of molecularly targeted therapy. *Curr. Oncol.* **2011**, *18*, 18–25. [CrossRef]
46. Chong, J.; Xia, J. MetaboAnalystR: An R package for flexible and reproducible analysis of metabolomics data. *Bioinformatics* **2018**, *34*, 4313–4314. [CrossRef]
47. Cavill, R.; Kamburov, A.; Ellis, J.K.; Athersuch, T.J.; Blagrove, M.S.C.; Herwig, R.; Ebbels, T.M.D.; Keun, H.C. Consensus-Phenotype Integration of Transcriptomic and Metabolomic Data Implies a Role for Metabolism in the Chemosensitivity of Tumour Cells. *PLoS Comput. Biol.* **2011**, *7*, e1001113. [CrossRef]
48. Von Stechow, L.; Ruiz-Aracama, A.; van de Water, B.; Peijnenburg, A.; Danen, E.; Lommen, A. Identification of Cisplatin-Regulated Metabolic Pathways in Pluripotent Stem Cells. *PLoS ONE* **2013**, *8*, e76476. [CrossRef]
49. Gifford, J.B.; Huang, W.; Zeleniak, A.E.; Hindoyan, A.; Wu, H.; Donahue, T.R.; Hill, R. Expression of GRP78, Master Regulator of the Unfolded Protein Response, increases chemoresistance in pancreatic ductal adenocarcinoma. *Mol. Cancer Ther.* **2016**, *15*, 1043–1052. [CrossRef]
50. Kreutz, D.; Bileck, A.; Plessl, K.; Wolrab, D.; Groessl, M.; Keppler, B.K.; Meier, S.M.; Gerner, C. Response Profiling Using Shotgun Proteomics Enables Global Metallodrug Mechanisms of Action To Be Established. *Chemistry* **2017**, *23*, 1881–1890. [CrossRef]
51. Gonen, N.; Meller, A.; Sabath, N.; Shalgi, R. Amino Acid Biosynthesis Regulation during Endoplasmic Reticulum Stress Is Coupled to Protein Expression Demands. *IScience* **2019**, *19*, 204–213. [CrossRef] [PubMed]
52. Scannell, J.W.; Blanckley, A.; Boldon, H.; Warrington, B. Diagnosing the decline in pharmaceutical R & D efficiency. *Nat. Rev. Drug Discov.* **2012**, *11*, 191–200. [PubMed]
53. Hermann, G.; Møller, L.H.; Gammelgaard, B.; Hohlweg, J.; Mattanovich, D.; Hann, S.; Koellensperger, G. In vivo synthesized 34 S enriched amino acid standards for species specific isotope dilution of proteins. *J. Anal. At. Spectrom.* **2016**, *31*, 1830–1835. [CrossRef]
54. Rampler, E.; Dalik, T.; Stingeder, G.; Hann, S.; Koellensperger, G. Sulfur containing amino acids—Challenge of accurate quantification. *J. Anal. At. Spectrom.* **2012**, *27*, 1018–1023. [CrossRef]

scientific reports

Check for updates

OPEN

Morpho-metabotyping the oxidative stress response

Mate Rusz[1,2], Giorgia Del Favero[3,4], Yasin El Abiead[1], Christopher Gerner[1], Bernhard K. Keppler[2,6], Michael A. Jakupec[2,6] & Gunda Koellensperger[1,5,6]✉

Oxidative stress and reactive oxygen species (ROS) are central to many physiological and pathophysiological processes. However, due to multiple technical challenges, it is hard to capture a comprehensive readout of the cell, involving both biochemical and functional status. We addressed this problem by developing a fully parallelized workflow for metabolomics (providing absolute quantities for > 100 metabolites including TCA cycle, pentose phosphate pathway, purine metabolism, glutathione metabolism, cysteine and methionine metabolism, glycolysis and gluconeogenesis) and live cell imaging microscopy. The correlative imaging strategy was applied to study morphological and metabolic adaptation of cancer cells upon short-term hydrogen peroxide (H_2O_2) exposure in vitro. The combination provided rich metabolic information at the endpoint of exposure together with imaging of mitochondrial effects. As a response, superoxide concentrations were elevated with a strong mitochondrial localization, and multi-parametric image analysis revealed a shift towards fragmentation. In line with this, metabolism reflected both the impaired mitochondrial function and shifts to support the first-line cellular defense and compensate for energy loss. The presented workflow combining high-end technologies demonstrates the applicability for the study of short-term oxidative stress, but it can be suitable for the in-depth study of various short-term oxidative and other cellular stress-related phenomena.

The central role of reactive oxygen species (ROS) in tuning cell physiology includes essential regulation of cell functional features and proliferation[1–6]. Oxidative stress is also crucial in pathophysiology, as there is a key interplay between ROS, hypoxia and inflammation during tumorigenesis and progression[7–9]. Intriguingly, exploiting redox homeostasis presents a therapeutic opportunity and can also be used for fighting cancer, as cancer cells are close to their antioxidant threshold, while non-cancerous cells can still extend their antioxidant capacities[10–12]. In addition, redox stress is a prerequisite for complex biological phenomena, such as endoplasmic reticulum stress and immunogenic cell death[13] and for redox activation of anticancer prodrugs[14]. Moreover, uncontrolled ROS production was shown to accompany toxicity as exerted by environmental pollutants[15,16], food contaminants[17,18], or therapy[19]. Upon such induction of cellular stress, cell fate is determined by the nature and the strength of the stimulus, as well as typically by the type of cell. Additionally, the coordinated interplay of response pathways and regulatory mechanisms is decisive for resisting and restoring perturbed homeostasis, such as the delicate balance between (oxidative) damage, repair, defense, autophagy and reprogramming. Nevertheless, integrity cannot be maintained, despite adaptations, above a critical threshold and the reprogramming changes from the support of survival to induction of cell cycle arrest, senescence, or some form of cell death (apoptosis, necrosis, autophagic cell death)[20–22].

Under physiological conditions the bulk of ROS originate from the mitochondria, as side products of aerobic respiration, thus representing a possible source of internal stress. All these aspects make the study of redox stress in a mitochondrial context relevant, both in a functional, spatial and mechanistic perspective. Nevertheless, informative measurement remains challenging.

Metabolomics can capture the molecular signature of the phenotype and thus provides the most functional information[23]. It offers an interrogation window into both cellular energy and redox state. Mass spectrometry-based cellular metabolic phenotyping proved to be powerful in diverse cutting-edge applications ranging from

[1]Institute of Analytical Chemistry, University of Vienna, Währinger Str. 38, 1090 Vienna, Austria. [2]Institute of Inorganic Chemistry, University of Vienna, Währinger Str. 42, 1090 Vienna, Austria. [3]Department of Food Chemistry and Toxicology, Faculty of Chemistry, University of Vienna, Währinger Straße 38-40, 1090 Vienna, Austria. [4]Core Facility Multimodal Imaging Faculty of Chemistry, University of Vienna, Währinger Straße 38-40, 1090 Vienna, Austria. [5]Vienna Metabolomics Center (VIME), University of Vienna, Althanstraße 14, 1090 Vienna, Austria. [6]Research Network Chemistry Meets Microbiology, Althanstraße 14, 1090 Vienna, Austria. ✉email: gunda.koellensperger@univie.ac.at

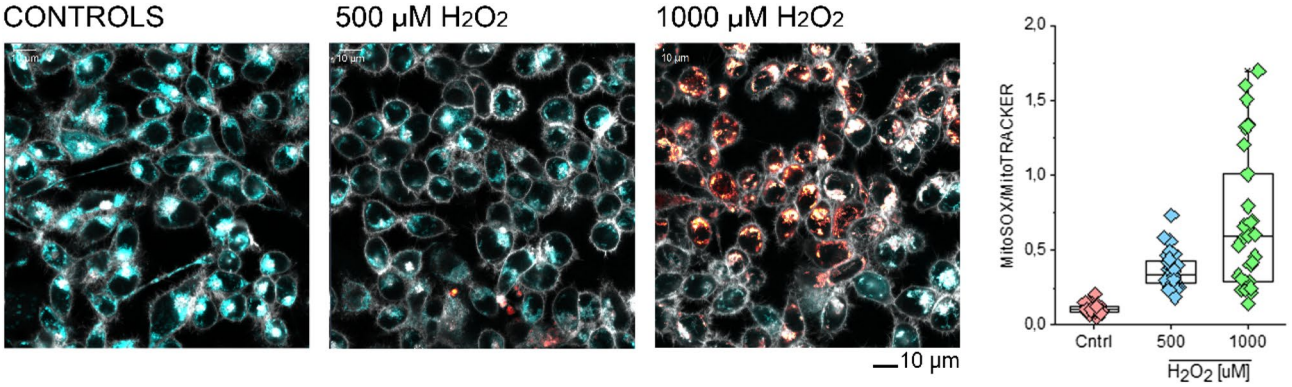

Figure 1. Live cell imaging: effect of hydrogen peroxide treatment. Representative images of the appearance of HCT116 colon cancer cells after staining with MitoSOX (orange, mitochondrial superoxide quantification) and MitoTracker (light blue, mitochondrial morphology). The plasma membrane was counterstained with CellMask (depicted in grey). The increasing MitoSOX to MitoTracker signal ratio upon external hydrogen peroxide treatment (500–1000 µM) in comparison to controls (Cntrl) implies the accumulation of superoxide anions within the mitochondria. Both treatments were different in comparison to controls (Mann–Whitney test; $p < 0.001$).

disease etiology to toxicology. While the toolsets are well established for cellular studies using > 100,000 cells, organelle-specific metabolomics is still in its infancy. The challenge lies in the sample preparation step. Typically, organelle fractionation requires conditions jeopardizing unbiased metabolomics. Therefore, most mitochondrial studies lack comprehensiveness so far, e.g., a recent study introduced NADPH imaging at subcellular resolution based on autofluorescence[24]. Using selective redox probes, only specific aspects of redox status (e.g., the redox pair GSH/GSSG) are unraveled, while secondary effects on metabolism and cellular status remain hidden. Recently, mitochondrial metabolomics on advanced cell models obtained by recombinant DNA technology was proposed. A seminal study by Chen et al.[25] allowed to selectively isolate and extract mitochondrial metabolites. The described method enabled rapid mitochondrial isolation by an epitope-tagged mitochondrial membrane protein.

In this work, we propose an alternative correlative imaging workflow that enables to capture metabolome profiles of mitochondrial ROS response, without mitochondrial isolation steps. More specifically, we combine live cell imaging and metabolomics in a strictly parallel manner. Thereby, the metabolome signatures can be addressed as molecular read-outs of mitochondrial morphological changes. To date, the number of applicable probes in cellular microscopy remains low, despite spectral multiplexing. Thus, integrating state-of-the-art metabolomics can expand the information content of imaging. A proof-of-principle experiment involved cancer cells exposed to hydrogen peroxide, modulating both the redox status and the energy metabolism. The *in-depth* metabolic profile of HCT116 colorectal carcinoma cells upon oxidative stress is obtained by high-resolution mass spectrometry combined with hydrophilic interaction chromatography. We specifically address the accurate determination of redox-sensitive thiol-containing metabolites by derivatization upon extraction. This information was complemented with the morphological characterization of the mitochondrial network obtained with live cell imaging. HCT116 cells are widely used to screen the cytotoxic potency of anticancer agents in vitro[10,26–28] as well as to investigate the potential effects of bioactive food constituents[29,30]. Here, we aim to pave the way for the application of combined metabolomics and live cell imaging methodology and expand the toolbox to study redox stress in metabolism and cellular morphometric adaptation. In order to demonstrate the applicability of the workflow, we take advantage of the large body of literature in oxidative stress research and seek to capture multiple established notions simultaneously and their possible correlations.

Results

The correlative metabolomics/imaging method comprised parallel in vitro experiments followed by tailored sample preparation for metabolomics and staining for microscopy. To achieve the highest degree of parallelization, cells were seeded in the same surface density and ratio of cell number to total medium volume, utilizing live cell imaging compatible multiwell plates and media.

In a proof-of-principle experiment, HCT116 colon cancer cells were exposed to hydrogen peroxide for a short period (2h) in live cell imaging medium and this perturbation could be investigated on both morphological and molecular levels. Microscopic analysis ensured the responsivity of our cell type to the stimulation protocol, albeit maintaining cell integrity and spatial resolution.

A concentration-dependent increase of the mitochondrial superoxide (expressed as MitoSox/MitoTracker signal ratio, Fig. 1) was found. Since structural integrity is tightly related to functional status[31–33], a multiparametric image analysis of the mitochondrial network was also implemented according to the protocol of Valente and colleagues[34]. Intriguingly, we observed a rather consistent effect of H_2O_2 stimulation on the average mitochondrial length and to a certain extent also on the mitochondrial network (ramification and junctions, Fig. 2). These responses seemed more stable at a concentration of 500 µM than at 1000 µM. Indeed, incubation with the highest concentration of H_2O_2 was also accompanied by cell morphological changes, possibly accounting for the loss of specificity for some structural parameters at the onset of toxicity and increased mitochondrial density and

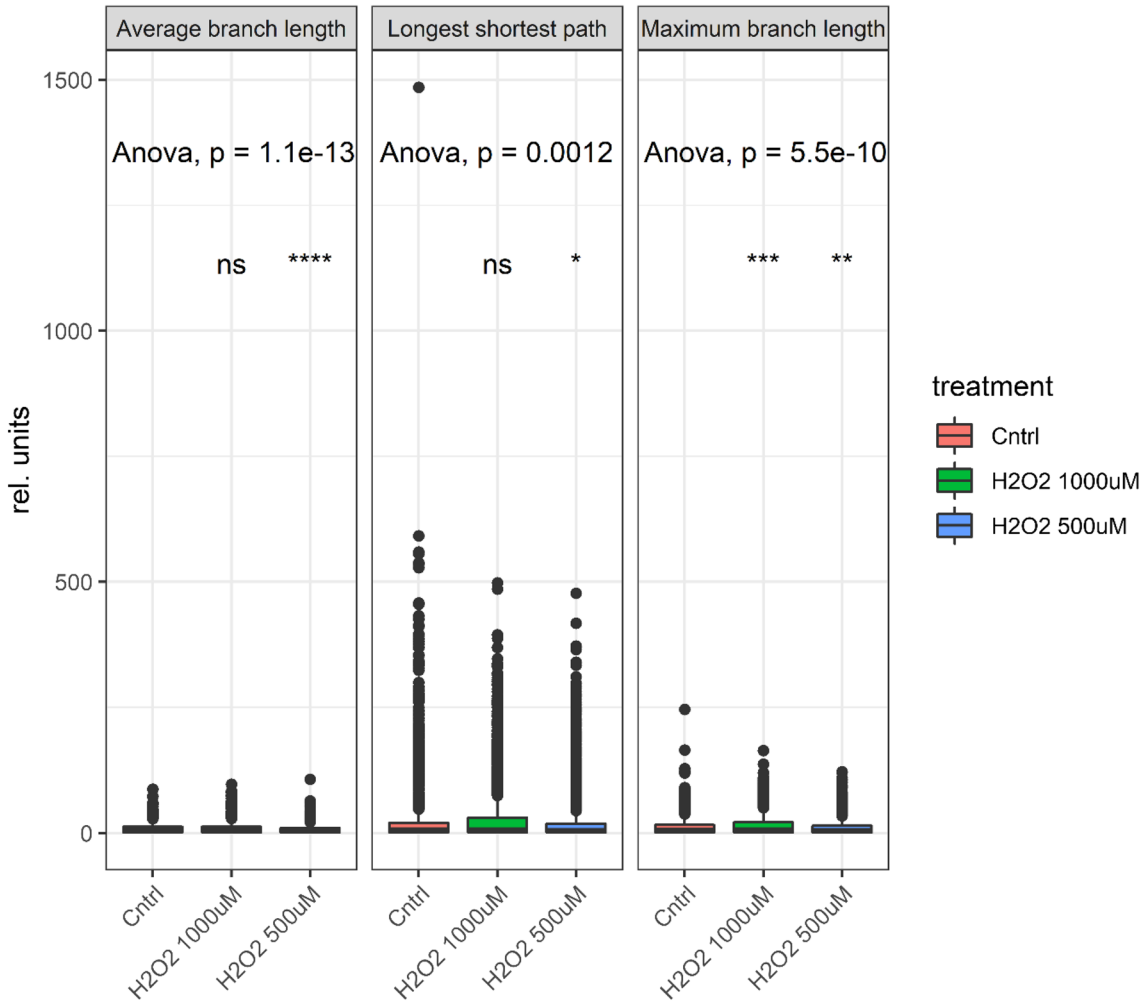

Figure 2. Selected significantly changed morphological features. Average branch length, longest shortest path and maximum branch length in relative units (rel.units) with 1000 µM and 500 µM H_2O_2 treatment, and control (Cntrl). Analysis of variance (ANOVA) based on comparison with control. (N = 5790, ns: not significant, $p > 0.05$, *$p \leq 0.05$, **$p \leq 0.01$, ***$p \leq 0.001$, ****$p \leq 0.0001$)

clustering in the peri-nuclear region[31]. To support this interpretation, a significant decrease in the average and maximal branch length of the mitochondrial network could be measured after incubation with 1000 µM H_2O_2.

The parallel metabolomics experiments were performed under an exposure to 500 µM H_2O_2 , as a molecular readout for the endpoint of exposure, since the interpretation would be challenged by the observed loss of morphologic specificity at higher concentrations. Sample preparation for metabolomics comprised internal standardization by fully ^{13}C-enriched yeast and a derivatization step targeting all thiol-containing metabolites. In our experimental model, metabolome adaptation was substantial despite the relatively short stimulation protocol (2 h). Absolute concentrations were determined for 100 + metabolites covering multiple relevant pathways of the primary metabolome. Among others, energy metabolism, DNA synthesis, TCA cycle, glycolysis, pentose phosphate pathway, amino acid metabolism, and glutathione synthesis were covered in-depth with this method. Absolute concentrations were obtained using fully labelled internal standards in combination with external calibration. As a novelty, the applied HILIC-HRMS covered metabolites as published elsewhere[35] together with metabolites along the sulfur pathway, which are key factors for the redox balance of a cell. Primary thiols (glutathione, cysteine, homocysteine and glutamyl-cysteine) were assessed as N-ethylmaleimide (NEM) derivatives to prevent oxidation during sample preparation and storage and to prolong stability[36]. Internal standardization and normalization to the protein content resulted in excellent analytical figures of merit and enabled absolute quantification of > 100 metabolites. Moreover, the presence of fully labeled ^{13}C biomass monitored unwanted oxidation artifacts during sample preparation[37]. This material, beyond enabling absolute quantification on LC–MS platforms and compensating for losses during sample preparation, was shown to form GSSG with typical isotopologue patterns (^{13}C:^{12}C 50:50) as a result of oxidation of fully labelled ^{13}C GSH and unlabeled GSH. The final derivatization protocol was quantitative, as free thiols remained < LOD in all samples, and it prevented measuring biased GSH/GSSG ratios, as no mixed isotopologues were measured. Consequently, all observed glutathione oxidation could be attributed to the hydrogen peroxide treatment and was not related to abiotic artefacts from

the sample preparation and handling. While oxidized glutathione (GSSG) was below LOD (< 10 pmol) in all eight control samples, the hydrogen peroxide treated samples contained approximately 1 nmol GSSG each.

Eight biological replicates were investigated following exposure to 500 µM hydrogen peroxide for 2 h. The data were evaluated in a targeted manner. Exploratory statistical analysis of the absolute amounts of 100 unique compounds using principal component analysis and hierarchical clustering clearly distinguishes within the sample groups (Fig. 3). The first principal component (39.2% explained variance) separates according to treatment, while in the heatmap all the samples are assigned to their respective cluster. Despite the short incubation time, hydrogen peroxide treatment led to strong changes, as a *t*-test with an adjusted *p*-value cutoff below 0.05 resulted in 51 unique significantly altered metabolites (Table 1), from which 30 increased and 21 decreased in their absolute concentrations, including several amino acids, nucleotides, organic acids and carbohydrates or related compounds.

In order to further investigate these changes, we constructed a metabolic network with MetExplore[38,39], mapped the significantly changed metabolites on it and extracted the subnetwork based on the mapping to create a concise, global view of the underlying phenotype upon the short redox stress induced by the hydrogen peroxide treatment. The resulting metabolic network (Fig. 4) displayed strong and consistent changes throughout the citric acid cycle (TCA), glycolysis/gluconeogenesis, glutathione metabolism, cysteine and methionine metabolism, nucleotide synthesis (purine metabolism) and pentose phosphate pathway. Here we show that many of the changes are biochemically close to each other, and only a few possible enzymatic reactions apart. Indeed, the distinct perturbed pathways exhibit a globally coordinated metabolic effort to maintain redox and energy homeostasis and restore cellular damage, as we will discuss below.

Discussion

Currently, correlative multimodal imaging –omics methods are emerging[40–43]. These include scientific questions for which untargeted analysis can take advantage of high spatial resolution, or when fast kinetic responses are involved, which can be described uniquely by live cell imaging [44,45] In this work, correlative imaging was established, integrating mass spectrometry-based metabolomics as an endpoint in live cell imaging experiments on cancer cells. Live cell imaging enables superb spatial resolution and even more importantly, to follow responses under live physiological conditions, which perfectly match the functional readout provided by metabolome analysis. The workflow was applied to study the impact of ROS on metabolism, accompanied by changes in cellular morphology and mitochondrial networks. Oxidative stress, the disturbance of oxidant-antioxidant balance favoring oxidizing environment is largely mediated by a few representative radical molecules. Mitochondria are the main ROS-active cellular sites, mainly due to electron leakage from complexes I or III, resulting in superoxide production, using a large fraction of cellular antioxidant capacity[46]. Under physiological conditions, low levels of ROS are used for cellular signaling and for regulating mitochondrial homeostasis and cellular respiration. We used hallmarks and established notions about oxidative stress response[3,6] upon hydrogen peroxide exposure with the aim of proving recurring patterns and phenomena in our data generated by the combined imaging –omics method. Perturbation of cancer cells by hydrogen peroxide was selected as a poster case. Although the applied hydrogen peroxide is moderately reactive, it can diffuse into cells or mitochondria through membranes via aquaporins with peroxiporin activity[47] and generate the highly reactive and toxic hydroxyl radical and superoxide, thereby leading to pathological effects and mutation accumulation.

Pioneering reports on the role of mitochondria in oxidative stress response date back to the last century. Mitochondria are known to handle the extramitochondrial oxidants to a large extent[48,] thereby tuning the mitochondrial metabolism[49], in particular glycolysis and oxidative phosphorylation[50]. Furthermore, DNA repair mechanisms[51] and apoptosis are induced by exogenous[52,53] and endogenous[54] hydrogen peroxide and the interplay of calcium fluxes. Oxidative stress and different forms of cellular death[55–57] have been extensively studied and summarized in exquisite reviews[58,59]. Regarding adaptive metabolism, seminal studies reported on the relevance of NADPH[60,61,] glutathione[62,63] and amino acid metabolism[64]. Nrf2 and phase II detoxification were found to have a major role in antioxidant response. Transcriptional regulation[65] such as NF-kB[66] and antioxidant enzyme levels[67] were reported.

In our study, already a short-term exposure to hydrogen peroxide resulted in significantly changed morphology and a perturbed metabolism. More specifically, the external hydrogen peroxide treatment did not uniformly affect all organelles within the cells but primarily affected the mitochondria. Although we introduced H_2O_2 to the cell culture medium and only applied a short 2 h incubation, hydrogen peroxide was able to diffuse into the cells and exert its effects, as clearly indicated by both the imaging and metabolomics. A striking result from our investigations is the high and strongly localized MitoSOX to MitoTracker ratio, indicating specific activation of the organelle. We see this despite the exogenous ROS source and the need for diffusion through the cytosol to the mitochondria. A possible explanation for this is that although the exogenous ROS affect the whole cell systematically, the primary effect is the exhaustion of antioxidant capacity, which manifests itself at the mitochondrial site, where the cell is unable to compensate for electron leakage from the ETC. This possible explanation is further supported by the morphological and network analysis of mitochondria. Multi-parametric image analysis revealed a significant reduction of the average and maximal mitochondrial length (Fig. 2), suggesting an imbalance of the fusion/fission equilibrium from mitochondrial network toward single organelles. Mitochondrial fragmentation (fission) represents the first step towards mitophagy and mitochondrial turnover, which is particularly relevant in the stress response to increased oxidative stress[68]. The finding of rapid adaptation to redox stress, as reflected in significant changes at different levels already after short-term exposure, is in accordance with previous studies. Intestinal cells were found to be able to translocate Nrf2 into the nucleus upon oxidative stress or mechanical stimulation within one hour[18], thus demonstrating that, if required, the oxidative stress response machinery can be activated quite promptly. Similarly, HT-29 colon adenocarcinoma cells can respond to oxidative stress

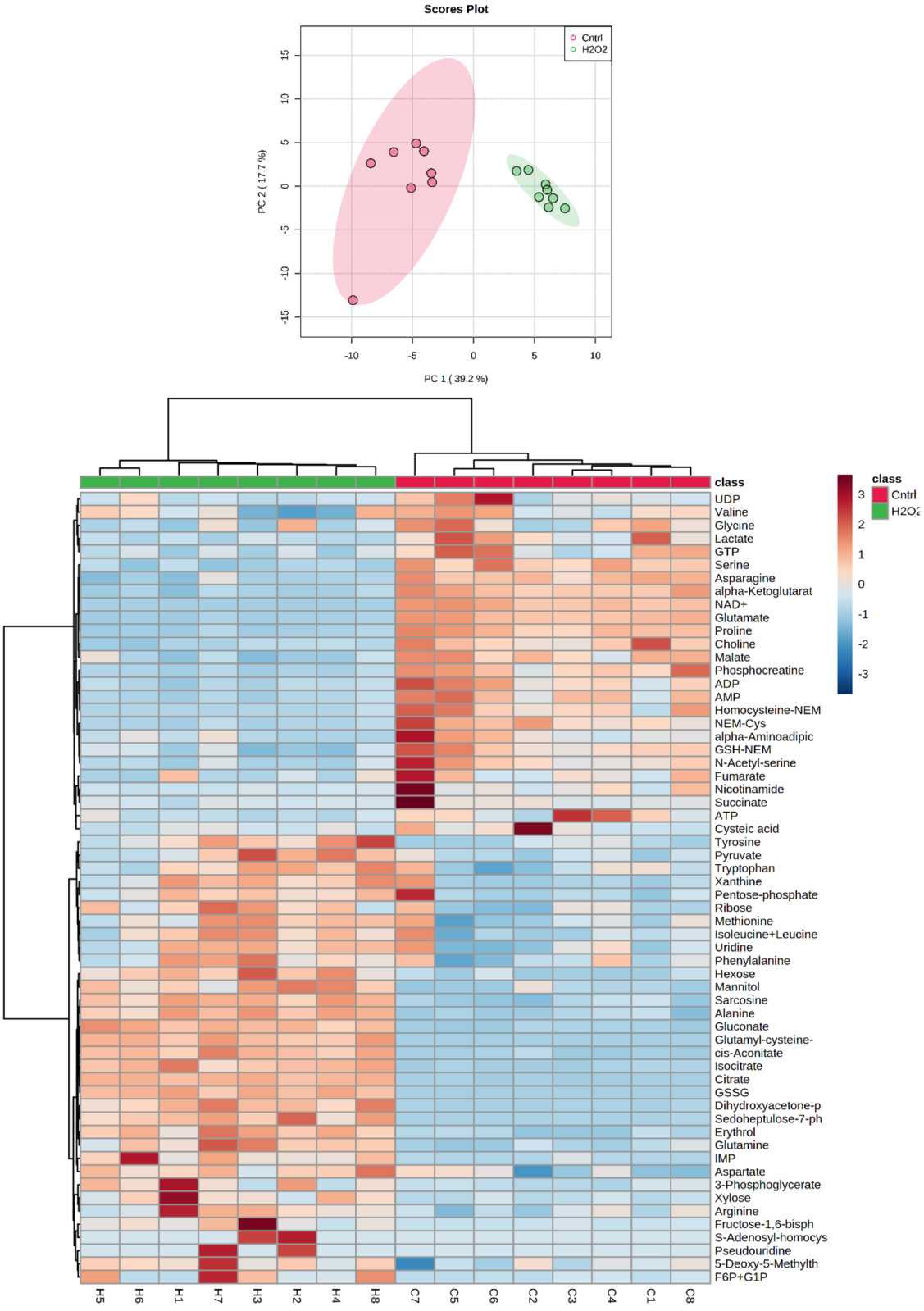

Figure 3. Principal component analysis and heatmap with hierarchical clustering of metabolomics data with 100 absolutely quantified compounds of 500 µM H_2O_2-treated samples and controls. The heatmap was constructed with top 60 features based on analysis of variance (ANOVA t-test).

Metabolite	Direction[a]	p-value (adjusted)[b]
Amino acids and derivatives		
Glutathione (oxidized)	UP	7.98E−11
Glutamyl-cysteine	UP	9.03E−10
Tyrosine	UP	7.89E−03
Glutamine	UP	4.07E−04
Alanine	UP	3.38E−07
Sarcosine	UP	3.29E−07
Arginine	UP	3.38E−02
Methionine	UP	4.83E−02
Aspartate	UP	1.14E−02
Histidine	UP	3.80E−02
Phenylalanine	UP	2.19E−02
Isoleucine–leucine	UP	1.55E−02
Tryptophan	UP	2.62E−02
Glutathione (reduced)	DOWN	1.06E−03
Asparagine	DOWN	1.58E−06
N-Acetyl-serine	DOWN	3.27E−03
Cysteine	DOWN	1.71E−04
Proline	DOWN	3.33E−08
Glutamate	DOWN	9.03E−10
Alpha-aminoadipic acid	DOWN	4.22E−02
Serine	DOWN	3.54E−06
Phosphocreatine	DOWN	3.79E−05
Homocysteine	DOWN	8.03E−04
Organic acids		
Isocitrate	UP	6.73E−08
Citrate	UP	5.74E−14
3-Phosphoglycerate	UP	3.38E−02
cis-Aconitate	UP	2.04E−08
Pyruvate	UP	2.45E−02
Malate	DOWN	1.40E−04
Alpha-ketoglutarate	DOWN	7.11E−08
Lactate	DOWN	6.47E−03
Carbohydrates and related compounds		
Sedoheptulose-7-phosphate	UP	4.94E−06
Dihydroxyacetone-phosphate	UP	2.99E−06
Xylose	UP	2.51E−02
Hexose	UP	1.32E−04
Mannitol	UP	1.49E−04
Gluconate	UP	1.55E−09
Erythrol	UP	4.01E−06
Ribose	UP	2.81E−02
Purines and pyrimidines		
IMP	UP	3.71E−03
Inosine	UP	2.45E−02
Xanthine	UP	2.02E−02
5-Deoxy-5-methylthioadenosine	UP	2.98E−02
Nicotinamide	DOWN	1.63E−02
AMP	DOWN	1.57E−04
ADP	DOWN	8.90E−04
GTP	DOWN	2.02E−02
ATP	DOWN	3.38E−02
NAD+	DOWN	1.69E−09
Amines		
Betaine	DOWN	3.96E−02
Choline	DOWN	1.32E−04

Table 1. Significantly altered metabolites upon hydrogen peroxide treatment. After 2 h incubation in HCT116 adenocarcinoma cell culture (N = 8, N = 8), 51 unique metabolites changed, from which 30 had higher (UP) and 21 lower (DOWN) concentration in means relative to control. [a]Direction of change in mean relative to control. [b]False discovery rate adjusted p-value with N = 8 biological replicates.

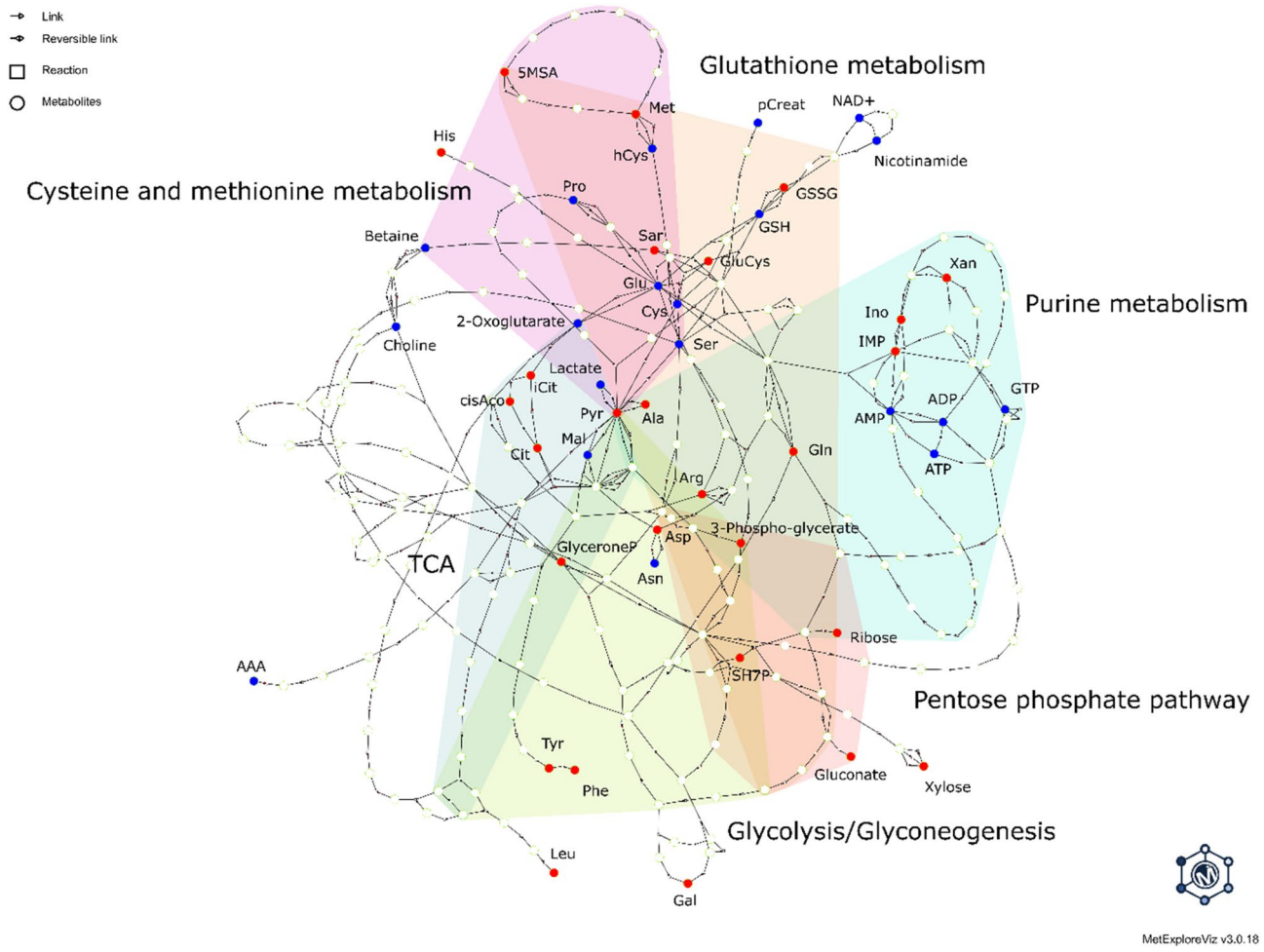

Figure 4. Sub-network constructed from the metabolic network of all possible KEGG reactions, corresponding to the union of all lightest paths between each pair of metabolites in the metabolic fingerprint of redox stress triggered by H_2O_2. Metabolites depicted as red nodes correspond to increasing amounts, while as blue nodes to decreasing amounts. Six major distinct pathways where the modulations by redox stress are found are highlighted by different colors. AAA: alpha-Aminoadipic acid, ADP: Adenosine diphosphate, Ala: Alanine, AMP: Adenosine monophosphate, Arg: Arginine, Asp: Aspartate, ATP: Adenosine triphosphate, Cit: Citrate, cisAco: cis-Aconitate, GluCys: gamma-Glutamyl-cysteine, Gln: Glutamine, Glu: Glutamate, GSH: Glutathione (reduced), GSSG: Glutathione (oxidized), His: Histidine, iCit: Isocitrate, IMP: Inosine monophosphate, Leu: Leucine, Mal: Malate, Met: Methionine, 5MSA: 5-Deoxy-5-Methylthioadenosine, NAD+: Nicotinamide adenine dinucleotide, Phe: Phenylalanine, pCreat: Phosphocreatine, Tyr: Tyrosine, SH7P: Sedoheptulose-7-phosphate, Sar: Sarcosine, Ser: Serine, Xan: Xanthine.

challenge within one hour from the stimulation and are able to up-regulate the pentose phosphate pathway (PPP), as well as to modulate glycolysis and the TCA cycle[69]. Furthermore, human skin cells also activate PPP and recycle glycolytic intermediates to maximize NADPH production even in response to ultra-short exposure to redox stress within seconds[70].

Also in this work, the structure of mitochondria was in agreement with the metabolic readout, with increased fragmentation of the mitochondrial network (Fig. 2). A significant decrease in GTP concentrations was observed, which aligns well with changes in the mitochondrial network, considering the dependence on local GTP concentrations, as three GTPases facilitate the fusion and division of mitochondrial membranes. Indeed, it was previously described that the fusion-fission equilibrium mirrors metabolic status: the ramified network (fused form) being prevalent during cell respiration and ATP production[71], and increased clustering was related to a decrease in OXPHOS efficiency[33]. Indeed, several lines of experimental evidence imply mutual regulation between cellular energetic status and mitochondrial fusion/fission equilibrium[68], making it even more important to monitor metabolic and morphologic adaptation in parallel.

Cancer cells exhibit lower levels of respiration in favor of aerobic glycolysis as well as remarkable metabolic plasticity in comparison with normal tissue. Despite this, it was previously reported, that the investigated colon carcinoma cell line HCT116 generates about 60% of its total ATP via OXPHOS[72,73]. Therefore, there is still a substantial margin for OXPHOS disruption upon mitochondrial impairment. Correspondingly, the cellular energy charge decreased upon treatment by 60% in our findings. Interestingly, phosphocreatine concentrations

were also substantially lowered, which can help to regenerate ATP during buffer fluctuations and maintain cellular energy homeostasis[74]. This seems plausible, as the synthesis of reduced glutathione is energy expensive and requires two ATP-dependent reactions.

Apart from adenosine nucleotides, multiple other purine and pyrimidine nucleotides have altered concentrations. Damage upon ROS exposure can induce DNA repair mechanisms and de novo nucleotide synthesis[75,76], and redox stress primarily damages the mitochondrial DNA over nuclear DNA[77].

The metabolic signature of antioxidant defense was accurately measured. It is also important to note that, in case of such a short-term response, cells primarily rely on the basal expression of ROS scavenging enzymes (catalases, superoxide dismutase, glutathione peroxidase and reductase, etc.) and small molecule antioxidants like reduced glutathione, until transcriptional regulation can be adapted[78]. Not only altered GSH/GSSG ratios (reduced glutathione pools due to H_2O_2 treatment, and an increase of GSSG), but also multiple changes throughout the glutathione-synthesis pathway indicate a systematic response. Beyond the first-line response of building the GSSG dimer from its reduced monomer and using its reducing power, cells started to replenish the depleted GSH pools. Changes could be observed in several differentially regulated GSH precursors such as cysteine, glutamyl-cysteine, homocysteine, glutamate. These findings were also in perfect agreement with the live cell imaging analysis of the mitochondrial superoxide (Fig. 1). Additionally, the closely related cysteine and methionine metabolism was widely perturbed.

Regarding NADPH/NADP and NAD/NAD ratios, key indicators of the cellular energy state were not considered in this work, as tailored sample preparation is needed for their accurate analysis[79]. However, the indirect effects on pathways were monitored. Upon further redox stress, there is a high NADPH demand for restoration of the reducing capacity of several enzymes in antioxidant defense (co-factor of glutathione reductase, catalase). To prioritize NADPH synthesis, glycolytic flux is diverted into the oxidative branch of the pentose phosphate pathway[75,76], and glycolytic intermediates from the non-oxidative phase of PPP can be recycled via gluconeogenesis[80–82]. Our results are in agreement with such a coordinated interplay as we see strong, consistent changes throughout these pathways. Increased amounts of glycolytic metabolites could also support the energy needs for glutathione synthesis. The other major NADPH producer apart from PPP is malic enzyme[83,84], which seems to be also involved, as its reaction partners malate and pyruvate are significantly altered as well.

Diminishing NAD+ concentration can introduce a bottleneck in the conversion of isocitrate to alpha-ketoglutaric acid, thereby stalling upstream metabolites in the TCA cycle and increasing citrate, cis-aconitate and isocitrate concentrations, which is exactly what we observed in the experiment. Furthermore, the results correspond well regarding oxidative inhibition and regulation of TCA enzymes due to high mitochondrial redox stress levels[49,85]. The reduced rate of oxidative phosphorylation (which manifests itself by the increased AMP to ATP ratio) is a response to minimize the endogenous ROS generation, as has been presented and discussed in previous works[70,86,87]. Mitochondria play a pivotal role in cellular fate. Preserving cellular physiology demands tight control of mitochondrial fusion and fission, which are key regulating processes of morphology. There is broad evidence that the morphology and bioenergetic status of mitochondria are linked[88]. The cellular energy status is given by the intracellular nucleotide pool and ATP production. The energy metabolism is in turn connected to the cellular reactive oxygen species (ROS) homeostasis, working on a delicate equilibrium between ROS and the cellular antioxidant system. The advancements in understanding reciprocal, responsive processes of morphological regulation and cellular bioenergetics status emphasized the need for methods allowing to dissect these intertwined processes also with regard to the redox status.

Here we demonstrate that precise metabolomics data relying on internal standardization and absolute quantities combined with live cell imaging are suitable for in-depth investigation of complex biological processes like short-term oxidative stress. As all the molecular signature, spatial information and morphology highlight the implication of mitochondria, we hold that this approach is a viable alternative to workflows with selective mitochondrial extraction. Cellular compartment-specific metabolomics is challenging and so far it only rarely solved problems. Conventional organelle fractionation techniques followed by extraction and LC–MS based measurements are known to introduce significant biases, as lengthy times between isolation and extraction hamper rapid quenching of metabolism. Chen et al.[25] introduced a superb solution for rapid mitochondrial isolation. Their workflow allowed to obtain metabolic profiles of mitochondria, however, as a drawback it relied on the use of genetically modified in vitro models. While our approach cannot pinpoint the cellular compartment for metabolome perturbations, we mutually validated the functional and quantitative information about the cellular state by the orthogonal information of live cell imaging and accurate absolute metabolite quantities. Overall, we were able to recapitulate established notions previously described in regard to oxidative stress in the metabolism, cellular state and morphology, as well as demonstrate the correlation between these effects. Furthermore, without the need to use an epitope-tag, the methodology can easily be extended to any adherent cell line, avoiding at the same time possible negative implications (e.g. interference with the folding of the target protein and biological activity) introduced by the tag.

Materials and methods

Methanol and water were LC–MS-grade from Fisher Scientific or Sigma Aldrich; ammonium formate, ammonium bicarbonate eluent additives for LC–MS, hydrogen peroxide (H_2O_2) and N-ethylmaleimide (NEM) were purchased from Sigma Aldrich.

Material and methods metabolomics experiment. *Cell culture.* The human colon carcinoma cell line HCT116 was kindly provided by Brigitte Marian, Institute of Cancer Research, Department of Medicine I, Medical University of Vienna. HCT116 cells were cultured as adherent monolayers in 75 cm^2 flasks (StarLab), McCoy's 5a medium (Sigma-Aldrich) was used supplemented with 4 mM L-glutamine and 10% fetal calf serum

(FCS) (BioWest) without antibiotics at 37 °C under a humidified atmosphere containing 5% CO_2. Cell culture media and reagents were obtained from Sigma-Aldrich, and all plastic dishes, plates and flasks were from Star-Lab unless stated otherwise.

Experiment: seeding, treatment and extraction. Conditions in the metabolomics and imaging cultivation plates were matched in regard to seeded cell density and available growth medium. For metabolomics 250×10^3 HCT116 cells per well were seeded (N = 8) in a 12-wellplate format (12-well CytoOne, TC-Treated) in 1 mL of McCoy's 5a medium (Sigma-Aldrich) supplemented with 10% fetal calf serum (FCS) (BioWest) and 4 mM L-glutamine without antibiotics and incubated at 37 °C (StarLab) under a humidified atmosphere containing 5% CO_2. At the same time for live cell imaging 70×10^3 cells and 291 µL medium per well were seeded into the imaging wells (Ibidi), in order to match the surface area ratio of the metabolomics well and imaging well (3.5 cm^2 vs 1 cm^2). This way we intended to achieve a similar degree of confluence at the day of the experiment.

Two days following seeding, cells were still subconfluent. First, the medium was removed, wells were washed with pre-warmed PBS (37 °C) and 500 µM hydrogen peroxide in live cell imaging solution were added, while for controls live cell imaging solution only (also 37 °C pre-warmed) was added. After incubation for 2 h, imaging and metabolomics wells were treated and prepared for measurement simultaneously..

Extraction of metabolites. We applied a combination of cold methanol extraction with NEM-derivatization: the extraction solvent consisted of 80% methanol (Fisher Scientific) and 20% aqueous 10 mM ammonium formate adjusted to pH 7 containing 25 mM N-ethylmaleimide (NEM) in order to form NEM-adducts of primary thiols[89]. The extraction solvent was prepared freshly prior to the experiment. Weighed in from NEM powder, dissolved in 10 mM ammonium formate with pH adjusted to 7.0 The solution was mixed with methanol and cooled down at − 20 °C.

Cells were washed three times with phosphate-buffered saline (PBS) (Sigma-Aldrich) (37 °C) and snap-frozen with liquid nitrogen. 20 µL fully ^{13}C labeled ($U^{13}C$) internal standard from ISOtopic solutions e.U. (dissolved in 5 mL 10 mM NH_4FA at pH 7) was added as well as 180 µL extraction solvent consisting of 20% 25 mM NEM in 10 mM NH_4FA and 80% methanol). Cells were scraped off in the extraction solution and transferred to Eppendorf tubes as described elsewhere[90]. During extraction, the samples were kept on ice. Subsequently, samples were vortexed and centrifuged (14,000 rcf, 10 min, 4 °C) and from each sample 100 µL of supernatant was transferred into a corresponding MS-vial and 50 µL extract was used to collect a pooled quality control sample. Samples were measured directly without evaporation.

The applied LC-HRMS method was adopted from[35] as described in[91]. In short, a SeQuant ZIC-pHILIC column (150 × 2.1 mm, 5 µm, polymer, Merck Millipore) with a 15-min long gradient under alkaline conditions with eluents 10 mM ammonium bicarbonate, pH 9.2/10% acetonitrile and 100% acetonitrile were used. The measurement sequence was randomized, blank and pooled quality control samples were injected at regular intervals. The high-resolution mass spectrometer Thermo Scientific™ Q Exactive HF™ quadrupole-high field Orbitrap mass spectrometer was being operated in positive/negative ion-switching mode. External calibration with 133 compounds involving $U^{13}C$ internal standardization was carried out.

Metabolomics data analysis. Targeted analysis of the data was performed with Skyline 20.2 (MacCoss Lab Software), by extracting the $[M-H]^-$ and $[M+H]^+$ ions with 5 ppm mass tolerance.

Exploratory data analysis was performed with MetaboAnalyst 5.0[92]. Missing values were imputed by 1/5 of the minimum value of the corresponding variable. For multivariate statistical methods the data were auto-scaled. The metabolic network was constructed with MetExplore[38,39] with *Homo sapiens* (Strain: Global) (Source: KEGG Map, Version: 24/04/2015) selected as BioSource[93,94]. From the 51 significantly changed metabolites (adjusted *p*-value cut-off 0.05, group variance: equal), 48 metabolites were mapped on KEGG, as mannitol, erythrol and N-acetyl-serine could not be retrieved. Following this, a subnetwork was extracted based on the mapping of significant metabolites.

Material and methods imaging experiments. *Evaluation of mitochondrial superoxide production and morphology.* In parallel to metabolome analysis, cells were incubated for live cell imaging experiments. Reference measurements of mitochondrial superoxide production and morphometric analysis were performed via imaging workflows to accurately monitor cell status with an independent experimental set-up.

Mitochondrial morphology was visualized with MitoTracker dye and mitochondrial superoxide production with MitoSox dye (both from Thermo Fisher Scientific), as previously described[18,31]. For the imaging, we removed the cell culture medium and incubated the cells with staining solutions (1:1000 dilution in Live Cell Imaging solution, Thermo Fisher Scientific) for 15 min. At the end of the staining, cells were rinsed twice with pre-warmed PBS and immediately imaged in Live Cell Imaging solution.

For microscopy acquisition, we used a confocal Zeiss microscope 710\ELYRA system PS.1 equipped with Plan-Apochromat 63×/1.2 water objective for live cell imaging and an Andor iXon 897 (EMCCD) camera. To this aim, ROI (regions of interest) were randomly selected from the MitoTracker images. During this step, the MitoSox channel was temporarily disabled to avoid selection bias. Multiparametric morphological evaluation of the mitochondrial network was performed according to the method of Valente et al.[34]. Data resulted from the quantification of at least three different optical fields/30 ROIs for every experimental condition.

Data availability

Metabolomics data (LC high-resolution mass spectrometry-based metabolomics dataset in rawdata have been deposited to the EMBL-EBI MetaboLights database (Haug et al., 2020) with the identifier MTBLS2672. The

complete dataset can be accessed here http://www.ebi.ac.uk/metabolights/MTBLS2672. The processed metabolomics data with absolute concentration, the morphological analysis and constructed subnetwork is provided in the supplementary material. Further information about the datasets generated during and/or analyzed during the study are available on request from the corresponding author G.K. (gunda.koellensperger@univie.ac.at).

Received: 8 April 2021; Accepted: 16 June 2021
Published online: 29 July 2021

References

1. Almeida, N. *et al.* Stimulation of cell invasion by the Golgi ion channel GAAP/TMBIM4 via an H_2O_2-dependent mechanism. *Redox Biol.* **28**, 101361 (2020).
2. D'Andrea, P., Romanello, M., Bicego, M., Steinberg, T. H. & Tell, G. H_2O_2 modulates purinergic-dependent calcium signalling in osteoblast-like cells. *Cell Calcium* **43**, 457–468 (2008).
3. Espinosa-Diez, C. *et al.* Antioxidant responses and cellular adjustments to oxidative stress. *Redox Biol.* **6**, 183–197 (2015).
4. Gerner, M. C. *et al.* The TGF-b/SOX4 axis and ROS-driven autophagy co-mediate CD39 expression in regulatory T-cells. *FASEB J.* **34**, 8367–8384 (2020).
5. Sciancalepore, M. *et al.* Reactive oxygen species contribute to the promotion of the ATP-mediated proliferation of mouse skeletal myoblasts. *Free Radic. Biol. Med.* **53**, 1392–1398 (2012).
6. Sies, H., Berndt, C. & Jones, D. P. Oxidative stress. *Annu. Rev. Biochem.* **86**, 715–748 (2017).
7. Aggarwal, V. *et al.* Role of reactive oxygen species in cancer progression: Molecular mechanisms and recent advancements. *Biomolecules* **9**, 735 (2019).
8. Sabharwal, S. S. & Schumacker, P. T. Mitochondrial ROS in cancer: Initiators, amplifiers or an Achilles' heel?. *Nat. Rev. Cancer* **14**, 709–721 (2014).
9. Tafani, M. *et al.* The interplay of reactive oxygen species, hypoxia, inflammation, and sirtuins in cancer initiation and progression. *Oxid. Med. Cell Longev.* **2016**, 3907147 (2016).
10. Jungwirth, U. *et al.* Anticancer activity of metal complexes: Involvement of redox processes. *Antioxid. Redox Signal.* **15**, 1085–1127 (2011).
11. Panieri, E. & Santoro, M. M. ROS homeostasis and metabolism: A dangerous liason in cancer cells. *Cell Death Dis.* **7**, e2253 (2016).
12. Trachootham, D., Alexandre, J. & Huang, P. Targeting cancer cells by ROS-mediated mechanisms: A radical therapeutic approach?. *Nat. Rev. Drug Discov.* https://doi.org/10.1038/nrd2803 (2009).
13. Chen, X. & Cubillos-Ruiz, J. R. Endoplasmic reticulum stress signals in the tumour and its microenvironment. *Nat. Rev. Cancer* https://doi.org/10.1038/s41568-020-00312-2 (2020).
14. Graf, N. & Lippard, S. J. Redox activation of metal-based prodrugs as a strategy for drug delivery. *Adv. Drug Deliv. Rev.* **64**, 993–1004 (2012).
15. Chen, H.-M., Lee, Y.-H. & Wang, Y.-J. ROS-triggered signaling pathways involved in the cytotoxicity and tumor promotion effects of pentachlorophenol and tetrachlorohydroquinone. *Chem. Res. Toxicol.* **28**, 339–350 (2015).
16. Henkler, F., Brinkmann, J. & Luch, A. The role of oxidative stress in carcinogenesis induced by metals and xenobiotics. *Cancers* **2**, 376–396 (2010).
17. Dai, C. *et al.* T-2 toxin neurotoxicity: Role of oxidative stress and mitochondrial dysfunction. *Arch. Toxicol.* **93**, 3041–3056 (2019).
18. Del Favero, G., Zaharescu, R. & Marko, D. Functional impairment triggered by altertoxin II (ATXII) in intestinal cells in vitro: Cross-talk between cytotoxicity and mechanotransduction. *Arch. Toxicol.* **92**, 3535–3547 (2018).
19. Zhang, S. *et al.* Identification of the molecular basis of doxorubicin-induced cardiotoxicity. *Nat. Med.* **18**, 1639–1642 (2012).
20. Filomeni, G., De Zio, D. & Cecconi, F. Oxidative stress and autophagy: The clash between damage and metabolic needs. *Cell Death Differ.* **22**, 377–388 (2015).
21. Fulda, S., Gorman, A. M., Hori, O. & Samali, A. Cellular stress responses: Cell survival and cell death. *Int. J. Cell Biol.* **2010**, e214074 (2010).
22. Navarro-Yepes, J. *et al.* Oxidative stress, redox signaling, and autophagy: Cell death versus survival. *Antioxid. Redox Signal.* **21**, 66–85 (2014).
23. Fiehn, O. Metabolomics—The link between genotypes and phenotypes. *Plant Mol. Biol.* **48**, 155–171 (2002).
24. Dong, Y., Digman, M. A. & Brewer, G. J. Age- and AD-related redox state of NADH in subcellular compartments by fluorescence lifetime imaging microscopy. *GeroScience* **41**, 51–67 (2019).
25. Chen, W. W., Freinkman, E., Wang, T., Birsoy, K. & Sabatini, D. M. Absolute quantification of matrix metabolites reveals the dynamics of mitochondrial metabolism. *Cell* **166**, 1324-1337.e11 (2016).
26. Van Der Kraak, L. *et al.* 5-Fluorouracil upregulates cell surface B7–H1 (PD-L1) expression in gastrointestinal cancers. *J. Immunother. Cancer* **4**, 65 (2016).
27. Kukcinaviciute, E. *et al.* Significance of Notch and Wnt signaling for chemoresistance of colorectal cancer cells HCT116. *J. Cell. Biochem.* **119**, 5913–5920 (2018).
28. Kreutz, D. *et al.* Response profiling using shotgun proteomics enables global metallodrug mechanisms of action to be established. *Chemistry* **23**, 1881–1890 (2017).
29. Enkhbat, T. *et al.* Epigallocatechin-3-gallate enhances radiation sensitivity in colorectal cancer cells through Nrf2 activation and autophagy. *Anticancer Res.* **38**, 6247–6252 (2018).
30. Dermani, F. K. *et al.* Resveratrol inhibits proliferation, invasion, and epithelial-mesenchymal transition by increasing miR-200c expression in HCT-116 colorectal cancer cells. *J. Cell. Biochem.* **118**, 1547–1555 (2017).
31. Del Favero, G., Hohenbichler, J., Mayer, R. M., Rychlik, M. & Marko, D. Mycotoxin altertoxin II induces lipid peroxidation connecting mitochondrial stress response to NF-κB inhibition in THP-1 macrophages. *Chem. Res. Toxicol.* **33**, 492–504 (2020).
32. Patten, D. A. *et al.* Altered mitochondrial fusion drives defensive glutathione synthesis in cells able to switch to glycolytic ATP production. *Biochim. Biophys. Acta Mol. Cell Res.* **1868**, 118854 (2021).
33. Wakim, J. *et al.* CLUH couples mitochondrial distribution to the energetic and metabolic status. *J. Cell. Sci.* **130**, 1940–1951 (2017).
34. Valente, A. J., Maddalena, L. A., Robb, E. L., Moradi, F. & Stuart, J. A. A simple ImageJ macro tool for analyzing mitochondrial network morphology in mammalian cell culture. *Acta Histochem.* **119**, 315–326 (2017).
35. Schwaiger, M. *et al.* Merging metabolomics and lipidomics into one analytical run. *Analyst* **144**, 220–229 (2018).
36. Sutton, T. R. *et al.* A robust and versatile mass spectrometry platform for comprehensive assessment of the thiol redox metabolome. *Redox Biol.* **16**, 359–380 (2018).
37. Haberhauer-Troyer, C. *et al.* Accurate quantification of the redox-sensitive GSH/GSSG ratios in the yeast Pichia pastoris by HILIC-MS/MS. *Anal. Bioanal. Chem.* **405**, 2031–2039 (2013).
38. Chazalviel, M. *et al.* MetExploreViz: Web component for interactive metabolic network visualization. *Bioinformatics* **34**, 312–313 (2018).
39. Cottret, L. *et al.* MetExplore: Collaborative edition and exploration of metabolic networks. *Nucleic Acids Res.* **46**, 495–502 (2018).

40. Gerner, M. C. *et al.* Proteome analysis reveals distinct mitochondrial functions linked to interferon response patterns in activated CD4+ and CD8+ T cells. *Front. Pharmacol.* **10**, 727 (2019).
41. Michálek, J. *et al.* Quantitative assessment of anti-cancer drug efficacy from coregistered mass spectrometry and fluorescence microscopy images of multicellular tumor spheroids. *Microsc. Microanal.* **25**, 1311–1322 (2019).
42. Miklosi, A. G., Favero, G. D., Marko, D., Harkany, T. & Lubec, G. Resolution matters: Correlating quantitative proteomics and nanoscale-precision microscopy for reconstructing synapse identity. *Proteomics* **18**, 1800139 (2018).
43. Van de Plas, R., Yang, J., Spraggins, J. & Caprioli, R. M. Image fusion of mass spectrometry and microscopy: A multimodality paradigm for molecular tissue mapping. *Nat. Methods* **12**, 366–372 (2015).
44. Chai, H. *et al.* Neural circuit-specialized astrocytes: Transcriptomic, proteomic, morphological, and functional evidence. *Neuron* **95**, 531-549.e9 (2017).
45. Miklosi, A. G. *et al.* Super-resolution microscopical localization of dopamine receptors 1 and 2 in rat hippocampal synaptosomes. *Mol. Neurobiol.* **55**, 4857–4869 (2018).
46. Handy, D. E. & Loscalzo, J. Redox regulation of mitochondrial function. *Antioxid. Redox Signal.* **16**, 1323–1367 (2012).
47. Bestetti, S. *et al.* Human aquaporin-11 guarantees efficient transport of H_2O_2 across the endoplasmic reticulum membrane. *Redox Biol.* **28**, 101326 (2020).
48. Guidot, D. M. *et al.* Mitochondrial respiration scavenges extramitochondrial superoxide anion via a nonenzymatic mechanism. *J. Clin. Investig.* **96**, 1131–1136 (1995).
49. Nulton-Persson, A. C. & Szweda, L. I. Modulation of mitochondrial function by hydrogen peroxide. *J. Biol. Chem.* **276**, 23357–23361 (2001).
50. Hyslop, P. A. *et al.* Mechanisms of oxidant-mediated cell injury. The glycolytic and mitochondrial pathways of ADP phosphorylation are major intracellular targets inactivated by hydrogen peroxide. *J. Biol. Chem.* **263**, 1665–1675 (1988).
51. Xanthoudakis, S., Miao, G., Wang, F., Pan, Y. C. & Curran, T. Redox activation of Fos-Jun DNA binding activity is mediated by a DNA repair enzyme. *EMBO J.* **11**, 3323–3335 (1992).
52. Gardner, A. M. *et al.* Apoptotic vs. nonapoptotic cytotoxicity induced by hydrogen peroxide. *Free Radic. Biol. Med.* **22**, 73–83 (1997).
53. Hampton, M. B. & Orrenius, S. Dual regulation of caspase activity by hydrogen peroxide: Implications for apoptosis. *FEBS Lett.* **414**, 552–556 (1997).
54. Quillet-Mary, A. *et al.* Implication of mitochondrial hydrogen peroxide generation in ceramide-induced apoptosis*. *J. Biol. Chem.* **272**, 21388–21395 (1997).
55. Clague, J. R. & Langer, G. A. The pathogenesis of free radical-induced calcium leak in cultured rat cardiomyocytes. *J. Mol. Cell. Cardiol.* **26**, 11–21 (1994).
56. Roveri, A. *et al.* Effect of hydrogen peroxide on calcium homeostasis in smooth muscle cells. *Arch. Biochem. Biophys.* **297**, 265–270 (1992).
57. Hajnóczky, G., Robb-Gaspers, L. D., Seitz, M. B. & Thomas, A. P. Decoding of cytosolic calcium oscillations in the mitochondria. *Cell* **82**, 415–424 (1995).
58. Ermak, G. & Davies, K. J. A. Calcium and oxidative stress: From cell signaling to cell death. *Mol. Immunol.* **38**, 713–721 (2002).
59. Görlach, A., Bertram, K., Hudecova, S. & Krizanova, O. Calcium and ROS: A mutual interplay. *Redox Biol.* **6**, 260–271 (2015).
60. Rescigno, M. & Perham, R. N. Structure of the NADPH-binding motif of glutathione reductase: Efficiency determined by evolution. *Biochemistry* **33**, 5721–5727 (1994).
61. Hillar, A. & Nicholls, P. A mechanism for NADPH inhibition of catalase compound II formation. *FEBS Lett.* **314**, 179–182 (1992).
62. Hwang, C., Sinskey, A. J. & Lodish, H. F. Oxidized redox state of glutathione in the endoplasmic reticulum. *Science* **257**, 1496–1502 (1992).
63. Winterbourn, C. C. & Metodiewa, D. The reaction of superoxide with reduced glutathione. *Arch. Biochem. Biophys.* **314**, 284–290 (1994).
64. Harding, H. P. *et al.* An integrated stress response regulates amino acid metabolism and resistance to oxidative stress. *Mol. Cell* **11**, 619–633 (2003).
65. Rushmore, T. H., Morton, M. R. & Pickett, C. B. The antioxidant responsive element. Activation by oxidative stress and identification of the DNA consensus sequence required for functional activity. *J. Biol. Chem.* **266**, 11632–11639 (1991).
66. Toledano, M. B. & Leonard, W. J. Modulation of transcription factor NF-kappa B binding activity by oxidation-reduction in vitro. *Proc. Natl. Acad. Sci. USA* **88**, 4328–4332 (1991).
67. Röhrdanz, E. & Kahl, R. Alterations of antioxidant enzyme expression in response to hydrogen peroxide. *Free Radic. Biol. Med.* **24**, 27–38 (1998).
68. Mishra, P. & Chan, D. C. Metabolic regulation of mitochondrial dynamics. *J. Cell Biol.* **212**, 379–387 (2016).
69. Uetaki, M., Tabata, S., Nakasuka, F., Soga, T. & Tomita, M. Metabolomic alterations in human cancer cells by vitamin C-induced oxidative stress. *Sci. Rep.* **5**, 13896 (2015).
70. Kuehne, A. *et al.* Acute activation of oxidative pentose phosphate pathway as first-line response to oxidative stress in human skin cells. *Mol. Cell* **59**, 359–371 (2015).
71. Westermann, B. Bioenergetic role of mitochondrial fusion and fission. *Biochim. Biophys. Acta Bioenergetics* **1817**, 1833–1838 (2012).
72. Ma, W., Sung, H. J., Park, J. Y., Matoba, S. & Hwang, P. M. A pivotal role for p53: Balancing aerobic respiration and glycolysis. *J. Bioenergy Biomembr.* **39**, 243–246 (2007).
73. Zheng, J. Energy metabolism of cancer: Glycolysis versus oxidative phosphorylation (Review). *Oncol. Lett.* **4**, 1151–1157 (2012).
74. Schlattner, U., Tokarska-Schlattner, M. & Wallimann, T. Mitochondrial creatine kinase in human health and disease. *Biochim. Biophys. Acta Mol. Basis Dis.* **1762**, 164–180 (2006).
75. Cooke, M. S., Evans, M. D., Dizdaroglu, M. & Lunec, J. Oxidative DNA damage: Mechanisms, mutation, and disease. *FASEB J.* **17**, 1195–1214 (2003).
76. Marnett, L. J. Oxyradicals and DNA damage. *Carcinogenesis* **21**, 361–370 (2000).
77. Yakes, F. M. & Van Houten, B. Mitochondrial DNA damage is more extensive and persists longer than nuclear DNA damage in human cells following oxidative stress. *Proc. Natl. Acad. Sci. USA* **94**, 514–519 (1997).
78. Christodoulou, D. *et al.* Reserve flux capacity in the pentose phosphate pathway by NADPH binding is conserved across kingdoms. *iScience* **19**, 1133–1144 (2019).
79. Lu, W., Wang, L., Chen, L., Hui, S. & Rabinowitz, J. D. Extraction and quantitation of nicotinamide adenine dinucleotide redox cofactors. *Antioxid. Redox Signal.* **28**, 167–179 (2017).
80. Mullarky, E. & Cantley, L. C. Diverting glycolysis to combat oxidative stress. In *Innovative Medicine: Basic Research and Development* (eds Nakao, K. *et al.*) (Springer, 2015).
81. Riganti, C., Gazzano, E., Polimeni, M., Aldieri, E. & Ghigo, D. The pentose phosphate pathway: An antioxidant defense and a crossroad in tumor cell fate. *Free Radic. Biol. Med.* **53**, 421–436 (2012).
82. Stanton, R. C. Glucose-6-phosphate dehydrogenase, NADPH, and cell survival. *IUBMB Life* **64**, 362–369 (2012).
83. Ciccarese, F. & Ciminale, V. Escaping death: Mitochondrial redox homeostasis in cancer cells. *Front. Oncol.* **7**, 117 (2017).
84. Murai, S. *et al.* Inhibition of malic enzyme 1 disrupts cellular metabolism and leads to vulnerability in cancer cells in glucose-restricted conditions. *Oncogenesis* **6**, e329–e329 (2017).

85. Chinopoulos, C., Tretter, L. & Adam-Vizi, V. Depolarization of in situ mitochondria due to hydrogen peroxide-induced oxidative stress in nerve terminals: Inhibition of α-ketoglutarate dehydrogenase. *J. Neurochem.* **73**, 220–228 (1999).
86. Stowe, D. F. & Camara, A. K. S. Mitochondrial reactive oxygen species production in excitable cells: Modulators of mitochondrial and cell function. *Antioxid. Redox Signal.* **11**, 1373–1414 (2009).
87. Tretter, L. & Adam-Vizi, V. Inhibition of krebs cycle enzymes by hydrogen peroxide: A key role of α-ketoglutarate dehydrogenase in limiting NADH production under oxidative stress. *J. Neurosci.* **20**, 8972–8979 (2000).
88. Galloway, C. A., Lee, H. & Yoon, Y. Mitochondrial morphology-emerging role in bioenergetics. *Free Radic. Biol. Med.* **53**, 2218–2228 (2012).
89. Ortmayr, K., Schwaiger, M., Hann, S. & Koellensperger, G. An integrated metabolomics workflow for the quantification of sulfur pathway intermediates employing thiol protection with N-ethyl maleimide and hydrophilic interaction liquid chromatography tandem mass spectrometry. *Analyst* **140**, 7687–7695 (2015).
90. Dettmer, K. *et al.* Metabolite extraction from adherently growing mammalian cells for metabolomics studies: Optimization of harvesting and extraction protocols. *Anal. Bioanal. Chem.* **399**, 1127–1139 (2011).
91. Oberhuber, M. *et al.* STAT3-dependent analysis reveals PDK4 as independent predictor of recurrence in prostate cancer. *Mol. Syst. Biol.* **16**, e9247 (2020).
92. Chong, J., Wishart, D. S. & Xia, J. Using MetaboAnalyst 4.0 for comprehensive and integrative metabolomics data analysis. *Curr. Protoc. Bioinform.* **68**, e86 (2019).
93. Kanehisa, M. & Goto, S. KEGG: Kyoto encyclopedia of genes and genomes. *Nucleic Acids Res.* **28**, 27–30 (2000).
94. Kanehisa, M. *et al.* Data, information, knowledge and principle: Back to metabolism in KEGG. *Nucleic Acids Res.* **42**, D199–D205 (2014).

Acknowledgements

We thank Gerrit Hermann from ISOtopic solutions e.U. for kindly providing the fully labelled ^{13}C standards. The imaging workflows were supported by the core facility Multimodal Imaging (Faculty of Chemistry, University of Vienna) member of the VLSI (Vienna Life Science Instruments). Open access funding provided by University of Vienna.

Author contributions

M.R., G.D.F., C.G. and G.K. designed the study. M.R. and G.D.F. interpreted the results. M.R. and G.D.F performed the experiments. M.R., Y.E.A., and G.D.F. analyzed the data. G.K. and B.K.K. also contributed via funding acquisition and providing resources. All authors contributed to the integration of the research, reviewed, and edited the final version of the manuscript.

Competing interests

The authors declare no competing interests.

Additional information

Supplementary Information The online version contains supplementary material available at https://doi.org/10.1038/s41598-021-94585-8.

Correspondence and requests for materials should be addressed to G.K.

Reprints and permissions information is available at www.nature.com/reprints.

Publisher's note Springer Nature remains neutral with regard to jurisdictional claims in published maps and institutional affiliations.

cancers

MDPI

Article

Thermodynamic Genome-Scale Metabolic Modeling of Metallodrug Resistance in Colorectal Cancer

Helena A. Herrmann [1,†], Mate Rusz [1,2,†], Dina Baier [2], Michael A. Jakupec [2,3], Bernhard K. Keppler [2,3], Walter Berger [3,4], Gunda Koellensperger [1,5,6,*] and Jürgen Zanghellini [1,*]

1 Department of Analytical Chemistry, University of Vienna, 1090 Vienna, Austria; helena.herrmann@univie.ac.at (H.A.H.); mate.rusz@univie.ac.at (M.R.)
2 Institute of Inorganic Chemistry, University of Vienna, 1090 Vienna, Austria; dina.baier@univie.ac.at (D.B.); michael.jakupec@univie.ac.at (M.A.J.); bernhard.keppler@univie.ac.at (B.K.K.)
3 Research Cluster Translational Cancer Therapy Research, University of Vienna and Medical University of Vienna, 1090 Vienna, Austria; walter.berger@meduniwien.ac.at
4 Institute of Cancer Research and Comprehensive Cancer Center, Medical University of Vienna, 1090 Vienna, Austria
5 Vienna Metabolomics Center (VIME), University of Vienna, 1090 Vienna, Austria
6 Research Network Chemistry Meets Microbiology, University of Vienna, 1090 Vienna, Austria
* Correspondence: gunda.koellensperger@univie.ac.at (G.K.); juergen.zanghellini@univie.ac.at (J.Z.)
† Equal contributor.

Simple Summary: Cancer, but also its treatment, can lead to a reprogramming of cellular metabolism. These changes are observable in metabolite abundances, which can be unbiasedly measured via mass spectrometry metabolomics. However, even when the metabolome changes strongly, a (mechanistic) interpretation is difficult as metabolite levels do not necessarily directly correspond to pathway activities. Here we measure the changes of the cellular metabolome in colorectal cancer cell lines sensitive and resistant to the ruthenium-based drug BOLD-100/KP1339 and the platinum-based drug oxaliplatin. We map these changes onto a cancer-specific genome-scale metabolic model, which allows us not only to compute intracellular flux distributions, but also to disentangle drug-specific effects from growth differences from differences in metabolic adaptations due to resistance. Specifically, we find that resistance to BOLD-100/KP1339 induces more extensive reprogramming than oxaliplatin, especially with respect to fatty acid and amino acid metabolism.

Abstract: Background: Mass spectrometry-based metabolomics approaches provide an immense opportunity to enhance our understanding of the mechanisms that underpin the cellular reprogramming of cancers. Accurate comparative metabolic profiling of heterogeneous conditions, however, is still a challenge. Methods: Measuring both intracellular and extracellular metabolite concentrations, we constrain four instances of a thermodynamic genome-scale metabolic model of the HCT116 colorectal carcinoma cell line to compare the metabolic flux profiles of cells that are either sensitive or resistant to ruthenium- or platinum-based treatments with BOLD-100/KP1339 and oxaliplatin, respectively. Results: Normalizing according to growth rate and normalizing resistant cells according to their respective sensitive controls, we are able to dissect metabolic responses specific to the drug and to the resistance states. We find the normalization steps to be crucial in the interpretation of the metabolomics data and show that the metabolic reprogramming in resistant cells is limited to a select number of pathways. Conclusions: Here, we elucidate the key importance of normalization steps in the interpretation of metabolomics data, allowing us to uncover drug-specific metabolic reprogramming during acquired metal-drug resistance.

Keywords: omics data integration; constraint-based modeling; data normalization

Citation: Herrmann, H.A.; Rusz, M.; Baier, D.; Jakupec, M.A.; Keppler, B.K.; Berger, W.; Koellensperger, G.; Zanghellini, J. Thermodynamic Genome-Scale Metabolic Modeling of Metallodrug Resistance in Colorectal Cancer. *Cancers* **2021**, *13*, 4130. https://doi.org/10.3390/cancers13164130

Academic Editor: Jesús García-Foncillas

Received: 24 June 2021
Accepted: 3 August 2021
Published: 17 August 2021

1. Background

A reprogramming of metabolism is a hallmark of multiple diseases, including cancer [1]. Changes in glucose, amino acid, lipid, and cholesterol metabolism, for example, have all been associated with aberrant metabolic phenotypes observed in cancers [2]. Resulting differences in metabolism between healthy and cancerous cells hold the potential for selectively targeting cancerous cells through pharmacological and dietary interventions. As such, understanding the extent to which metabolic reprogramming occurs in different cancer cells is a fundamental requirement for better treatment options. However, not only malignant transformation, but also therapy response on drug resistance acquisition might be paralleled or even driven by metabolic changes in the malignant cells [3,4]. In case of acquired therapy resistance, dissection of the respective metabolic alterations and mechanism on a larger scale are only at the beginning and have not found widespread application yet.

In silico methods have the potential to integrate existing experimental data and to generate new hypotheses about the underlying mechanisms associated with metabolic reprogramming. Genome-scale metabolic models (GSMMs), which capture the known biochemical reactions of a given system, have previously been applied in various cancer studies [5,6], such as the investigation of metabolic heterogeneity [7] and have led to the discovery of new drug targets and biomarkers [8–12]. There are, however, areas of cancer research where GSMMs have not yet been applied due to a lack of available experimental data. For example, GSMMs have not yet been used extensively to study acquired drug resistance against different drug classes in different cancer cell types. Acquired therapy resistance is considered a major obstacle for curative systemic cancer treatment at progressed stages and also affects the success of anticancer metal drugs [13–16].

Metal-based drug treatments involving oxaliplatin are a standard therapy for colorectal cancer, the third most commonly diagnosed cancer [17–20]. Drug resistance, however, has been reported to develop in nearly all patients with colorectal cancer; even when using modern targeted and immunotherapy options, chemotherapy remains a major part of the colorectal cancer treatment regimen [14,15]. Platinum-based drugs are still prescribed in different lines of systemic cancer treatment in diverse tumor types and patient cohorts [21]. Although platinum-based anticancer drugs like oxaliplatin are widely-used, intrinsic and acquired resistances remain a crucial impediment in the treatment of colorectal cancer.

Acquired resistance against platinum drugs is thought to be mainly based on elevated DNA-repair mechanisms, detoxification, evading apoptosis and autophagy [22]. However, there is an increasing amount of evidence that metabolic alterations might play a pivotal role as well [23]. The clinically-investigated ruthenium-based anticancer drug BOLD-100/KP1339 has shown promising results with regard to colorectal cancer treatment [24]. BOLD-100/KP1339 (sodium trans-[tetrachloridobis (1H-indazole) ruthenate(III)]) is a prodrug [25] displaying preferential activation by reduction in the hypoxic milieu of solid tumors and does not primarily target DNA [26] and metabolic alterations are expected to be relevant. Unlike BOLD-100/KP1339, which is still under investigation for clinical applications, oxaliplatin is an already widely-applied, clinical cancer treatment. As a result, the body of literature addressing oxaliplatin resistance is notably larger than that of BOLD-100/KP1339 resistance. Nonetheless, the extent to which metallodrug resistance results in an altered metabolic profile remains poorly understood for both drug treatments and has not yet been compared. As such, it is not yet known whether metabolic reprogramming during resistance development against anticancer compounds with differenct metal centers and activity parameters are comparable or drug-specific.

Metabolomics aims to directly measure metabolite abundance from a global and unbiased perspective and has the potential to not only detect metabolic alterations but to discover diagnostic and prognostic markers and to generate hypotheses that can be validated with genetic experiments [27]. Recent progress in targeted and untargeted metabolomics approaches have resulted in a wide-ranging toolkit for studying metabolic phenotypes in terms of cellular concentrations. Mass spectrometry-based metabolomics

approaches can be used for the metabolic profiling of drug-treatment responses in cancer cell lines [28,29].

While metabolomics studies provide an effective interrogation window for the cellular changes that occur in response to a change in conditions, they do not necessarily provide mechanistic insights into the reprogramming of metabolism. Metabolite pools do not inform about pathway activity, ergo corresponding metabolic fluxes are sometimes measured. Measuring metabolic fluxes, however, also suffers from several practical limitations. For example, a prolonged time for peripheral pathways to reach isotopic steady-state, the fact that simple linear pathways can only be investigated with non-stationary labelling or an increased number of samples, and the complex data analyses required for nonstationary labelling experiments often hinder a successful and comprehensive application of isotopic labelling methods [30].

Recent trends in metabolomics have shown it is always possible to measure more metabolites at more time points and to analyse the obtained results in combination with other 'omics data sets [31–34]. While multi-omics have allowed for the identification of numerous regulatory mechanisms in cancer [35,36], their integration with fluxomics is required to gain a holistic understanding of metabolic reprogramming. To understand the mechanisms that underpin a potential reprogramming of metabolism during resistance development, observed changes in metabolite concentrations need to be placed in the context of changes in metabolic flux. GSMMs provide a platform for doing so [37]. Multiple techniques for integrating omics data sets into GSMMs have been developed [11,38–41]. While expression data sets are often used to generate system-specific models [8,42], metabolomics and proteomics data sets are used to constrain the solution space of the generated models [38,41].

Typically, constraint-based modelling (CBM) is employed to study GSMMs and to explore metabolic phenotypes in the form of steady-state fluxes [43,44]. Flux balance analysis (FBA), for example, uses linear optimization techniques to model the fluxome of GSMMs [see Orth et al. [45] for a review]. FBA, however, can lead to the prediction of thermodynamically infeasible flux solutions. Thermodynamic flux analysis (TFA) imposes additional constraints on stoichiometric models to ensure thermodynamically valid fluxes and provides a framework for integrating metabolomics data into GSMMs [46,47]; extracellular metabolite data are used to constrain the directionality of exchange reactions of the model and intracellular metabolite data can be used to constrain reactions in the model. Both intra- and extracellular metabolite data have previously been integrated into system-specific metabolic models to draw physiological conclusions about cancerous and healthy cells [48–51].

In this work, we integrate experimentally determined absolute concentrations of intracellular metabolites and medium-based metabolites and growth rates of the colorectal cancer cell-line HCT116 into a cell-line specific, thermodynamic, genome-scale metabolic model (GSMM). We consider two different models of acquired resistance in colon cancer: oxaliplatin resistant (OxR) and BOLD-100/KP1339 resistant (RuR) HCT116 cells as well as their sensitive controls to generate four model instances. To identify metabolic differences between resistant and sensitive cells, we normalize the calculated flux values by their representative growth rates. As oxaliplatin and BOLD-100 are prepared in different solvents (water versus dimethylsulfoxid (DMSO)), OxR and RuR cells were grown in the same media, but RuR and its respective control were exposed to a low DMSO background equivalent to the drugs' stock solution solvent. To account for metabolic differences that are the results of a difference in solvent, we further normalized the results obtained for the resistant cells by their sensitive controls. Eliminating both differences in growth rate and solvent background, we are able to draw drug-specific conclusions about the metabolic changes that occur upon resistance. As a result, we are able to identify specific changes in flux that are the direct result of an acquired resistance to either oxaliplatin or BOLD-100/KP1339 treatment.

2. Materials and Methods

2.1. Cell Culture

HCT116 colon cancer cells were generously provided by Dr. Vogelstein from John Hopkins University, Baltimore. Cells were cultured in McCoy's medium (Sigma Aldrich, Burlington, MA, USA) supplemented with 10% fetal calf serum (FCS; PAA, Linz, Austria) and 2 mM glutamine (Sigma Aldrich). Cells were selected for acquired drug resistance over several months via exposure to increasing concentrations of oxaliplatin or BOLD-100/KP1339 followed by drug-free recovery phases. Finally, the oxaliplatin-resistant HCT116 (OxR) cells were selected with 5 µM of oxaliplatin [52,53] for 24 h and BOLD-100/KP1339-resistant (RuR) cells with 200 µM of BOLD-100/KP1339 for 72 h in two-week-intervals. All cultures were grown under standard cell culture conditions and checked for *Mycoplasma* contamination.

2.2. Cell Viability Assay

Cells were seeded at densities of 3.5×10^4 cells/well in 96-well microtiter plates and allowed to adhere overnight. Cells were exposed to indicated concentrations of the respective drugs for 72 h. Cell viability was determined using the 3-(4,5-dimethylthiazol-2-yl)-2,5-diphenyltetrazolium bromide (MTT) assay (EZ4U, Biomedica, Vienna, Austria) following the manufacturer's recommendations.

2.3. Metabolomics Experiment

HCT116 cells, HCT116 cells with acquired oxaliplatin resistance, and HCT116 cells with acquired BOLD-100/KP1339 resistance were seeded ($N = 6$ for each respectively) as 2×10^5 cells/well in 12-well plate format in 1 mL McCoy's medium (Sigma Aldrich) supplemented with 2 mM glutamine and 10% FCS. After overnight growth, wells were supplemented with 1 mL fresh medium each. HCT116 with acquired BOLD-100/KP1339 resistance and its sensitive control contained the same medium with 0.5% dimethyl sulfoxide (DMSO) used as BOLD-100 solvent. Twenty-four hours after supplementing with additional medium, cells were still not confluent. At this point, the medium was removed and cells were washed three times with 2 mL PBS (37 °C) and snap frozen with liquid nitrogen.

2.4. Metabolomics Sample Preparation

The samples were randomized at the stages of the experiment including seeding, sample preparation and extraction as well as LC-MS measurement sequence. Extraction and measurement of the metabolites were based on a protocol described elsewhere [54]. Briefly, the protocol comprised cell scraping and extraction with 180 µL cold 80% methanol containing 5 mM N-ethylmaleimide (dissolved in 10 mM ammonium-formate at pH 7) with 20 µL fully ^{13}C-labeled internal standard, ISOtopic solutions (Vienna, Austria). After a centrifugation step (14,000 rcf, 4 °C, 10 min) cell extracts were directly measured with high-resolution OrbiTrap mass spectrometer.

2.5. LC-MS Analysis of Metabolites

The quantification of metabolites was based on Schwaiger et al. [55] and the LC-MS gradient was adapted and shortened to suit metabolites as described elsewhere [56]. Full mass scan data was acquired both in positive and negative ion mode.

2.6. LC-MS Analysis of Coenzymes

The analysis of free coenzyme A (CoA), acetyl-coenzyme A, palmitoyl-coenzyme A, malonyl-coenzyme (A below LOD) was carried out in an additional measurement series of the same samples and on the same instrumental setup but with a dedicated LC-MS method. The same separation was used with the same gradient and eluents, but flushing of the column started at 6 min instead of 7 min, shortening the total measurement time from 15 min to 14 min. The OrbiTrap MS settings were changed with regard to the mass range

to 750–1100 m/z, the capillary temperature was lowered from 280 °C to 200 °C to reduce in-source fragmentation and the S-lense RF-level was increased from 30 to 60.

2.7. Determination of Total Protein Content

The applied extraction and centrifugation resulted in a pellet containing the high-molecular fraction and non-polar metabolites. This pellet was dissolved in 0.2 M NaOH overnight, diluted 1:10 in the same NaOH solution and determined for total protein content with the Thermo Micro BCA kit, according to manufacturer's instructions.

2.8. Data Analysis of Metabolomics Measurement

Targeted analysis of the data was done with Skyline 20.2 (available at https://skyline.ms/project/home/software/Skyline/begin.view, accessed on 12 August 2021) extracting the $[M\text{-}H]^-$ and $[M+H]^+$ ions with 5 ppm mass tolerance. The absolute concentrations relied on the external calibration with internal standardization. The compounds were standardized compound-specifically where possible and class-specifically when the $U^{13}C$ equivalent was not reliably available or by $U^{13}C$-glutamate if neither of the aforementioned were available.

Metabolites with technical repeatability (relative standard deviation) above 30% were removed from the dataset. This was based on the repeated injection and measurement of a pooled quality control sample. Furthermore, metabolites which had mean concentration below the determined lowest limit of quantification (LOQ) according to the validation of the LC-MS method described in [55] were removed.

Datasets were combined by joining the metabolite data acquired in both positive and negative mode, as well as coenzyme data in the negative acquisition mode. A further calibration was measured in positive mode for several carnitines (propionyl-carnitine, O-acetyl-carnitine, propionyl-carnitine, palmitoyl-carnitine) with the method for metabolites, since these compounds were not contained in our original calibration mixture. Also the calibration row for coenzymes was prepared freshly in this mixture to avoid degradation by storage. The external calibration of the different coenzymes (coenzyme A, acetyl coenzyme A, malonyl coenzyme A, palmitoyl coenzyme A) was measured in negative mode. For every primary thiol in the dataset (coenzyme-A, glutathione, cysteine, etc.) its N-ethyl maleimide adduct was used for quantification after it was made sure that the conversion was quantitative.

2.9. Measurement of Extracellular Metabolite Concentrations

10^5 HCT116 cells as well as HCT116 cells with acquired oxaliplatin resistance and HCT116 cells with BOLD-100/KP1339 resistance were seeded ($N = 4$ for each respectively) into 12-well plate (StarLab) with 2 mL McCoy's 5A medium (Sigma-Aldrich) containing 10% FCS (BioWest) and 4 mM glutamine. Also in the case of the sensitive HCT116 cells and the BOLD-100/KP1339-resistant cells the experiment was run with and without 0.5% DMSO. 100 µL were collected from the starting medium at the beginning of the experiment, and directly from the wells 24 h, 48 h and 72 h after seeding. Also, a cell free experiment was run to determine the contribution of abiotic glutamine decay.

2.10. Determination of Dry-Weight for the Cell Lines

The cell dry weight measurements of HCT116 sensitive (Sen), oxaliplatin-resistant (OxR) and BOLD-100/KP1339-resistant (RuR) cells were carried out ($N = 4$ for each respectively) as described by Széliová et al. [57].

2.11. HCT116-Specific Genome-Scale Metabolic Model

Robinson et al. [58] provide the latest consensus GSMM of human metabolism called Human1. The authors used Human1 to generate cell-line specific models using gene essentiality data from previous CRISPR knockout screens [59]. Using the tINIT algorithm [42] and RNA-Seq data from HCT116 colorectal carcinoma cells they select reactions from

Human1 associated with moderately and highly expressed genes to build a cell-line specific model for HCT116. We obtained the model from the authors, removed the enzyme constraints and added a further seven exchange reactions to the model to account for the excretion or uptake of cis-aconitate, fumarate, isocitrate, malate, sarcosine, succinate and xanthine that we observed in our measured time-course of the medium composition. We use this updated model for all our analyses presented here. The model is available at https://github.com/HAHerrmann/Hct116_DrugRes/blob/master/Models/Colon_Combined.xml (accessed on 12 August 2021).

Growth rates (Figure S1) and exchange rates (Figure S2) were fitted as described in Széliová et al. [60]. In short, we fitted an exponential model to estimate the initial concentration, X_0, and the growth rate, μ. The fitted growth rate and the initial biomass, B_0, were then used to calculate the specific exchange rates for all of the measured medium-based metabolites across all time points, i.e., 0, 24, 48, and 72 h. B_0 was calculated from the fitted X_0 and the experimentally determined dry mass per cell (Figure S3). The fitting was done in Python (Version 3.7.9) using the optimize function in scipy (Version 1.5.2) with parameters `soft_l1` for the loss function and `f_scale` $= 0.3$ for outlier detection. The propagated error of the growth rate measurement (Figure S1) and the dry mass per cell (Figure S3) was calculated and used to set upper and lower bounds. The obtained growth and exchange rates were used to constrain the respective import and export reactions of the model. Flux constraints were set such that the applied upper and lower bounds accounted for the relative standard error or the propagated error of the measurement. We further constrained the directionality of uptake and excretion rates of 50 metabolites, using HCT116 cell line specific data obtained by Jain et al. [61]. The "blood pool" reactions were removed from the model because we did not consider in vivo conditions. Instead, we allowed for an unconstrained influx of stearate, palmitate, oleate, linolenate, linoleate, and arachidonate. These fatty acids have previously been shown to make up the majority of lipids present in fetal calf serum [62,63] which was used as a growth medium supplement.

All applied model constraints are based on data obtained during the exponential growth phase and as such, all model results are specific to this growth phase.

2.12. Thermodynamic Metabolic Modeling

The pyTFA package [47], https://github.com/EPFL-LCSB/pytfa, accessed on 12 August 2021, formulates thermodynamic flux analysis (TFA) of GSMM as a mixed-integer linear programming problem that incorporates metabolite concentrations as thermodynamic constraints into a traditional flux balance analysis (FBA) model. Masid et al. [49] have recently constructed an extensive thermodynamic database containing the thermodynamic information for compounds, reactions and compartments in human metabolism; this includes the Gibbs free energy formation of compounds and the associated error estimation, the pH, ionic strength and membrane potentials. Using Biopython (Version 1.78) we annotated the GSMM with SEED identifiers which allowed us to match the information in the GSMM to the thermodynamic database of Masid et al. [49]. Absolute metabolite concentrations were normalized according to total protein content. Normalized values were used to constrain condition-dependent GSMM instances. Between 61 and 68 metabolites were experimentally constrained in each model instance. Where no experimental data was available, metabolite concentrations were set to the default range of 10^{-12} to 0.1 mol per total protein. This allowed us to achieve a thermodynamic coverage of 89% of the compounds and to estimate the Gibb's free energy for 20% of the reactions. Using a parsimonious FBA (pFBA) that maximizes a linear objective while minimizing the total sum of fluxes [64], we calculated the minimum total sum of fluxes and set this as an additional constraint to our linear model prior to performing a Flux Variability Analysis (FVA) on the thermodynamic model, here referred to as TFVA. TFVA applies the same constraints as TFA but instead of returning a single feasible solution, the lowest and highest possible flux value for each reaction is returned [65]. Because pFBA does not necessarily return a unique solution when two alternative pathways with the same total sum of fluxes exist, we chose

to implement a parsimonious TFVA (pTFVA) to compare different model instances to one another. Upon parallelizing the existing TFVA implementation in pyTFA for an improved run time, we ran a pTFVA for different instances of the HCT116 cell-lines specific GSMM. Flux analyses were done in Python (Version 3.7.9) using cobrapy (Version 0.19.0) [66].

2.13. Data Processing and Flux Normalization

We constrained four different instances of the HCT116 model: oxaliplatin-resistant cells (OxR) and their sensitive parental counterpart (HCT116) and BOLD-100/KP1339-resistant cells (RuR) and their sensitive parental counterpart in a DMSO-based medium (HCT116-DMSO). Model instances were constrained using the condition-specific exchange fluxes (Figure S1) and growth rate (Figure S2). All blocked reactions were removed using the `find_blocked_reactions` in cobrapy (Version 0.19.0) with default parameters, resulting in a model with 4530 reactions and 4492 degrees of freedom. Upon calculating flux values for each model instance using pTFVA as described, we divided each set of flux values by the outgoing flux to biomass production of that model instance, effectively normalizing for difference in growth. We checked for reactions for which both the upper and the lower bound differed by at least 15%. Furthermore, we feature-scaled all flux values to lie between 0 and 1 and divided the flux values obtained in the drug-resistant instances by the corresponding flux values obtained for their respective controls. Having thus normalized for differences in the medium composition, we were able to compare the flux profiles of the two metallodrug resistances to another, again checking for which reactions both the upper and lower bounds differed by at least 15%.

3. Results

3.1. Differences in Metabolite Concentrations May Not Correlate to Changes in Flux

To investigate the metabolic changes associated with metallo-resistance in colorectal cancer, we compared the metabolic profiles of resistant and sensitive cells. Using the HCT116 colorectal cancer cell line, cells with resistance to either oxaliplatin (OxR) or BOLD-100/KP1339 (RuR) were compared to their sensitive counterparts. The two acquired resistence models are largely independent of one another: while OxR cells show moderate cross-resistance for the ruthenium-based drug, RuR cells display no cross-resistance and remain sensitive to oxaliplatin treatment (Figure S5). This implies a difference in the molecular basis of resistance between the two models. OxR cells and their parental sensitive counterparts were grown in a standard medium, while RuR cells and their parental sensitive counterparts were grown in the same medium but with a low solvent-background (DMSO) as outlined in the Materials and Methods. Relative differences in the cellular metabolite concentrations of sensitive versus resistant cells highlight the extent to which the acquired metallodrug resistance results in an altered metabolome (Figure 1). We observe that some responses, such as an increase in palmitoylcarnitine and a decrease in lactate upon resistance, are shared across the two metallo-resistance phenotypes. Nevertheless, many of the metabolic changes associated with resistance are drug-specific. Pyruvate and carnitine concentrations, for example, are higher in RuR cells but lower in OxR cells when compared to their sensitive counterparts. Palmitoyl-CoA, on the other hand, is lower in RuR cells and higher in OxR cells when compared to their parental sensitive counterparts (Figure 1).

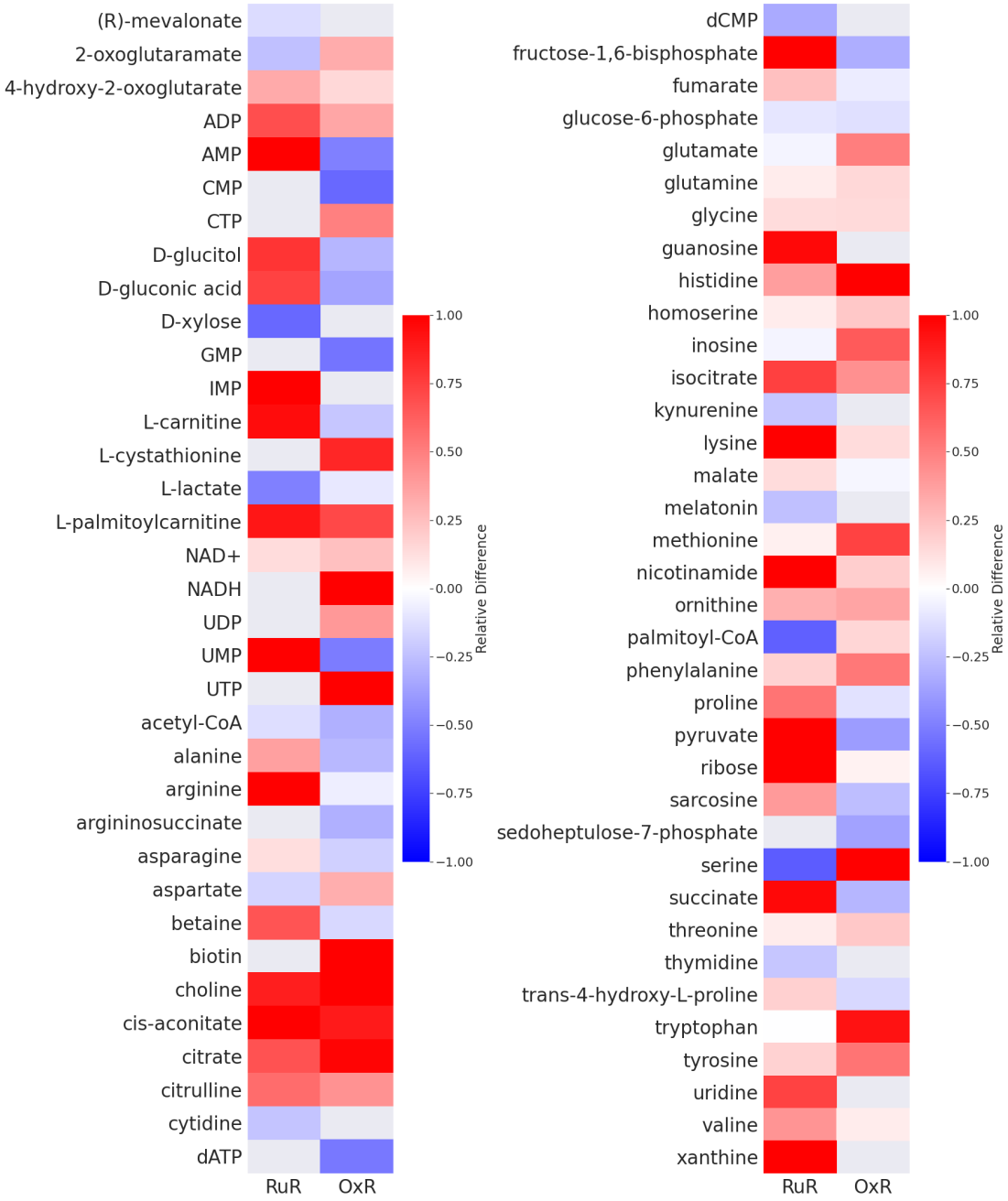

Figure 1. Observed changes in metabolite concentrations upon acquired resistance. Oxaliplatin (OxR) and BOLD-100/KP1339 (RuR) resistance models are compared to their sensitive counterparts. Relative differences in the measured metabolite concentrations of resistant and sensitive cells are shown. A positive relative difference (red) indicates a higher metabolite concentration in the resistant as compared to the parental sensitive model, whereas a negative relative difference (blue) indicates a lower metabolite concentration in the resistant than in the sensitive counterpart. Relative differences were calculated from using the mean values of six replicates. Only those metabolites for which we observed an absolute relative change greater than 15% between sensitive and resistant, in at least one of the two conditions, are shown. The following abbreviations were used: ADP—adenosine diphosphate, AMP—adenosine monophosphate, CMP—cytidine monophosphate, CTP—cytidine triphosphate, GMP—guanosine monophosphate, IMP—inosine monophosphate, NAD—nicotinamide adenine dinucleotide , UDP—uridine diphosphate, UMP—uridine monophosphate, UTP—uridine triphosphate, CoA—coenzyme A, dATP—deoxyadenosine triphosphate, dCMP—deoxycytidine monophosphate.

With the aim of investigating whether the observed changes in cellular metabolite concentrations (Figure 1) translate to changes in metabolic flux, we integrated experimen-

tally determined growth rates (Figure S1), intracellular metabolite concentrations (Figure 1) and exchange rates (Figure S2) in a genome-scale metabolic model (GSMM) of HCT116. We constrained four instances of the GSMM: an oxaliplatin-resistant (OxR) and a parental sensitive counterpart (sensitive), a BOLD-100/KP1339-resistant (RuR) and a parental sensitive counterpart for the DMSO-containing medium (sensitive-DMSO). Measuring 110 metabolite concentrations and 37 exchange fluxes, we constrained the solution space of a model with 6479 metabolites and 6716 reactions. Growth rates were used to constrain the biomass production of each model instance. Resistant cells grow slower than sensitive cells and OxR cells grow even slower than RuR cells (Figure S1). Exchange rates (Figure S2) were determined from time-course measurements of the medium composition and were applied as flux bounds on the corresponding import and export reactions of the model. Intracellular metabolite concentrations were applied as constraints using the pyTFA package [47]. Using a parsimonious thermodynamic flux variability analysis (pTFVA), as outlined in the Materials and Methods, we calculated flux solutions for each of the four model instances, each of which was constrained with the corresponding experimental data. By incorporating the growth and exchange rates as well as the intracellular metabolite concentrations into a GSMM, we were able to calculate possible changes in metabolic fluxes. Metabolic rates, rather than concentrations, could then be normalized according to the cellular growth rate observed under those conditions. We compared the four sets of flux solutions against one another, both before and after normalizing all flux values by the respective growth rate (Figure 2). Growth rate normalization was implemented by dividing all of the calculated flux values by the experimentally measured growth rate used to constrain that model instance.

The maximum relative standard error observed across the metabolite measurements was less than 15%. Thus, when integrating the data into the GSMM and comparing flux differences between condition-specific instances of the model, we used a cutoff of 15% to determine whether fluxes were significantly different across conditions. Comparing resistant cells to sensitive cells, we identify pathways with the most prominent changes in flux upon acquired resistance (Figure 2). Differences in flux observed prior to growth standardization directly correspond to predictions of in vivo fluxes. Differences in flux observed post growth standardization are no longer predictions of in vivo fluxes, but are predictions of flux differences that are assumed to be the direct result of a metabolic reprogramming upon acquired resistance rather than changes in growth rate.

Initially, the oxidative phosphorylation pathway shows the highest amount of flux changes in response to OxR. Upon growth normalizing, however, it is RuR that shows a higher number of flux changes in this pathway. Furthermore, what initially appears to be significant differences in flux through the cholesterol and lipid metabolism, largely disappears upon growth normalization. Changes in the subsystem reactive oxygen species (ROS) detoxification seem minimal prior to growth normalization; the normalized results, however, indicate significant changes in flux with regards to detoxification. While the number of reactions that appear to be affected in starch and sugar and tricarboxylic acid (TCA) metabolism appears to be drug resistance-specific prior to growth normalization, this effect disappears upon growth normalization. The comparison of non-normalized and growth-normalized results in Figure 2 emphasizes that observed changes in metabolite concentrations are not necessarily indicative of cellular changes in flux. It further highlights that flux results must be growth normalized in order to distinguish a resistance model effect from a growth effect when comparing the metabolic profiles of resistant and sensitive cells. Changes in the pentose phosphate pathway (PPP), oxidative phosphorylation, glycolysis/gluconeogenesis, TCA, nucleotide, ROS and fatty acid pathways, for example, appear to be a direct result of acquired resistance when comparing OxR and RuR to their parental sensitive counterparts (Figure 2).

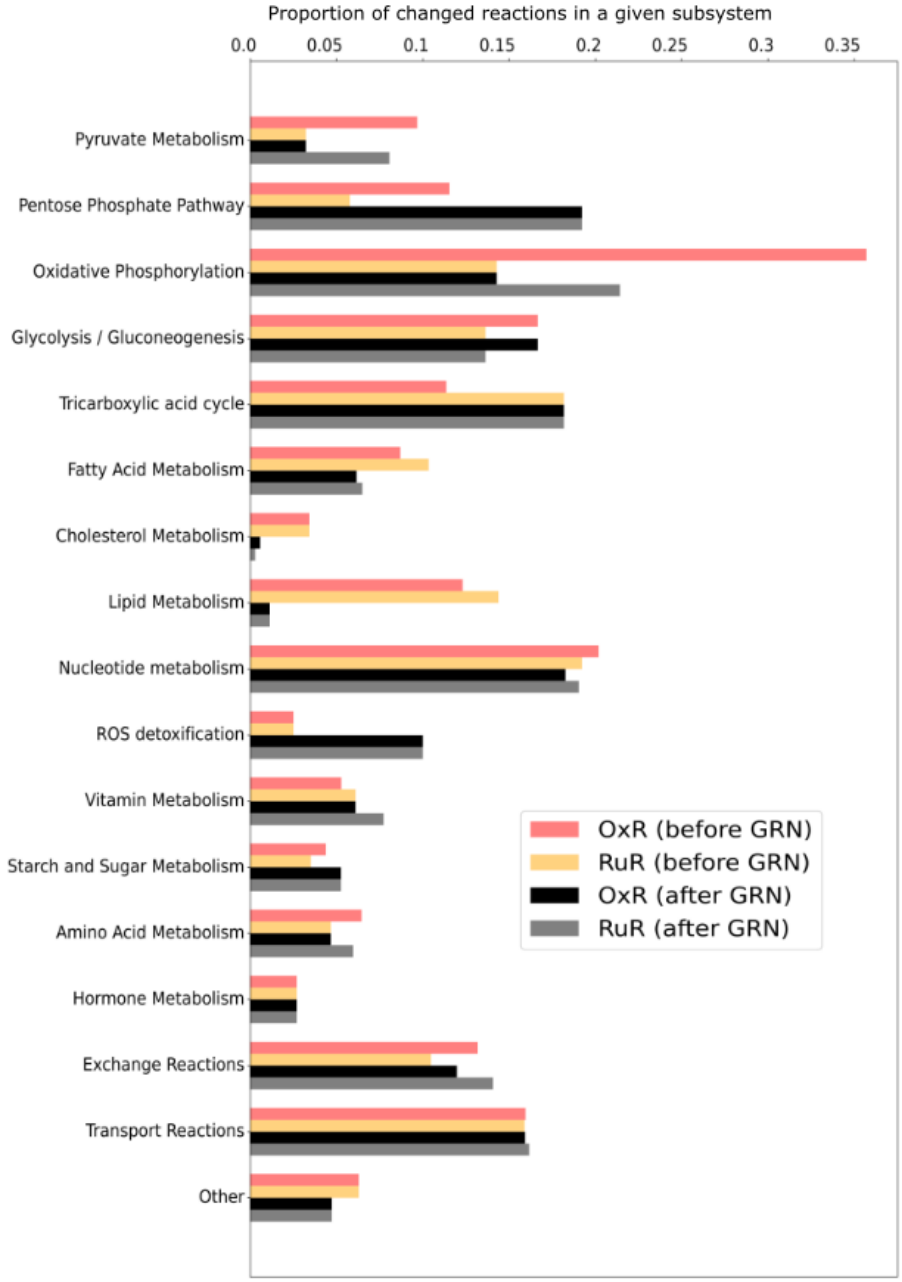

Figure 2. Metabolic fluxes in resistant versus sensitive models before and after growth rate normalization. Both intracellular and extracellular metabolite constraints were applied to generate four instances of the HCT-specific GSMM [oxaliplatin (OxR) and BOLD-100/KP1339 (RuR) and their parental sensitive counterparts (sensitive and sensitive-DMSO, respectively)] as described in the Section 2. A parsimonious thermodynamic flux variability analysis (pTFVA) was done on each model instance. Flux values of the resistant instances were compared to their respective controls. Metabolic reactions that had an absolute relative difference greater than 15% in both the highest possible and the lowest possible flux value were considered to be different. The proportion of reactions that show a difference in flux between the OxR and sensitive condition [OxR before growth rate normalization (GRN); red bars] and the RuR and sensitive conditions (RuR before GRN; orange bars) are shown for each subsystem (pre-defined pathways in the GSMM). All flux values were then normalized according to the corresponding growth rate of that condition (Figure S1) and were again checked for a relative difference between OxR (OxR after GRN; black bars) and RuR (RuR after GRN; gray bars) and their sensitive controls. Subsystems for which no relative changes in flux between resistant and sensitive instances were observed were omitted from the figure for clarity.

3.2. Metallodrug Resistance Is Linked to Changes in Energy Metabolism

Integrating metabolite measurements into GSMMs allows for growth rate normalization of the calculated fluxes which in turn allows for a direct flux comparison between resistant and sensitive cells. The reprogramming of energy metabolism to support cell growth and proliferation is a major hallmark of cancer [1] and has previously been linked to the emergence of acquired drug resistance [3]. To further investigate the role of a reprogramming of energy metabolism upon acquired metallodrug resistance, we used the four instances of the HCT116 model (OxR, sensitive, RuR, sensitive-DMSO) to specifically assess differences in flux in pathways related to energy metabolism.

In the growth conditions considered here, glucose acts as the primary carbon source (Figure S2). Glucose is catabolized to pyruvate, generating two ATP during glycolysis. Pyruvate can then be transported into the mitochondria and converted to acetyl-CoA which then enters the TCA cycle or, in what is known as the Warburg effect in cancer cells [67], pyruvate can be converted to lactate. Acetyl-CoA can also be generated from fatty acid oxidation and sometimes amino acid catabolism (see [68] for a review). Fluxes corresponding to these three well-established energy pathways of colorectal cells along with the oxygen consumption are shown for each cell type in Figure 3. While glutaminolysis is another common means by which cancer cells support the Warburg effect [69], we did not measure high glutamine uptake rates in the considered growth conditions. In fact, our determined glucose and glutamine uptake rates are in the same orders of magnitude as previously determined for HCT116 cell lines grown in fetal bovine serum [61].

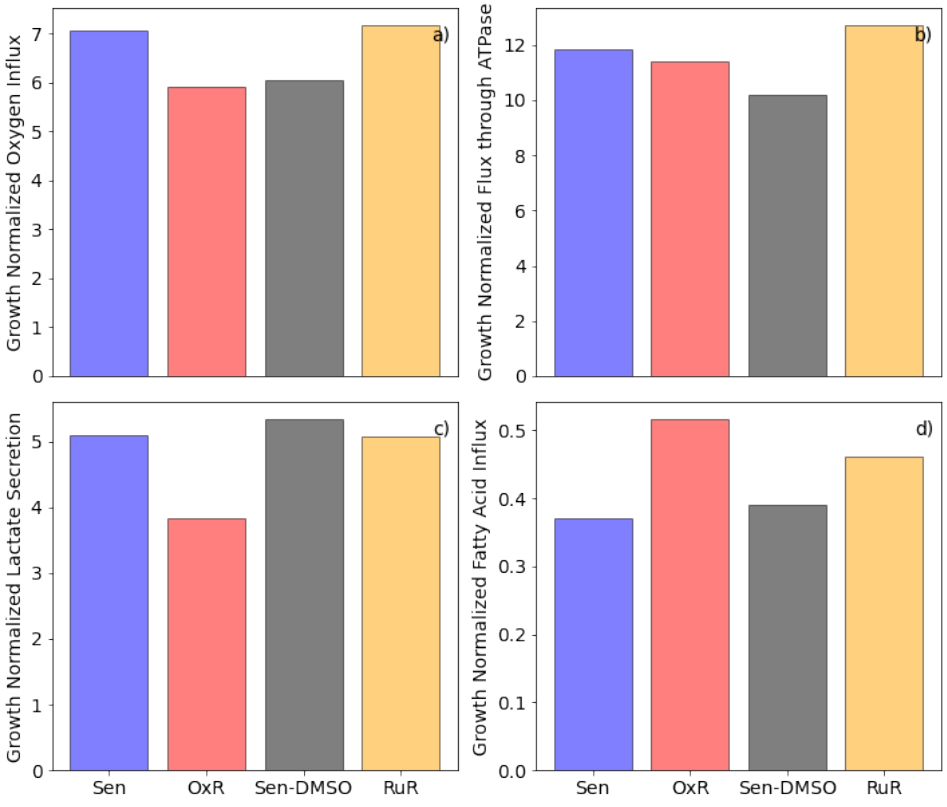

Figure 3. Comparison of fluxes through key energy metabolism reactions for ruthenium- and oxaliplatin-based resistant cells after growth rate normalization. Growth normalized flux values through (**a**) the oxygen uptake reaction—HMR_9048, (**b**) the ATP synthase reaction—HMR_6916, (**c**) the lactate secretion reaction—HMR_9135, and (**d**) the fatty acid influx—sum of m01362s_FAx, m02387s_FAx, m02389s_FAx, m02646s_FAx, m02674s_FAx, m02938s_FAx, across the four model instances (sensitive, Sen—blue bars; sensitive in a DMSO-containing medium, Sen-DMSO—gray bars; oxaliplatin-resistant, OxR—red bards; BOLD-100/KP1339, RuR—yellow bars) are shown. Fatty acid influx is the combined influx of stearate, palmitate, oleate, linolenate, linoleate, arachidonate.

We observe that OxR cells convert less pyruvate into lactate, but in turn consume a higher relative amount of fatty acids compared to their parental sensitive cells. RuR cells, however, show a high glycolytic flux and a high oxygen consumption as well as higher fatty acid consumption than their sensitive counterparts (Figure 3). Notably, the flux values shown in Figure 3 are growth normalized and may therefore not directly correspond to what would be observed in a traditional oxygen consumption rate (OCR) versus extracellular acidification rate (ECAR) experiment [70]. When comparing experimentally determined OCR and ECAR measurements to the non-normalized model results, we find a close agreement with regard to the differences in glycolysis and respiration between sensitive and resistant cells (Figures S4 and S6); thus further validating the set model constraints.

With the four instances of the HCT116-specific GSMMs, further conditions encountered in the tumor environment can be simulated. Simulating the effect of hypoxic growth conditions, we first set the oxygen influx for each model instance to the minimum possible value and then observe the minimum required fatty acid influx as we iteratively increase the oxygen influx, thus plotting the growth normalized production envelope of oxygen versus minimum fatty acid influx for each of the four conditions (Figure 4). While RuR cells appear to have a lower tolerance for hypoxic conditions, they also have a higher fatty acid requirement under those conditions when compared to the sensitive simulations (Figure 4c,d). While the same difference can be observed between OxR and sensitive simulations, it is less pronounced (Figure 4a,b).

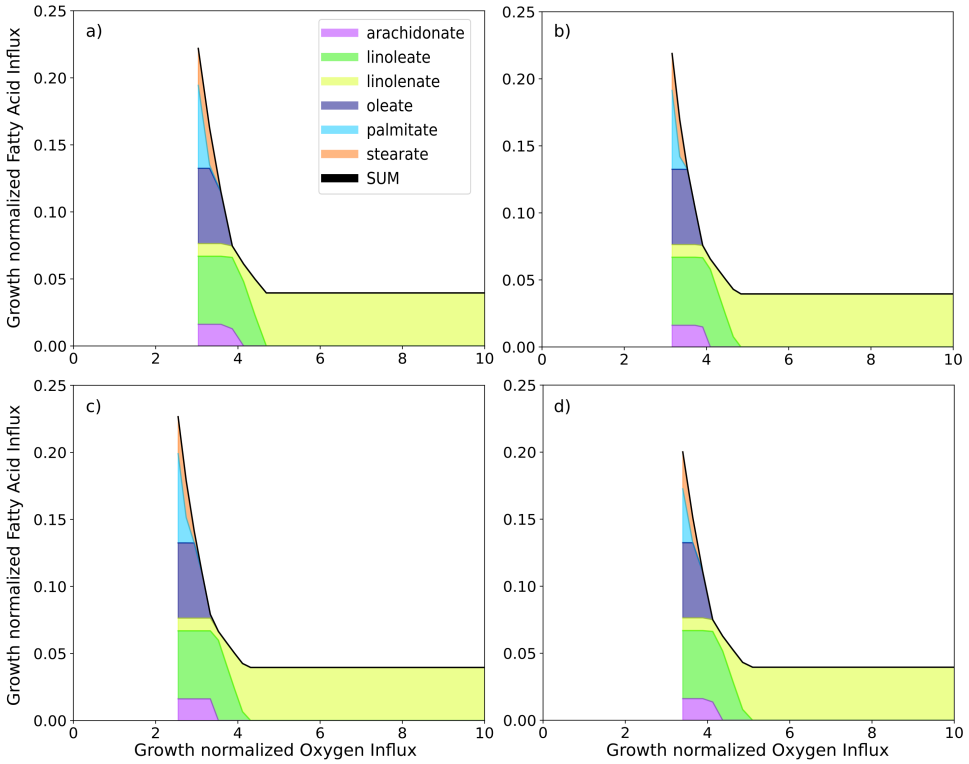

Figure 4. Simulating minimum fatty acid uptake requirement in response to various oxygen uptake constraints. Oxygen influx constraints were applied to each of the model instances (**a**) sensitive, (**b**) oxaliplatin-resistant, (**c**) sensitive in DMSO-containing medium, and (**d**) BOLD-100/KP1339-resistant. Using a parsimonious thermodynamic flux variability analysis (pTFVA; see Methods and Materials for details) the minimum possible fatty acid uptake was calculated for each oxygen constraint as shown. Fatty acid influx is the combined influx (black line) of stearate (orange), palmitate (cyan), oleate (dark purple), linolenate (yellow), linoleate (green), arachidonate (light purple).

We then set a minimum possible fatty acid influx and iteratively increased the total fatty acid influx to the model while calculating the minimum required oxygen influx (Figure 4). We repeated this calculation for various biomass constraints and note that there is an optimal fatty acid influx for minimizing the total oxygen required. In fact, this

optimal value corresponds directly to the fatty acid uptake rates observed in Figure 3d and is in accordance with the parsimonious thermodynamic flux variability analysis which minimizes the total sum of fluxes (see Section 2 for details).

Crucially, while a direct comparison between resistant and sensitive cells for each drug respectively can be made, we cannot make a direct comparison between the two drug resistance models (Figures 1–5). Because RuR cells were grown in a DMSO-containing medium whereas OxR cells were not, we cannot, at this stage, distinguish a resistance model-specific effect from a solvent background-induced effect.

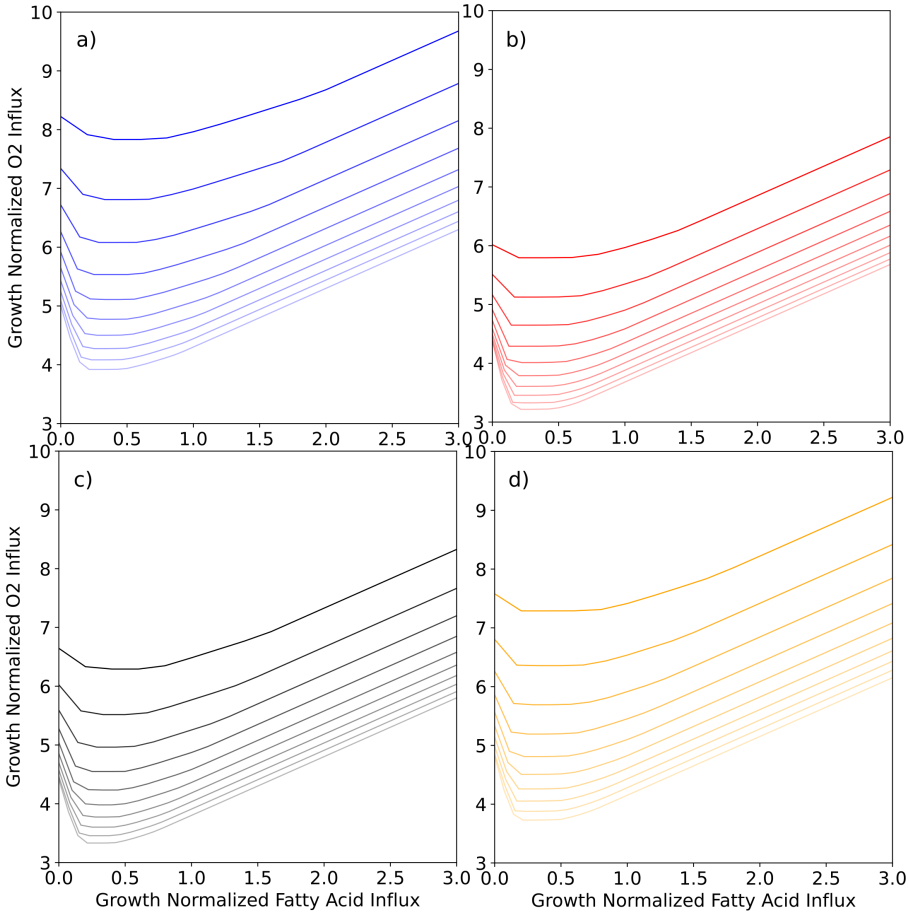

Figure 5. Simulating minimum oxygen requirement in response to various fatty acid uptake and biomass constraints. Fatty acid influx constraints were applied to each of the model instances (**a**) sensitive—blue lines, (**b**) oxaliplatin-resistant—red lines, (**c**) sensitive in DMSO-containing medium—black lines, and (**d**) BOLD-100/KP1339-resistant—yellow lines. Using a parsimonious flux variability analysis (pTFVA; see Methods and Materials for details) the minimum possible oxygen uptake was calculated for each fatty acid constraint. The calculations were performed for various growth rate constraints ranging from 5 to 15 h^{-1}, as indicated by the fading lines. Fatty acid influx constraints were applied as the combined influx of stearate, palmitate, oleate, linolenate, linoleate, arachidonate.

3.3. Growth Rate and Medium Normalization Allows for a Direct Comparison of Fluxes of Cells Grown Across Heterogeneous Conditions

In order to be able to compare the metabolic profiles of the two metallodrug resistance phenotypes directly, we finally normalized the flux results obtained from the metallo-resistant model instances against their respective parental sensitive counterparts (see Section 2 for further details). By dividing growth rate normalized and feature-scaled flux values calculated for the resistant models by those calculated for the respective sensitive models, we add a further normalization step. This normalization step eliminates observed differences in flux values that are the result of differences due to the presence of DMSO-

background. Because the parental sensitive counterparts were grown in the same medium as their resistant counterparts, we can assume that shared differences in flux between sensitive and resistant cells are the result of differences caused by DMSO. As such, this normalization step allows us to directly compare the two acquired resistances, OxR and RuR, to one another even though RuR, unlike OxR, was grown in a medium with low solvent (DMSO) background. The comparison of OxR and RuR (Figure 6) cells highlights an upregulation of fluxes associated with amino acid and fatty acid metabolism in RuR. OxR cells, on the other hand, show an upregulation in glycolysis and starch and sugar metabolism when compared to RuR cells (Figure 6b).

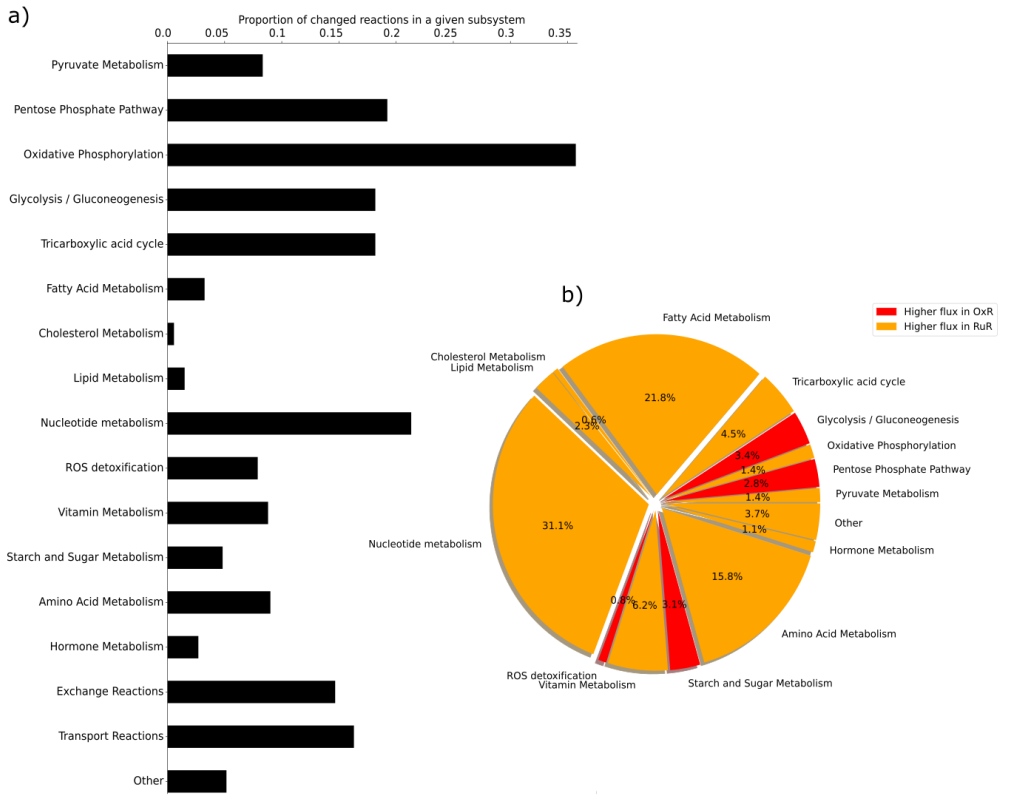

Figure 6. Predicted differences in the metabolic fluxes of ruthenium- and oxaliplatin-based resistances after growth rate and medium normalization. Both intracellular and extracellular metabolite constraints were applied to generate four instances of the HCT-specific GSMMs (oxaliplatin (OxR) and BOLD-100/KP1339 (RuR) and their sensitive parental counterparts (WT and WT-DMSO, respectively)) as described in the Materials and Methods. A parsimonious thermodynamic flux variability analysis (pTFVA) was done on each model instance. Each set of flux values was divided by the corresponding flux through biomass (Figure S1), thus normalizing for differences in growth. Flux values were then feature-scaled to lie between 0 and 1 and the flux values obtained in the drug-resistant instances were divided by the flux values of the corresponding control instances, thus normalizing for difference in medium composition. (**a**) The relative changes in flux between OxR and RuR instances were calculated and the total number of reactions that showed an absolute relative difference greater than 15% in relative upper and lower flux values were counted for each subsystem. The proportion of reactions that are significantly different in each subsystem is shown as black bars. Subsystems for which no relative changes in flux between the two resistant instances were observed were omitted from the figure for clarity. (**b**) Percentage of reactions in a subsystem which were identified as significantly different out of all reactions that were identified as significantly different between the two conditions are shown as a pie chart. Subsystems for which the total flux values were higher in OxR are shown in red. Subsystems for which total flux values were higher in the RuR are shown in orange. The subsystems transport reactions were omitted from this analysis as together they make up over 95% of the significantly different reactions.

Notably, when comparing the OxR and RuR model instances to their respective parental HCT116 drug-sensitive counterparts, prior to growth normalization, we identified 1039 (OxR) and 1180 (RuR) fluxes that were significantly different. Upon growth normalization, these numbers reduced to 743 (OxR) and 883 (RuR), highlighting that hundreds of differences observed in the non-normalized results are simply the result of a difference in growth rate. The OxR versus RuR comparison upon growth-media DMSO-background normalization highlighted 670 different reactions, suggesting that another 73 of reactions were initially observed as significantly different because of presence of 0.5% DMSO.

4. Discussion

Genome-scale metabolic models (GSMMs) provide a platform for integrating omics data sets and for analysing them in the context of metabolic fluxes. As we have shown, GSMMs can be constrained using both extracellular and intracellular metabolite concentrations to study metallodrug resistance in colon cancer. Approximately one-hundred metabolite constraints were applied to study the effect of changes in their concentrations in thousands of reactions. Colorectal-specific GSMMs have previously been constructed [12,48,58,71] but have not yet been applied to study metallo-drug resistance specifically. Here, we compared metabolic flux alterations in HCT116 cell models with acquired oxaliplatin- (OxR) vs. BOLD-100/KP1339 resistance (RuR) relative to parental, drug-sensitive HCT116 cells grown in the respective growth media without or with 0.5% DMSO.

In this study, we investigated various pathways in silico including glycolysis, the tricarboxylic acid cycle, fatty acid and amino acid metabolism, beta-oxidation, the pentose phosphate pathway. A comprehensive stable isotope resolved metabolic flux analysis considering such a diverse set of pathways would require the application of multiple different positionally labelled isotopic tracers [27,72]. In addition to economic factors, practical challenges may also play a role in experimental design. The application of palmitate to study beta-oxidation, for example, requires the conjugation of fatty acid free bovine serum albumin [73]. Moreover, it usually has high background contamination from plastic materials [74]. Finally, stable isotope labeling in living organisms is even more complex from a data evaluation perspective [75]. Thus, a purely experimental study that provides a holistic analysis of metabolic reprogramming in cancer is currently infeasible.

There is no simple relationship between changes in metabolite concentrations and changes in flux [76]. This notion also applies to acquired resistance in the HCT116 colorectal cancer cell line. We have shown that observed differences in metabolite concentrations between resistant and sensitive conditions may not necessarily reflect a drug resistance-specific response but may instead arise as a result of differences in growth rate or solvent conditions. If we want to compare changes in metabolic flux of cells grown in heterogeneous conditions, data needs to be normalized in order for valid comparisons to be made. Here we have outlined a procedure for this kind of normalization based on thermodynamic genome-scale metabolic modelling of the HCT116 cell line.

Accurate comparative profiling of metabolic changes observed across heterogenous conditions remains a challenge. Differences in growth rates and impact of solvent necessities will result in observed differences in metabolite concentrations but are not causal to a reprogramming of metabolism [77]. Considering cellular fluxes as the metabolic phenotype through the use of GSMMs has the advantage that fluxes, unlike concentrations, can easily be normalized with regard to other rate measurements, such as growth rate or exchange rates (e.g., [78–80]).

As a prerequisite to produce accurate, quantitative metabolomics data [77], we normalized the metabolite amounts to total protein content, calculating absolute concentrations based on internal standardization. Even though this approach is superior to relative quantification and is able to compensate for technical variation of the sample preparation and differences in extracted biomass, it does not account for biological processes like growth or environmental factors such as differences in medium composition.

Integrating the metabolite data as part of a thermodynamic flux analysis allows us to normalize the calculated reaction rates by the growth rate observed under the corresponding conditions. We showed that growth-normalization reduces the number of reactions that are different between resistant and sensitive model instances and changes some of the conclusions about altered metabolic pathways entirely. Growth normalization is therefore a critical step when looking for drug-specific metabolic phenotypes. A second limitation to studying non-normalized metabolite concentrations is that data obtained from heterogeneous conditions cannot be directly compared. Using the growth normalized flux results we further normalized each resistant model against its sensitive counterpart which was grown in an identical medium and solvent composition. Hence, we were able to do a direct comparison between the two metallo-resistances and to identify drug resistance-specific responses.

A limitation to our approach is that we first normalized our flux results to differences in growth rate and then normalized each resistant model against its respective counterpart. This means that we are unable to capture emergent properties that result from both differences in growth rate and solvent impact; we assume that a combined effect of the two is minimal. Furthermore our flux analyses assume metabolism to be in steady-state, such that intracellular concentrations are constant. Nonetheless, we have clearly demonstrated that a growth and medium/solvent normalization is non-trivial as it allows for comparisons across heterogeneous conditions. We expect this method to be of wider applicability in studies where the effects of medium compositions, such as the availability of carbon sources to a cell, are of interest.

Time-dependent changes of metabolite profiles have previously been considered [81,82], but are not typically integrated at a genome-scale level. Measuring metabolite concentrations alongside cell counts at various time points and quantifying the relative metabolite abundance per cell using linear regression, Dubuis et al. [81] account for deviations from steady-state. The method was then further developed, using intermediates of fatty acid metabolism and other metabolites to account for differences in cell size [82]. While the difference in cell size can be interpreted as a proxy of growth rate, it cannot be assumed that the observed changes in metabolite concentrations directly translate to differences in metabolic activity, i.e., fluxes. Metabolic responses associated with an acquired metallodrug resistance in cancer have not yet been studied extensively using constraint-based flux analyses [39,83,84]. The use of GSMMs to integrate metabolomics data to study cellular fluxes, however, provides multiple new opportunities in this field.

Defense mechanisms and acquired resistance are well known phenomena when applying metal-based drugs as anticancer agents. Reduced efficacy due to acquired resistance remains a major challenge in systemic anticancer therapy. The complexity is increasingly recognized, as the contribution of epigenetic and metabolic effects will be uncovered. Drug-specific and tumor tissue specific mechanisms have been described, and more recently the tumor microenvironment has come into focus [85]. Accordingly, response profiling with metabolomics analysis can be a powerful tool for investigating drugs and drug candidates [28,29] and dissecting emerging resistance [86]. Currently, only a handful of studies consider metallodrugs applied to cancers with metabolomics [87–89], and even fewer investigate acquired metallodrug resistance [53].

In this work, we consider an in vitro study of colon cancer. Gastrointestinal cancer cell lines, including colorectal cancer cell line HCT116 activate beta-oxidation as a response to oxaliplatin treatment and conversely become more sensitive to oxaliplatin upon inhibition of fatty acid catabolism [23]. A seminal study in the field integrates both metabolomics and transcriptomics and finds that, within 59 NCI60 cell lines, the metabolic basis of platinum-sensitivity can largely be attributed to energy metabolism (TCA cycle, glutaminolysis, pyruvate metabolism), lipoprotein uptake, and nucleotide synthesis [90]. The results from our in silico analysis are in line with these findings, also highlighting the importance of energy metabolism (OXPHOS, glycolysis, TCA).

Figure 6 highlights the relevance of fatty acid metabolism, as fluxes from this subsystem contribute to 12.5% of all observed differences (excluding all transport reactions)

between the RuR and OxR, showing elevated fluxes in RuR. This supports existing evidence of beta-oxidation activation in response to metallodrug treatment [23]. Interestingly, for the majority of observed flux differences between OxR and RuR, flux values are higher in the RuR, implying a higher metabolic activity in this phenotype, independently of differences in growth rate. OxR, however, does exhibit elevated activity in the glycolysis/glyconeogenesis and pentose phosphate pathways. Thus, our comparison of the growth rate- and medium-normalized reaction rates supports the notion that an acquired resistance to the two metallodrugs is marked by differences in their metabolic phenotype with an overall higher metabolic activity in the RuR system.

The high metabolic plasticity of cancer cells enables efficient detoxification and protection strategies [85]. Normalization of the flux values by growth rate substantially reduces the observed differences (Figure 2) in most of the investigated pathways. In contrast, both the pentose phosphate pathway and ROS detoxification subsystem, which includes glutathione-synthesis, were emphasized to the same extent in both the OxR and RuR resistance models upon growth standardization. This supports the notion that metallodrugs interfere with cellular redox homeostasis and stimulate a readiness to counter reactive oxygen species (also by synthesizing NADPH via the pentose phosphate pathway) which has previously been described to conjugate glutathione to platinum complexes with glutathione-S-transferase [91].

Despite shared commonalities like the production of ROS, it is expected that RuR and OxR models display different metabolic phenotypes, because of known differences in their modes of action [26,92,93]. Oxaliplatin, for example, is primarily a DNA targeting drug, whereas BOLD-100/KP1339 has recently been found to have a prodrug nature and is capable of causing ER-stress and the downregulation of GRP78, encoding an endoplasmic reticulum chaperone protein, which has been linked to malignancy [94]. It is widely accepted that DNA repair mechanisms play a crucial role in resistance to oxaliplatin [95]. It is important to note that, using GSMM, we have here focused solely on metabolic changes to compare metabolic reprogramming of the two acquired resistances but cannot exclude further regulatory events.

The comparison of fluxes through key energy metabolism reactions (Figure 3) shows that both acquired resistances are defined by lowered glycolytic flux than their sensitive parental cells, although this is less pronounced with RuR. Growth normalization does not affect this observation (Figure S4). The same cannot be said about the fatty acid beta-oxidation, where upon growth standardization the acquired resistance models both show a higher fatty acid requirement than their sensitive controls (Figure 3d; Figure S4d). Additionally, upon growth normalization OxR has lower and RuR higher respiration rates than corresponding sensitive counterparts (Figure 3a). The calculated rates correspond well to the experimentally determined results with a Seahorse assay (Figure S6). As expected the experimentally determined and non-normalized in vitro results align more closely with the non-normalized flux values modelled in silico.

Drastic changes in oxygen and fatty acid availability are known stress conditions in a tumor microenvironment, and are assumed to be managed with metabolic adaptations [4]. Lipid dependency, for example, is more pronounced under hypoxic conditions and relies on the uptake of extracellular fatty acids [73,96,97]. We thus used the condition-specific instances of our constrained GSMM to further inspect the relationship between hypoxia and fatty acid uptake. We found that the composition of fatty acids taken up changes in response to oxygen limitation (Figure 4). Under normoxic conditions linolenate can act as the sole fatty acid source. As oxygen limitation becomes more pronounced, linoleate, arachidonate, oleate, stearate and finally palmitate are also required. RuR cells require less fatty acids under oxygen limitation compared to their sensitive counterpart (Figure 4c,d); while the same is true for OxR, the observed difference is notably less pronounced (Figure 4a,b).

Additionally, the investigation of minimum oxygen requirement at various fatty acid influxes (Figure 5) revealed that the optimal fatty acid composition, which has the lowest oxygen demand, is the same across growth rates. Overall, OxR has the lowest oxygen

requirement, which suggests that if sufficient fatty acids are available, OxR will be the most resilient of the investigated models against hypoxia (Figure 5).

5. Conclusions

There are different ways to capture the metabolic phenotype of a cell. Metabolic profiling via metabolomics provides an interrogation window of the intracellular concentrations at a given point in time. Extracellular concentrations measured over time provide insight to the cellular uptake and excretion rates of cells. Together they can be integrated to constrain the solution space of a genome-scale metabolic model. The calculated flux values can then be normalized according to growth rates and environmental conditions, allowing for drug resistance specific metabolic responses to be identified across heterogenous conditions. We find the outlined normalization steps to be crucial in the interpretation of the results and show that metabolic reprogramming is more extensive in BOLD-100/KP1339 resistant cells than in oxaliplatin resistant cells. We identify pathways, such as fatty acid and amino acid metabolism, to be upregulated in response to a resistance acquired to a ruthenium-based drug when compared to a platinum-based drug. All in all, genome-scale metabolic modelling provides a valuable platform for putting observed changes in metabolite concentrations in the context of metabolic fluxes.

Supplementary Materials: The following are available at https://www.mdpi.com/article/10.3390/cancers13164130/s1, Figure S1: Experimentally determined exchanged fluxes used to constrain the HCT116-specific genome-scale metabolic model, Figure S2: Observed differences in growth rate between drug treatments and their sensitive controls, Figure S3: Cell dry weight of wild-type and resistant cells, Figure S4: Comparison of fluxes through key energy metabolism reactions for ruthenium- and oxaliplatin-based resistances before growth rate normalization, Figure S5: Investigation of cross-resistance of the resistance model HCT116 with acquired BOLD-100/KP1339-resistance towards oxaliplatin and cross-resistance of HCT116 with acquired oxaliplatin-resistance towards BOLD-100/KP1339, Figure S6: Mito Stress test measuring the metabolic parameters OCR and ECAR with the Seahorse FX analyzer of sensitive vs. oxaliplatin-resistant HCT116 cells; and sensitive vs. BOLD-100/KP1339-resistant HCT116 cells.

Author Contributions: Conceptualization, G.K. and J.Z.; Funding acquisition G.K. and J.Z.; Methodology, H.A.H., M.R., D.B., W.B., G.K. and J.Z.; Software, H.A.H.; Investigation, M.R.; Resources, M.R., D.B., M.A.J., B.K.K. and W.B.; Supervision, G.K. and J.Z.; Visualization, H.A.H. and D.B.; Writing—original draft, H.A.H. and M.R.; Writing—review editing, all authors. All authors have read and agreed to the published version of the manuscript.

Funding: This research received no external funding. Open Access Funding by the University of Vienna.

Institutional Review Board Statement: Not applicable.

Informed Consent Statement: Not applicable.

Data Availability Statement: All data and code used to conduct the analyses presented in this manuscript are available on GitHub (https://github.com/HAHerrmann/Hct116_DrugRes, accessed on 12 August 2021) and Zenodo (DOI: 10.5281/zenodo.4633725 (https://zenodo.org/record/4633725, accessed on 12 August 2021)). Metabolomics data (LC high-resolution mass spectrometry-based metabolomics dataset in rawdata and total protein contents corresponding to the samples) have been deposited to the EMBL-EBI MetaboLights database [98] with the identifier MTBLS2665 for the OxR-batch and MTBLS2681 for the RuR-batch. The complete dataset can be accessed at https://www.ebi.ac.uk/metabolights/MTBLS2665, accessed on 12 August 2021 and https://www.ebi.ac.uk/metabolights/MTBLS2681, accessed on 12 August 2021 for the OxR- and RuR-batch, respectively.

Conflicts of Interest: The authors declare that they have no competing interests.

References

1. Hanahan, D.; Weinberg, R.A. Hallmarks of Cancer: The Next Generation. *Cell* **2011**, *144*, 646–674. [CrossRef]
2. Vernieri, C.; Casola, S.; Foiani, M.; Pietrantonio, F.; Braud, F.D.; Longo, V. Targeting Cancer Metabolism: Dietary and Pharmacologic Interventions. *Cancer Discov.* **2016**, *6*, 1315–1333. [CrossRef]
3. Zaal, E.A.; Berkers, C.R. The Influence of Metabolism on Drug Response in Cancer. *Front. Oncol.* **2018**, *8*, 148. [CrossRef]
4. Faubert, B.; Solmonson, A.; DeBerardinis, R.J. Metabolic reprogramming and cancer progression. *Science* **2020**, *368*, eaaw5473 . [CrossRef]
5. Agren, R.; Bordel, S.; Mardinoglu, A.; Pornputtapong, N.; Nookaew, I.; Nielsen, J. Reconstruction of Genome-Scale Active Metabolic Networks for 69 Human Cell Types and 16 Cancer Types Using INIT. *PLoS Comput. Biol.* **2012**, *8*, e1002518. [CrossRef] [PubMed]
6. Nilsson, A.; Nielsen, J. Genome scale metabolic modeling of cancer. *Metab. Eng.* **2017**, *43*, 103–112. [CrossRef] [PubMed]
7. Jalili, M.; Scharm, M.; Wolkenhauer, O.; Damaghi, M.; Salehzadeh-Yazdi, A. Exploring the Metabolic Heterogeneity of Cancers: A Benchmark Study of Context-Specific Models. *J. Pers. Med.* **2021**, *11*, 496. [CrossRef] [PubMed]
8. Folger, O.; Jerby, L.; Frezza, C.; Gottlieb, E.; Ruppin, E.; Shlomi, T. Predicting selective drug targets in cancer through metabolic networks. *Mol. Syst. Biol.* **2011**, *7*, 501. [CrossRef]
9. Frezza, C.; Zheng, L.; Folger, O.; Rajagopalan, K.N.; MacKenzie, E.D.; Jerby, L.; Micaroni, M.; Chaneton, B.; Adam, J.; Hedley, A.; et al. Haem oxygenase is synthetically lethal with the tumour suppressor fumarate hydratase. *Nature* **2011**, *477*, 225–228. [CrossRef]
10. Gatto, F.; Miess, H.; Schulze, A.; Nielsen, J. Flux balance analysis predicts essential genes in clear cell renal cell carcinoma metabolism. *Sci. Rep.* **2015**, *5*, 10738. [CrossRef]
11. Jerby, L.; Ruppin, E. Predicting Drug Targets and Biomarkers of Cancer via Genome-Scale Metabolic Modeling. *Clin. Cancer Res.* **2012**, *18*, 5572–5584. [CrossRef]
12. Zhang, C.; Aldrees, M.; Arif, M.; Li, X.; Mardinoglu, A.; Aziz, M.A. Elucidating the Reprograming of Colorectal Cancer Metabolism Using Genome-Scale Metabolic Modeling. *Front. Oncol.* **2019**, *9*, 681, [CrossRef] [PubMed]
13. Dallas, N.A.; Xia, L.; Fan, F.; Gray, M.J.; Gaur, P.; Buren, G.V.; Samuel, S.; Kim, M.P.; Lim, S.J.; Ellis, L.M. Chemoresistant Colorectal Cancer Cells, the Cancer Stem Cell Phenotype, and Increased Sensitivity to Insulin-like Growth Factor-I Receptor Inhibition. *Cancer Res.* **2009**, *69*, 1951–1957. [CrossRef]
14. Hu, T.; Li, Z.; Gao, C.Y.; Cho, C.H. Mechanisms of drug resistance in colon cancer and its therapeutic strategies. *World J. Gastroenterol.* **2016**, *22*, 6876–6889. [CrossRef] [PubMed]
15. Stein, A.; Atanackovic, D.; Bokemeyer, C. Current standards and new trends in the primary treatment of colorectal cancer. *Eur. J. Cancer* **2011**, *47*, S312–S314. [CrossRef]
16. Vasan, N.; Baselga, J.; Hyman, D.M. A view on drug resistance in cancer. *Nature* **2019**, *575*, 299–309. [CrossRef] [PubMed]
17. Gill, S.; Thomas, R.R.; Goldberg, R.M. Colorectal cancer chemotherapy. *Aliment. Pharmacol. Ther.* **2003**, *18*, 683–692. [CrossRef]
18. Anthony, E.J.; Bolitho, E.M.; Bridgewater, H.E.; Carter, O.W.L.; Donnelly, J.M.; Imberti, C.; Lant, E.C.; Lermyte, F.; Needham, R.J.; Palau, M.; et al. Metallodrugs are unique: Opportunities and challenges of discovery and development. *Chem. Sci.* **2020**, *11*, 12888–12917. [CrossRef]
19. Savvas, P.; Efrosini, K.; Athanasios, S. Metallodrugs in Targeted Cancer Therapeutics: Aiming at Chemoresistance-related Patterns and Immunosuppressive Tumor Networks. *Curr. Med. Chem.* **2019**, *26*, 607–623.
20. Sung, H.; Ferlay, J.; Siegel, R.L.; Laversanne, M.; Soerjomataram, I.; Jemal, A.; Bray, F. Global cancer statistics 2020: GLOBOCAN estimates of incidence and mortality worldwide for 36 cancers in 185 countries. *CA Cancer J. Clin.* **2020**, *71* , 209–249. [CrossRef]
21. Johnstone, T.C.; Park, G.Y.; Lippard, S.J. Understanding and Improving Platinum Anticancer Drugs–Phenanthriplatin. *Anticancer Res.* **2014**, *34*, 471–476.
22. Zhou, J.; Kang, Y.; Chen, L.; Wang, H.; Liu, J.; Zeng, S.; Yu, L. The Drug-Resistance Mechanisms of Five Platinum-Based Antitumor Agents. *Front. Pharmacol.* **2020**, *11*, 343. [CrossRef]
23. Wang, Y.; Lu, J.H.; Wang, F.; Wang, Y.N.; He, M.M.; Wu, Q.N.; Lu, Y.X.; Yu, H.E.; Chen, Z.H.; Zhao, Q.; et al. Inhibition of fatty acid catabolism augments the efficacy of oxaliplatin-based chemotherapy in gastrointestinal cancers. *Cancer Lett.* **2020**, *473*, 74–89. [CrossRef]
24. Burris, H.A.; Bakewell, S.; Bendell, J.C.; Infante, J.; Jones, S.F.; Spigel, D.R.; Weiss, G.J.; Ramanathan, R.K.; Ogden, A.; Hoff, D.V. Safety and activity of IT-139, a ruthenium-based compound, in patients with advanced solid tumours: A first-in-human, open-label, dose-escalation phase I study with expansion cohort. *ESMO Open* **2016**, *1*, e000154. [CrossRef]
25. Trondl, R.; Heffeter, P.; Kowol, C.R.; Jakupec, M.A.; Berger, W.; Keppler, B.K. NKP-1339, the first ruthenium-based anticancer drug on the edge to clinical application. *Chem. Sci.* **2014**, *5*, 2925–2932. [CrossRef]
26. Meier-Menches, S.M.; Gerner, C.; Berger, W.; Hartinger, C.G.; Keppler, B.K. Structure–activity relationships for ruthenium and osmium anticancer agents—Towards clinical development. *Chem. Soc. Rev.* **2018**, *47*, 909–928. [CrossRef] [PubMed]
27. Jang, C.; Chen, L.; Rabinowitz, J.D. Metabolomics and Isotope Tracing. *Cell* **2018**, *173*, 822–837. [CrossRef] [PubMed]
28. Armitage, E.G.; Godzien, J.; Peña, I.; López-Gonzálvez, Á.; Angulo, S.; Gradillas, A.; Alonso-Herranz, V.; Martín, J.; Fiandor, J.M.; Barrett, M.P.; et al. Metabolic Clustering Analysis as a Strategy for Compound Selection in the Drug Discovery Pipeline for Leishmaniasis. *ACS Chem. Biol.* **2018**, *13*, 1361–1369. [CrossRef] [PubMed]

29. Armitage, E.G.; Southam, A.D. Monitoring cancer prognosis, diagnosis and treatment efficacy using metabolomics and lipidomics. *Metabolomics* **2016**, *12*, 146. [CrossRef]
30. Zamboni, N.; Saghatelian, A.; Patti, G.J. Defining the Metabolome: Size, Flux, and Regulation. *Mol. Cell* **2015**, *58*, 699–706. [CrossRef]
31. Buescher, J.M.; Antoniewicz, M.R.; Boros, L.G.; Burgess, S.C.; Brunengraber, H.; Clish, C.B.; DeBerardinis, R.J.; Feron, O.; Frezza, C.; Ghesquiere, B.; et al. A roadmap for interpreting 13C metabolite labeling patterns from cells. *Curr. Opin. Biotechnol.* **2015**, *34*, 189–201. [CrossRef]
32. Eicher, T.; Kinnebrew, G.; Patt, A.; Spencer, K.; Ying, K.; Ma, Q.; Machiraju, R.; Mathé, E.A. Metabolomics and Multi-Omics Integration: A Survey of Computational Methods and Resources. *Metabolites* **2020**, *10*, 202. [CrossRef] [PubMed]
33. Meng, C.; Kuster, B.; Culhane, A.C.; Gholami, A.M. A multivariate approach to the integration of multi-omics datasets. *BMC Bioinform.* **2014**, *15*, 162. [CrossRef] [PubMed]
34. Rampler, E.; Abiead, Y.E.; Schoeny, H.; Rusz, M.; Hildebrand, F.; Fitz, V.; Koellensperger, G. Recurrent Topics in Mass Spectrometry-Based Metabolomics and Lipidomics—Standardization, Coverage, and Throughput. *Anal. Chem.* **2021**, *93*, 519–545. [CrossRef] [PubMed]
35. Chen, Y.X.; Chen, H.; Rong, Y.; Jiang, F.; Chen, J.B.; Duan, Y.Y.; Zhu, D.L.; Yang, T.L.; Dai, Z.; Dong, S.S.; et al. An integrative multi-omics network-based approach identifies key regulators for breast cancer. *Comput. Struct. Biotechnol. J.* **2020**, *18*, 2826–2835. [CrossRef]
36. Ghaffari, S.; Hanson, C.; Schmidt, R.E.; Bouchonville, K.J.; Offer, S.M.; Sinha, S. An integrated multi-omics approach to identify regulatory mechanisms in cancer metastatic processes. *Genome Biol.* **2021**, *22*, 19. [CrossRef]
37. Bordbar, A.; Monk, J.M.; King, Z.A.; Palsson, B.O. Constraint-based models predict metabolic and associated cellular functions. *Nat. Rev. Genet.* **2014**, *15*, 107–120. [CrossRef]
38. Pandey, V.; Hadadi, N.; Hatzimanikatis, V. Enhanced flux prediction by integrating relative expression and relative metabolite abundance into thermodynamically consistent metabolic models. *PLoS Comput. Biol.* **2019**, *15*, e1007036. [CrossRef]
39. Yizhak, K.; Chaneton, B.; Gottlieb, E.; Ruppin, E. Modeling cancer metabolism on a genome scale. *Mol. Syst. Biol.* **2015**, *11*, 817. [CrossRef] [PubMed]
40. Yizhak, K.; Benyamini, T.; Liebermeister, W.; Ruppin, E.; Shlomi, T. Integrating quantitative proteomics and metabolomics with a genome-scale metabolic network model. *Bioinformatics* **2010**, *26*, i255–i260. [CrossRef]
41. Zur, H.; Ruppin, E.; Shlomi, T. iMAT: An integrative metabolic analysis tool. *Bioinformatics* **2010**, *26*, 3140–3142. [CrossRef]
42. Agren, R.; Mardinoglu, A.; Asplund, A.; Kampf, C.; Uhlen, M.; Nielsen, J. Identification of anticancer drugs for hepatocellular carcinoma through personalized genome-scale metabolic modeling. *Mol. Syst. Biol.* **2014**, *10*, 721. [CrossRef]
43. Lewis, N.E.; Nagarajan, H.; Palsson, B.O. Constraining the metabolic genotype–phenotype relationship using a phylogeny of in silico methods. *Nat. Rev. Microbiol.* **2012**, *10*, 291–305. [CrossRef]
44. O'Brien, E.J.; Lerman, J.A.; Chang, R.L.; Hyduke, D.R.; Palsson, B. Genome-scale models of metabolism and gene expression extend and refine growth phenotype prediction. *Mol. Syst. Biol.* **2013**, *9*, 693. [CrossRef]
45. Orth, J.D.; Thiele, I.; Palsson, B.Ø. What is flux balance analysis? *Nat. Biotechnol.* **2010**, *28*, 245–248. [CrossRef]
46. Henry, C.S.; Broadbelt, L.J.; Hatzimanikatis, V. Thermodynamics-Based Metabolic Flux Analysis. *Biophys. J.* **2007**, *92*, 1792–1805. [CrossRef]
47. Salvy, P.; Fengos, G.; Ataman, M.; Pathier, T.; Soh, K.C.; Hatzimanikatis, V. pyTFA and matTFA: A Python package and a Matlab toolbox for Thermodynamics-based Flux Analysis. *Bioinformatics* **2019**, *35*, 167–169. [CrossRef] [PubMed]
48. Aurich, M.K.; Paglia, G.; Rolfsson, Ó.; Hrafnsdóttir, S.; Magnúsdóttir, M.; Stefaniak, M.M.; Palsson, B.Ø.; Fleming, R.M.T.; Thiele, I. Prediction of intracellular metabolic states from extracellular metabolomic data. *Metabolomics* **2015**, *11*, 603–619. [CrossRef] [PubMed]
49. Masid, M.; Ataman, M.; Hatzimanikatis, V. Analysis of human metabolism by reducing the complexity of the genome-scale models using redHUMAN. *Nat. Commun.* **2020**, *11*, 2821. [CrossRef]
50. Volkova, S.; Matos, M.R.A.; Mattanovich, M.; Marín de Mas, I. Metabolic Modelling as a Framework for Metabolomics Data Integration and Analysis. *Metabolites* **2020**, *10*, 303. [CrossRef] [PubMed]
51. Zielinski, D.C.; Jamshidi, N.; Corbett, A.J.; Bordbar, A.; Thomas, A.; Palsson, B.Ø. Systems biology analysis of drivers underlying hallmarks of cancer cell metabolism. *Sci. Rep.* **2017**, *7*, 41241. [CrossRef]
52. Jungwirth, U.; Xanthos, D.N.; Gojo, J.; Bytzek, A.K.; Körner, W.; Heffeter, P.; Abramkin, S.A.; Jakupec, M.A.; Hartinger, C.G.; Windberger, U.; et al. Anticancer activity of methyl-substituted oxaliplatin analogs. *Mol. Pharmacol.* **2012**, *81*, 719–728. [CrossRef] [PubMed]
53. Galvez, L.; Rusz, M.; Schwaiger-Haber, M.; Abiead, Y.E.; Hermann, G.; Jungwirth, U.; Berger, W.; Keppler, B.K.; Jakupec, M.A.; Koellensperger, G. Preclinical studies on metal based anticancer drugs as enabled by integrated metallomics and metabolomics. *Metallomics* **2019**, *11*, 1716–1728. [CrossRef]
54. Rusz, M.; Del Favero, G.; El Abiead, Y.; Gerner, C.; Keppler, B.K.; Jakupec, M.A.; Koellensperger, G. Morpho-metabotyping the oxidative stress response. *Sci. Rep.* **2021**, *11*, 15471. [CrossRef]
55. Schwaiger, M.; Schoeny, H.; Abiead, Y.E.; Hermann, G.; Rampler, E.; Koellensperger, G. Merging metabolomics and lipidomics into one analytical run. *Analyst* **2018**, *144*, 220–229. [CrossRef] [PubMed]

56. Oberhuber, M.; Pecoraro, M.; Rusz, M.; Oberhuber, G.; Wieselberg, M.; Haslinger, P.; Gurnhofer, E.; Schlederer, M.; Limberger, T.; Lagger, S.; et al. STAT3-dependent analysis reveals PDK4 as independent predictor of recurrence in prostate cancer. *Mol. Syst. Biol.* **2020**, *16*, e9247. [CrossRef]
57. Széliová, D.; Schoeny, H.; Knez, V.; Troyer, C.; Coman, C.; Rampler, E.; Koellensperger, G.; Ahrends, R.; Hann, S.; Borth, N.; et al. Robust Analytical Methods for the Accurate Quantification of the Total Biomass Composition of Mammalian Cells. In *Metabolic Flux Analysis in Eukaryotic Cells: Methods and Protocols*; Nagrath, D., Ed.; Methods in Molecular Biology; Springer: New York, NY, USA, 2020; pp. 119–160. [CrossRef]
58. Robinson, J.L.; Kocabaş, P.; Wang, H.; Cholley, P.E.; Cook, D.; Nilsson, A.; Anton, M.; Ferreira, R.; Domenzain, I.; Billa, V.; et al. An atlas of human metabolism. *Sci. Signal.* **2020**, *13*, eaaz1482. [CrossRef]
59. Hart, T.; Chandrashekhar, M.; Aregger, M.; Steinhart, Z.; Brown, K.R.; MacLeod, G.; Mis, M.; Zimmermann, M.; Fradet-Turcotte, A.; Sun, S.; et al. High-Resolution CRISPR Screens Reveal Fitness Genes and Genotype-Specific Cancer Liabilities. *Cell* **2015**, *163*, 1515–1526. [CrossRef] [PubMed]
60. Széliová, D.; Ruckerbauer, D.E.; Galleguillos, S.N.; Petersen, L.B.; Natter, K.; Hanscho, M.; Troyer, C.; Causon, T.; Schoeny, H.; Christensen, H.B.; et al. What CHO is made of: Variations in the biomass composition of Chinese hamster ovary cell lines. *Metab. Eng.* **2020**, *61*, 288–300. [CrossRef]
61. Jain, M.; Nilsson, R.; Sharma, S.; Madhusudhan, N.; Kitami, T.; Souza, A.L.; Kafri, R.; Kirschner, M.W.; Clish, C.B.; Mootha, V.K. Metabolite Profiling Identifies a Key Role for Glycine in Rapid Cancer Cell Proliferation. *Science* **2012**, *336*, 1040–1044. [CrossRef]
62. Else, P.L. The highly unnatural fatty acid profile of cells in culture. *Prog. Lipid Res.* **2020**, *77*, 101017. [CrossRef]
63. Gregory, M.K.; King, H.W.; Bain, P.A.; Gibson, R.A.; Tocher, D.R.; Schuller, K.A. Development of a Fish Cell Culture Model to Investigate the Impact of Fish Oil Replacement on Lipid Peroxidation. *Lipids* **2011**, *46*, 753–764. [CrossRef]
64. Lewis, N.E.; Hixson, K.K.; Conrad, T.M.; Lerman, J.A.; Charusanti, P.; Polpitiya, A.D.; Adkins, J.N.; Schramm, G.; Purvine, S.O.; Lopez-Ferrer, D.; et al. Omic data from evolved E. coli are consistent with computed optimal growth from genome-scale models. *Mol. Syst. Biol.* **2010**, *6*, 390. [CrossRef]
65. Gudmundsson, S.; Thiele, I. Computationally efficient flux variability analysis. *BMC Bioinform.* **2010**, *11*, 489. [CrossRef] [PubMed]
66. Ebrahim, A.; Lerman, J.A.; Palsson, B.O.; Hyduke, D.R. COBRApy: Constraints-based reconstruction and analysis for python. *BMC Syst. Biol.* **2013**, *7*, 74. [CrossRef]
67. Warburg, O. Über den Stoffwechsel der Carcinomzelle. *Naturwissenschaften* **1924**, *12*, 1131–1137. [CrossRef]
68. Brown, R.E.; Short, S.P.; Williams, C.S. Colorectal Cancer and Metabolism. *Curr. Color. Cancer Rep.* **2018**, *14*, 226–241. [CrossRef]
69. Li, T.; Le, A. Glutamine Metabolism in Cancer. In *The Heterogeneity of Cancer Metabolism*; Le, A., Ed.; Advances in Experimental Medicine and Biology; Springer International Publishing: Berlin/Heidelberg, Germany, 2018; pp. 13–32. [CrossRef]
70. Wu, M.; Neilson, A.; Swift, A.L.; Moran, R.; Tamagnine, J.; Parslow, D.; Armistead, S.; Lemire, K.; Orrell, J.; Teich, J.; et al. Multiparameter metabolic analysis reveals a close link between attenuated mitochondrial bioenergetic function and enhanced glycolysis dependency in human tumor cells. *Am. J. Physiol. Cell Physiol.* **2007**, *292*, C125–C136. [CrossRef] [PubMed]
71. Uhlen, M.; Zhang, C.; Lee, S.; Sjöstedt, E.; Fagerberg, L.; Bidkhori, G.; Benfeitas, R.; Arif, M.; Liu, Z.; Edfors, F.; et al. A pathology atlas of the human cancer transcriptome. *Science* **2017**, *357*, 6352. [CrossRef] [PubMed]
72. Balcells, C.; Foguet, C.; Tarragó-Celada, J.; de Atauri, P.; Marin, S.; Cascante, M. Tracing metabolic fluxes using mass spectrometry: Stable isotope-resolved metabolomics in health and disease. *TrAC Trends Anal. Chem.* **2019**, *120*, 115371. [CrossRef]
73. Yao, C.H.; Fowle-Grider, R.; Mahieu, N.G.; Liu, G.Y.; Chen, Y.J.; Wang, R.; Singh, M.; Potter, G.S.; Gross, R.W.; Schaefer, J.; et al. Exogenous Fatty Acids Are the Preferred Source of Membrane Lipids in Proliferating Fibroblasts. *Cell Chem. Biol.* **2016**, *23*, 483–493. [CrossRef] [PubMed]
74. Yao, C.H.; Liu, G.Y.; Yang, K.; Gross, R.W.; Patti, G.J. Inaccurate quantitation of palmitate in metabolomics and isotope tracer studies due to plastics. *Metabolomics* **2016**, *12*, 143. [CrossRef]
75. Hasenour, C.M.; Rahim, M.; Young, J.D. In Vivo Estimates of Liver Metabolic Flux Assessed by 13C-Propionate and 13C-Lactate Are Impacted by Tracer Recycling and Equilibrium Assumptions. *Cell Rep.* **2020**, *32*, 107986. [CrossRef] [PubMed]
76. Williams, T.C.R.; Miguet, L.; Masakapalli, S.K.; Kruger, N.J.; Sweetlove, L.J.; Ratcliffe, R.G. Metabolic Network Fluxes in Heterotrophic Arabidopsis Cells: Stability of the Flux Distribution under Different Oxygenation Conditions. *Plant Physiol.* **2008**, *148*, 704–718. [CrossRef] [PubMed]
77. Wu, Y.; Li, L. Sample normalization methods in quantitative metabolomics. *J. Chromatogr. A* **2016**, *1430*, 80–95. [CrossRef]
78. Chan, S.; Cai, J.; Wang, L.; Simons-Senftle, M.; Maranas, C. Standardizing biomass reactions and ensuring complete mass balance in genome-scale metabolic models. *Bioinformatics* **2017**, *33*, 3603–3609. [CrossRef] [PubMed]
79. Pereira, R.; Nielsen, J.; Rochaa, I. Improving the flux distributions simulated with genome-scale metabolic models of Saccharomyces cerevisiae. *Metab. Eng. Commun.* **2016**, *3*, 153–163. [CrossRef] [PubMed]
80. Yuan, H.; Cheung, M.; Hilbers, P.; van Riel, N. Flux balance analysis of plant metabolism: The effect of biomass composition and model structure on model predictions. *Front. Plant Sci.* **2016**, *7*, 537. [CrossRef]
81. Dubuis, S.; Ortmayr, K.; Zampieri, M. A framework for large-scale metabolome drug profiling links coenzyme A metabolism to the toxicity of anti-cancer drug dichloroacetate. *Commun. Biol.* **2018**, *1*, 101. [CrossRef]
82. Ortmayr, K.; Dubuis, S.; Zampieri, M. Metabolic profiling of cancer cells reveals genome-wide crosstalk between transcriptional regulators and metabolism. *Nat. Commun.* **2019**, *10*, 1841. [CrossRef]

83. Nam, H.; Campodonico, M.; Bordbar, A.; Hyduke, D.; Kim, S.; Zielinski, D.; Palsson, B. A Systems Approach to Predict Oncometabolites via Context-Specific Genome-Scale Metabolic Networks. *PLoS Comput. Biol.* **2014**, *10*, e1003837. [CrossRef]
84. Turanli, B.; Zhang, C.; Kim, W.; Benfeitas, R.; Uhlen, M.; Arga, K.; Mardinoglu, A. Discovery of therapeutic agents for prostate cancer using genome-scale metabolic modeling and drug repositioning. *EBioMedicine* **2019**, *42*, 386–396. [CrossRef]
85. McGuirk, S.; Audet-Delage, Y.; St-Pierre, J. Metabolic Fitness and Plasticity in Cancer Progression. *Trends Cancer* **2020**, *6*, 49–61. [CrossRef] [PubMed]
86. Lee, S.; Jang, W.J.; Choi, B.; Joo, S.H.; Jeong, C.H. Comparative metabolomic analysis of HPAC cells following the acquisition of erlotinib resistance. *Oncol. Lett.* **2017**, *13*, 3437–3444. [CrossRef] [PubMed]
87. Fan, T.W.M.; El-Amouri, S.S.; Macedo, J.K.A.; Wang, Q.J.; Song, H.; Cassel, T.; Lane, A.N. Stable Isotope-Resolved Metabolomics Shows Metabolic Resistance to Anti-Cancer Selenite in 3D Spheroids versus 2D Cell Cultures. *Metabolites* **2018**, *8*, 40. [CrossRef] [PubMed]
88. Ricci, F.; Brunelli, L.; Affatato, R.; Chilà, R.; Verza, M.; Indraccolo, S.; Falcetta, F.; Fratelli, M.; Fruscio, R.; Pastorelli, R.; et al. Overcoming platinum-acquired resistance in ovarian cancer patient-derived xenografts. *Ther. Adv. Med Oncol.* **2019**, *11*, 1758835919839543. [CrossRef]
89. Rusz, M.; Rampler, E.; Keppler, B.K.; Jakupec, M.A.; Koellensperger, G. Single Spheroid Metabolomics: Optimizing Sample Preparation of Three-Dimensional Multicellular Tumor Spheroids. *Metabolites* **2019**, *9*, 304. [CrossRef]
90. Cavill, R.; Kamburov, A.; Ellis, J.K.; Athersuch, T.J.; Blagrove, M.S.C.; Herwig, R.; Ebbels, T.M.D.; Keun, H.C. Consensus-Phenotype Integration of Transcriptomic and Metabolomic Data Implies a Role for Metabolism in the Chemosensitivity of Tumour Cells. *PLoS Comput. Biol.* **2011**, *7*, e1001113. [CrossRef]
91. Jungwirth, U.; Kowol, C.R.; Keppler, B.K.; Hartinger, C.G.; Berger, W.; Heffeter, P. Anticancer Activity of Metal Complexes: Involvement of Redox Processes. *Antioxid. Redox Signal.* **2011**, *15*, 1085–1127. [CrossRef]
92. Gibson, D. The mechanism of action of platinum anticancer agents—What do we really know about it? *Dalton Trans.* **2009**, *48*, 10681–10689. [CrossRef] [PubMed]
93. Kelland, L. The resurgence of platinum-based cancer chemotherapy. *Nat. Rev. Cancer* **2007**, *7*, 573–584. [CrossRef]
94. Lizardo, M.M.; Morrow, J.J.; Miller, T.E.; Hong, E.S.; Ren, L.; Mendoza, A.; Halsey, C.H.; Scacheri, P.C.; Helman, L.J.; Khanna, C. Upregulation of Glucose-Regulated Protein 78 in Metastatic Cancer Cells Is Necessary for Lung Metastasis Progression. *Neoplasia* **2016**, *18*, 699–710. [CrossRef] [PubMed]
95. Gottesman, M.M.; Fojo, T.; Bates, S.E. Multidrug resistance in cancer: Role of ATP–dependent transporters. *Nat. Rev. Cancer* **2002**, *2*, 48–58. [CrossRef]
96. Drury, J.; Rychahou, P.G.; He, D.; Jafari, N.; Wang, C.; Lee, E.Y.; Weiss, H.L.; Evers, B.M.; Zaytseva, Y.Y. Inhibition of Fatty Acid Synthase Upregulates Expression of CD36 to Sustain Proliferation of Colorectal Cancer Cells. *Front. Oncol.* **2020**, *10*, 1185. [CrossRef] [PubMed]
97. Valli, A.; Rodriguez, M.; Moutsianas, L.; Fischer, R.; Fedele, V.; Huang, H.L.; Stiphout, R.V.; Jones, D.; Mccarthy, M.; Vinaxia, M.; et al. Hypoxia induces a lipogenic cancer cell phenotype via HIF1α-dependent and -independent pathways. *Oncotarget* **2014**, *6*, 1920–1941. [CrossRef]
98. Haug, K.; Cochrane, K.; Nainala, V.C.; Williams, M.; Chang, J.; Jayaseelan, K.V.; O'Donovan, C. MetaboLights: A resource evolving in response to the needs of its scientific community. *Nucleic Acids Res.* **2020**, *48*, D440–D444. [CrossRef] [PubMed]

Supplementary Material:

Thermodynamic genome-scale metabolic modeling of metallodrug resistance in colorectal cancer

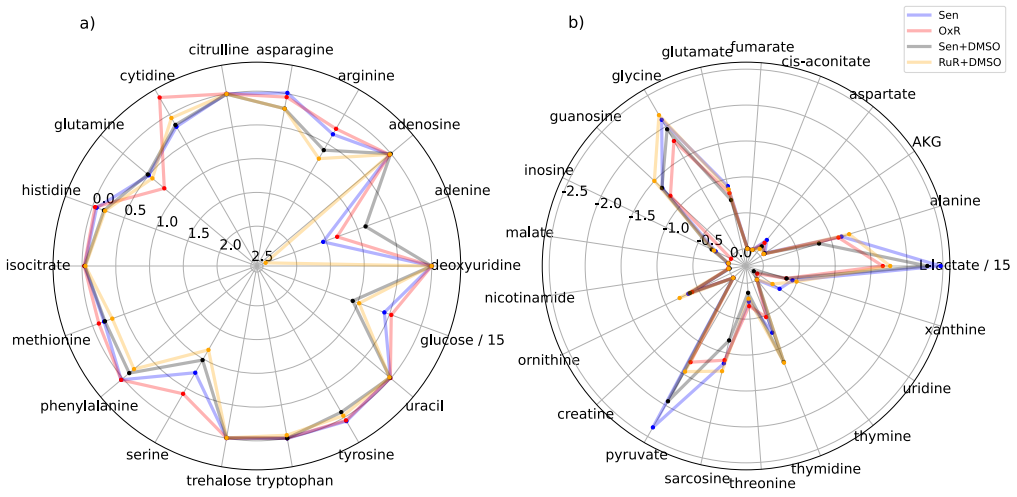

Figure S1 Experimentally determined exchanged fluxes used to constrain the HCT116 - specific genome-scale metabolic model. Metabolite concentrations in the standard and DMSO media were determined at four different time points (0, 24, 48, 72 h) and were used to calculate an uptake rate ($\mathrm{mmol\,g^{-1}\,h^{-1}}$) as outlined in the Materials and Methods. Uptake rates (a) and excretion rates (b) are shown for HCT116 cells resistant to oxaliplatin (OxR, red) or ruthenium (RuR + DMSO, orange) and their sensitive controls a standard (Sen, blue) and a 0.5% DMSO medium (Sen + DMSO, black). The exchange fluxes for lactate and glucose were scaled down by 15, as indicated by the labels, to fit into the plot.

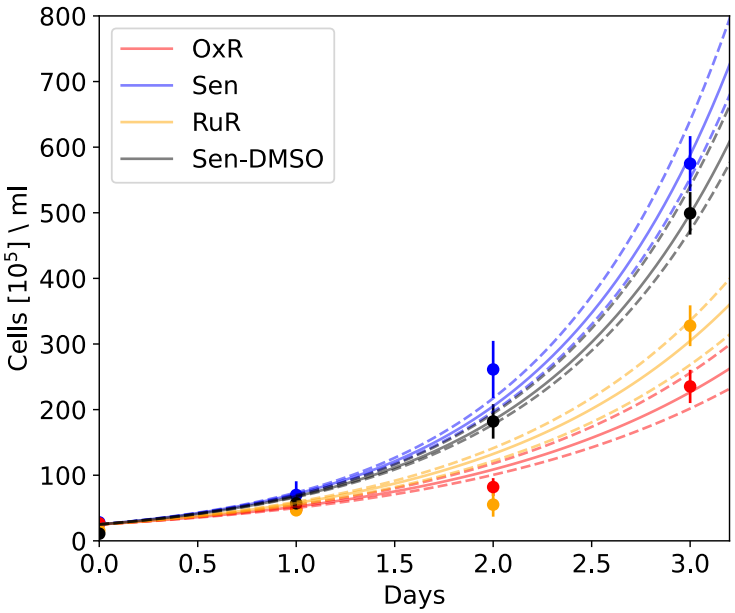

Figure S2 Observed differences in growth rate between drug treatments and their sensitive (Sen) controls. HCT116 cells resistant to oxaliplatin (OxR, red) or Bold-100/KP1339 (RuR + DMSO, orange) and their sensitive controls were inoculated in a standard (Sen, blue) and a 0.5% DMSO medium (sensitive + DMSO, black), respectively (see Materials and Methods for details). Cell density measurements were taken every 24 hours. The mean standard deviation of the three replicates measured at each time point is shown. Fitting an exponential growth curve to the mean values using the scipy package (Version 1.5.2) in Python (Version 3.7.9), the growth rate (μ) was fitted to minimize the averaged sum of squared residuals for each condition (solid line). Growth curves fitted to the upper and lower standard error (dashed lines) are also shown and were used to set upper and lower bounds in the flux analysis.

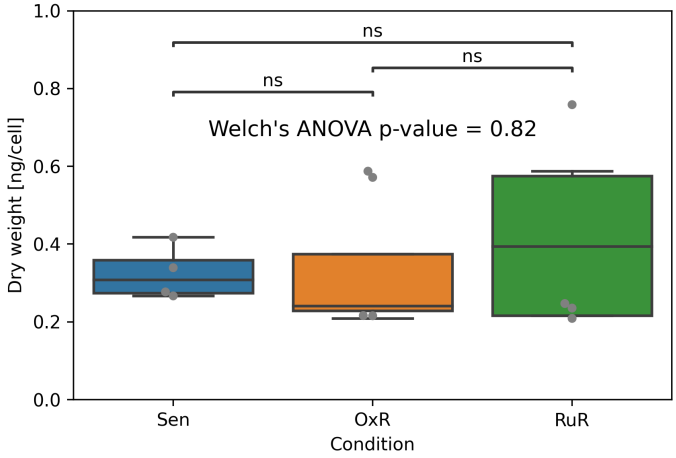

Figure S3 Cell dry weight of wild-type and resistant cells. Dry mass of HCT116 sensitive (Sen), oxaliplatin-resistant (OxR) and Bold-100/KP1339-resistant (RuR) cells were measured as outlined in the Materials and Methods. Equalities of the means was tested by Welch's analysis of variance (ANOVA). No statistically significant difference was detected.

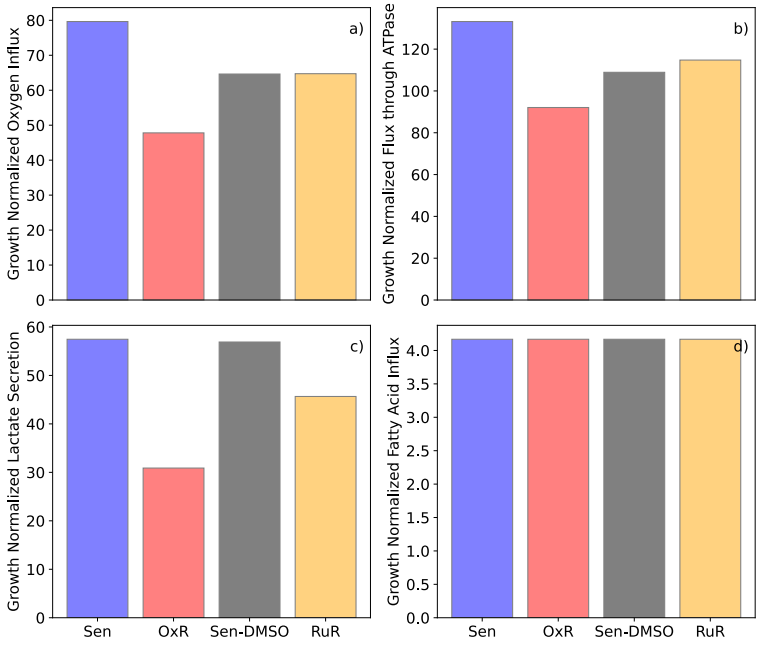

Figure S4 Comparison of fluxes through key energy metabolism reactions for ruthenium- and oxaliplatin-based resistances before growth rate normalization. Non-normalized flux values through (a) the oxygen uptake reaction - HMR_9048, (b) the ATP synthase reaction - HMR_6916, (c) the lactate secretion reaction - HMR_9135, and (d) the fatty acid influx - sum of m01362s_FAx, m02387s_FAx, m02389s_FAx, m02646s_FAx, m02674s_FAx, m02938s_FAx, across the four model instances (sensitive - Sen - blue bars; sensitive in a DMSO-based medium - Sen-DMSO - gray bars; oxaliplatin-resistant - OxR - red bards; Bold-100/KP1339 - RuR - yellow bars) are shown. Fatty acid influx is the combined influx of stearate, palmitate, oleate, linolenate, linoleate, arachidonate.

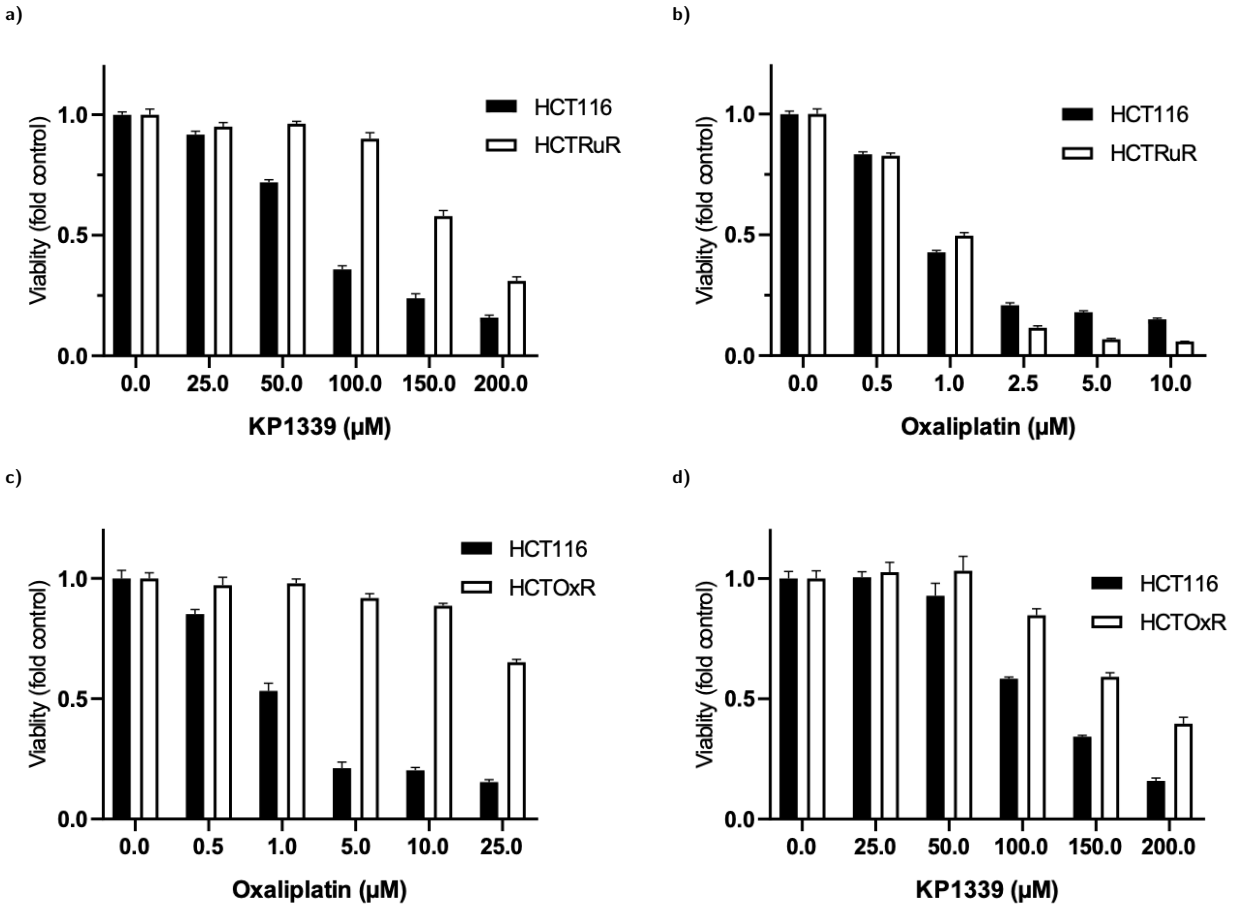

Figure S5 Investigation of cross-resistance of the resistance model HCT116 with acquired BOLD-100/KP1339-resistance (RuR) towards oxaliplatin and cross-resistance of HCT116 with acquired oxaliplatin-resistance (OxR) towards BOLD-100/KP1339. Viabilities are expressed in fold-change to untreated control in the function of the applied drug concentrations. (a) Parental sensitive HCT116 cells (HCT116) vs. RuR cells treated with the Ru-based BOLD-100/KP1339. (b) HCT116 vs. RuR cells treated with oxaliplatin. (c) HCT116 vs. OxR cells treated with oxaliplatin. (d) HCT116 vs. OxR cells treated with BOLD-100/KP1339.

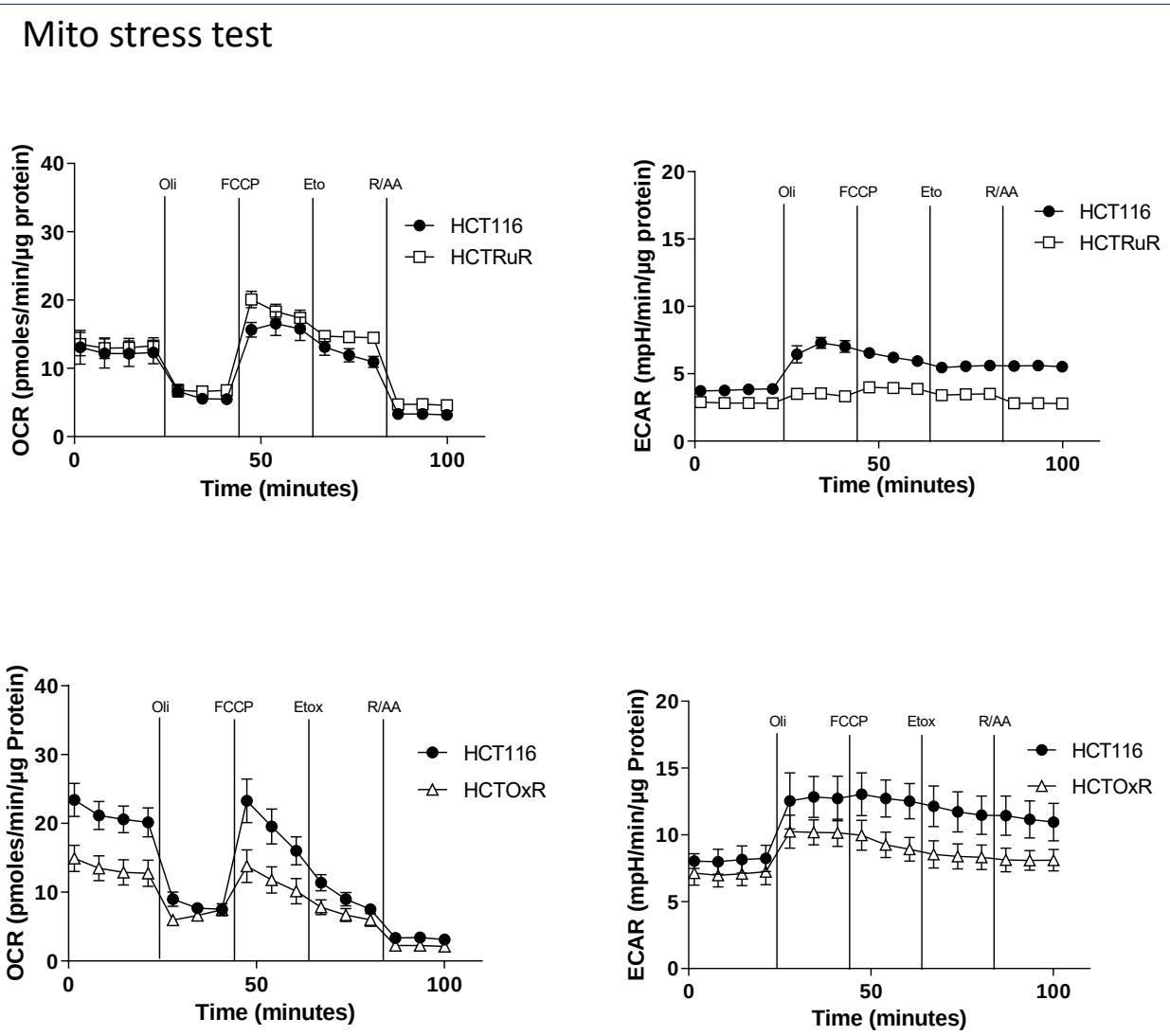

Figure S6 Mito Stress test measuring the metabolic parameters OCR and ECAR with the Seahorse FX analyzer of sensitive vs. oxaliplatin-resistant HCT116 cells (HCT116 vs. HCTOxR); and sensitive vs. BOLD-100/KP1339-resistant HCT116 cells (HCT116 vs. HCTRuR). The points and error-bars correspond to mean ± SD for each group ($n = 3$). Oxygen consumption rate (OCR) on the left and extracellular acidification rate (ECAR) on the right of the panel. All values have been normalized to total protein content in µg.

Conclusion

The three peer-reviewed original works presented in this dissertation all revolve around the development of innovative tools for preclinical studies and metallodrug research with metabolomics approaches: they explore as well as extend the frontier of novel cutting-edge methodologies. The presented works expand the toolkit of preclinical drug screening, help to dissect complex mechanisms such as oxidative stress response and decipher the metabolism behind acquiring drug resistance. Furthermore, they exemplify that precise and quantitative metabolomics data relying on a carefully chosen set of authentic standards and internal standardization has the potential to reveal consistent and fundamental metabolic effects associated with the phenotype.

Within the first publication „**Single Spheroid Metabolomics: Optimizing Sample Preparation of Three-Dimensional Multicellular Tumor Spheroids**“, we showed that even a single spheroid is sufficient to quantify a wide range of metabolites and the overall method had excellent analytical figures of merit, with metabolite concentrations in the pmol to the nmol range and low relative standard deviation even for biological replicates.

The applied ^{13}C internal standardization and protein content normalization enhanced the precision and repeatability. Moreover, the ability of profiling single spheroids is a great advantage over only being capable to measure samples containing pools of multiple spheroids, as hereby the variation in the metabolome of individual biological replicates can be characterized, enhancing the statistical power.

The observed metabolic effects revealed a marked difference between the two drugs, consistent with the different modes of action described in the literature. This publication had been the first systematic investigation of sample preparation for 3D cell cultures and it demonstrates that metabolomics experiments with single tumor spheroids could be integrated into the preclinical screening of novel compounds. Hence it is promoting and extending the utilization of an *in vitro* model with intermediate complexity, which could recapitulate more features of tumors and thus reduce the rate of failure in oncology drug discovery.

In the second publication, “**Morpho-metabotyping the oxidative stress response**” a combined, fully parallelized metabolomics and live cell imaging workflow was developed and explored regarding its potential. In particular, while imaging approaches only deliver information about a limited number of molecular features, the metabolomics methodology utilizing internal standardization and external calibration provides quantitative concentrations of over 100 compounds of the primary metabolism. N-ethylmaleimide (NEM) derivatization was carried out during the extraction of metabolites, which enabled the quantification of primary thiols, substances otherwise prone to unwanted oxidation.

Despite superb quantification, metabolomics so far is unable to capture spatial information and only obtains a bulk concentration of typically $100x10^3$ or more cells. Microscopy techniques complement this, and with the combination of fluorescent probes (also redox-sensitive and compartment-specific dyes), they enable the characterization of the cells' functional state, thereby indicating and allowing the quantification of mitochondrial redox stress. Moreover, the applied live cell imaging technique does not require fixing of the cells, but enables real-time observation of the living cells on a special cell culture plate after a washing and a brief staining period and is, therefore, less prone to artifact formation (Cole, 2014; Stephens and Allan, 2003).

Even within the short 2 h incubation with hydrogen peroxide, the metabolome was widely perturbed, as 51 metabolites significantly changed. Also, through the imaging we observed a strong increase in the mitochondrial superoxide levels. Analysis of the mitochondrial morphology revealed significant changes in multiple morphology and mitochondrial network parameters, indicating a shift towards fragmentation of the mitochondrial network.

In line with this, metabolomics showed that the cells are in an energy-depleted state, as a consequence of dysfunctional mitochondria and energy-expensive redox homeostasis. Moreover, several other hallmarks of redox stress, such as increased oxidized to reduced glutathione ratio, increased glutathione, and NADPH synthesis, were observed. Since we utilized ^{13}C labeled internal standards during the extraction, we were able to prove the absence of abiotic oxidation (tracing back to mixed ^{13}C-^{12}C oxidized glutathione formation) during the sample preparation, thus all observed oxidation is caused by hydrogen peroxide and is experimental design-related.

Finally, in the third publication "**Thermodynamic Genome-Scale Metabolic Modeling of Metallodrug Resistance in Colorectal Cancer**" we applied metabolomics, genome-scale metabolic modeling and flux-balance analysis for the investigation of two cellular models of the HCT116 cell line with acquired metallodrug resistance to oxaliplatin and BOLD-100/KP1339.

Although the absolute metabolite concentrations exhibit profound differences between resistance models and their respective parental sensitive control cell line (with some being shared differences, while others seem to be drug-specific), we found that these differences of metabolite levels do not necessarily translate into differences in the fluxes of the corresponding reactions.

Another interesting finding was that normalization to the growth rate of the particular model is crucial and impacts the results to a high degree, with some pathways becoming more prominent, while others lost a large fraction of significant reaction fluxes after this correction. It is important to note that normalization to growth rate is only possible in the dynamic context of fluxes, but not with static

metabolite concentrations, and growth rate normalization was critical, although the input data for the flux distribution were metabolite concentrations already normalized to total protein content (a good proxy of cell numbers and total biomaterial). Most of the changes in metabolism that accompany acquired resistance are found in energy metabolism and related pathways: oxidative phosphorylation, fatty acid metabolism, pentose phosphate pathway (PPP), glycolysis/gluconeogenesis, TCA cycle, and ROS detoxification.

We also simulated and compared fluxes through key energy metabolism reactions, which are usually measured via mitochondrial stress test with Seahorse XF analyzers by evaluating the oxygen consumption rate and extracellular acidification rate in a time-course experiment (upon addition of enzymatic inhibitors and electron transport chain uncouplers). The comparison with the experimental results revealed good agreement, especially with data not normalized to the growth rate. Furthermore, simulation of fatty acid influx and oxygen requirement for cellular growth implied that the BOLD-100/KP1339-resistant model has a higher fatty acid and oxygen intake requirement for a comparable growth rate, prompting us to hypothesize a possible metabolic vulnerability.

Although these three publications present specific cases to illustrate the applicability of the developed methods, they can be used in a broader context. Regarding the biomaterial, we hold that the workflows are not limited to the cell line of our choice (as in all cases the human colon cancer cell line HCT116 and its variants with in-house generated acquired resistance were used), but can be extended to any established cell line. In terms of metabolic modeling, a cell line-specific model was available, but on a minimum basis, a model organism with an available genome-scale metabolic model is required and should be sufficient. Although we showcase the differences between acquired oxaliplatin and BOLD-100/KP1339-based resistances, the approach certainly works for any phenomenon which has a profound metabolic basis to study, such as intrinsic drug resistance.

The presented workflows are published in peer-reviewed open access journals and great care was taken to describe in detail the specific steps in order to make the methods reproducible and reusable for the scientific community. Although much effort was made to exhaustively analyze the datasets in a targeted manner from a biochemical and metabolism perspective, most of the raw data was acquired with high-resolution Orbitrap HF mass spectrometer, thus leaving room for further extensive nontargeted evaluation. In order to exercise good scientific conduct and make a step towards more reproducible omics-type experiments, we made the data available on a public repository. This also enables researchers to carry out further data mining in the future, as well as reprocess the raw data and include it in meta-analysis.

List of all peer-reviewed publications

1. Arakawa A, Jakubowski N, Flemig S, Koellensperger G, Rusz M, Iwahata D, et al.
High- resolution laser ablation inductively coupled plasma mass spectrometry used to study transport of metallic nanoparticles through collagen-rich microstructures in fibroblast multicellular spheroids.
Anal Bioanal Chem. 2019 Jun 1;411(16):3497–506.
https://doi.org/10.1007/s00216-019-01827-w

2. Galvez L, Rusz M, Jakupec MA, Koellensperger G.
Heart-cut 2DSEC-RP-LC-ICP-MS as a screening tool in metal-based anticancer research.
J Anal At Spectrom. 2019 Mar 26;
https://pubs.rsc.org/en/content/articlelanding/2019/ja/c9ja00045c

3. Galvez L, Rusz M, Schwaiger-Haber M, Abiead YE, Hermann G, Jungwirth U, et al.
Preclinical studies on metal based anticancer drugs as enabled by integrated metallomics and metabolomics.
Metallomics . 2019 Oct 16; 11(10):1716–28.
https://pubs.rsc.org/en/content/articlelanding/2019/mt/c9mt00141g

4. Rampler E, Egger D, Schoeny H, Rusz M, Pacheco MP, Marino G, et al.
The Power of LC-MS Based Multiomics: Exploring Adipogenic Differentiation of Human Mesenchymal Stem/Stromal Cells.
Molecules . 2019 Jan; 24(19):3615.
https://www.mdpi.com/1420-3049/24/19/3615

5. Rusz M, Rampler E, Keppler BK, Jakupec MA, Koellensperger G.
Single Spheroid Metabolomics: Optimizing Sample Preparation of Three-Dimensional Multicellular Tumor Spheroids.
Metabolites . 2019 Dec; 9(12):304.
https://www.mdpi.com/2218-1989/9/12/304

6. Oberhuber M, Pecoraro M, Rusz M, Oberhuber G, Wieselberg M, Haslinger P, et al.
STAT3-dependent analysis reveals PDK4 as independent predictor of recurrence in prostate cancer.
Molecular Systems Biology . 2020 Apr 1; 16(4):e9247.
https://www.embopress.org/doi/full/10.15252/msb.20199247

7. Rampler E, Abiead YE, Schoeny H, Rusz M, Hildebrand F, Fitz V, et al.
Recurrent Topics in Mass Spectrometry-Based Metabolomics and Lipidomics—Standardization, Coverage, and Throughput.
Anal Chem . 2021 Jan 12; 93(1):519–45.
https://doi.org/10.1021/acs.analchem.0c04698

8. Rusz M, Del Favero G, El Abiead Y, Gerner C, Keppler BK, Jakupec MA, et al.
Morpho-metabotyping the oxidative stress response.
Sci Rep . 2021 Jul 29; 11(1):15471.
http://www.nature.com/articles/s41598-021-94585-8

9. Herrmann HA, Rusz M, Baier D, Jakupec MA, Keppler BK, Berger W, et al.
Thermodynamic Genome-Scale Metabolic Modeling of Metallodrug Resistance in Colorectal Cancer.
Cancers . 2021 Jan; 13(16):4130.
https://www.mdpi.com/2072-6694/13/16/4130

10. Abiead YE, Milford M, Schoeny H, Rusz M, Salek RM, Koellensperger G.
Benchmarking feature quality assurance strategies for non-targeted metabolomics.
bioRxiv; 2021. p. 2021.09.09.459600.
https://www.biorxiv.org/content/10.1101/2021.09.09.459600v1

11. Baier D, Schoenhacker-Alte B, Rusz M, Pirker C, Mohr T, Mendrina T, et al.
The Anticancer Ruthenium Compound BOLD-100 Targets Glycolysis and Generates a Metabolic Vulnerability towards Glucose Deprivation.
Pharmaceutics . 2022 Feb; 14(2):238.
https://www.mdpi.com/1999-4923/14/2/238

Ich habe mich bemüht, sämtliche Inhaber der Bildrechte ausfindig zu machen und ihre Zustimmung zur Verwendung der Bilder in dieser Arbeit eingeholt. Sollte dennoch eine Urheberrechtsverletzung bekannt werden, ersuche ich um Meldung bei mir.

Mate Rusz

Juni, 2022